UCLouvain

epl

École polytechnique de Louvain

Luminescent properties of narrow emission red phosphor

an *ab initio* study

Author: **Julien Bouquiaux**
Supervisors: **Xavier Gonze, Yongchao Jia**
Readers: **Clément Lauzin, Gian-Marco Rignanese**
Academic year 2019–2020
Master [120] in Physical Engineering

Abstract

Recent experimental discovery of narrow emission red phosphor $Sr[Li_2Al_2O_2N_2]:Eu^{2+}$ enables a potential noticeable leap in the luminous efficacy of phosphor based white LEDs because of its advantageous luminescent properties. Understanding those properties and their temperature dependence from a theoretical perspective is however something that has not been done yet. This master thesis aims at providing such characterization of the temperature dependence of the luminescent properties of $SALON:Eu^{2+}$.
For this purpose, a combination of density functional theory (DFT) calculations and configuration coordinate models (CCM) based on the Franck-Condon overlaps were used. Thermal expansion coefficient was computed within the quasi-harmonic approximation and its effect on the luminescence spectrum was calculated. A complete phonon decomposition of the luminescent spectrum is also obtained with a generating function approach. A new method based on molecular dynamic is finally explored for the theoretical study of luminescence spectrum.
The results of this work showed that the use of the 1D-CCM is sufficient to fairly reproduce experimental luminescence spectrum as well as the temperature dependence of the FWHM. The generating function approach allowed us to identify an important phonon mode at 33.7 meV that strongly couples with the optical 4f-5d transition. Results also revealed that the 1D-CCM, greatly used in the field to explain luminescent properties, is not suitable to correctly reproduce the temperature dependence of the emission maximum. It is only by considering all the vibrations modes by means of molecular dynamic simulation that the experimental blue shift was observed. We found also that accounting for the prefactor ω^3 in the computation of the luminescence intensity is crucial to explain the shift (with ω the light frequency).

Acknowledgements

First, I would like to thank my supervisor, Professor Xavier Gonze, that brought me in this truly fascinating research field at the frontier of fundamental physics and applied science. I am very grateful to him for the numerous remarks, advice and explanations he gave me during our nearly weekly meetings. His availability, his deep knowledge in the field and the interest he put in my work were really motivating. This master thesis would not have been possible without him.

I also want to warmly thank Yongchao Jia for the time he spent considering my work throughout this year. His experience in the field and his always relevant remarks were really helpful.

I want to thank Masayochi Mikami, Anna Miglio and Samuel Ponce for the attention they put in my researches. Each month, with Xavier Gonze and Yongchao Jia, we took some time to discuss the progress of my work. These fruitful discussions allowed me to critically assess the results obtained during this master thesis and to explore new ideas. This is why, although all the results come from my simulations, I will prefer the pronoun "we" to the pronoun "I" in this manuscript. Participating to such international collaboration gave me a taste of how scientific collaboration works, it was very instructive and motivating!

Of course, I want to thank Louise for her support and her (maybe slightly fake) attentive ear on my endless explanations on how crazy light-matter interaction was.

Last but not least, I want to thank my parents for their support during these five years of study and for their precious remarks in the last rush of the writing process.

Computational resources have been provided by the supercomputing facilities of the Université catholique de Louvain (CISM/UCL) and the Consortium des Équipements de Calcul Intensif en Fédération Wallonie Bruxelles (CÉCI) funded by the Fond de la Recherche Scientifique de Belgique (F.R.S.-FNRS) under convention 2.5020.11 and by the Walloon Region.

Contents

Introduction

Improving energy efficiency of our daily-life technologies is one of the answer to the urgent need of energy saving for CO_2 emission reduction. The lightning sector is one of those sectors where there is still some gains to make by replacing old incandescent lamps by more efficient light sources such as white LEDs. One way to manufacture those white LEDs is to coat a blue-LED with a material called "phosphor" that is able to down-convert a fraction of the blue light to lower frequency light (red for instance). The resulting light (mix of the blue light not down-converted and the fraction of blue light down-converted) will appear white.

While efficient green and yellow phosphors are well-known today, an efficient commercial red phosphor is still lacking because of the strict requirements that a red phosphor should fulfil : a precise location of the emission peak, a small full width a half maximum and luminescent properties that remain weakly affected by temperature. In 2019, Hoerder et al. [1] reported the experimental discovery of a new red-emission phosphor ($Sr[Li_2Al_2O_2N_2]:Eu^{2+}$ abbreviated SALON) that fulfils all these requirements, enabling an eventual noticeable leap in energy efficiency of white LED based on red phosphor. In addition to their experimental characterization of the luminescent properties of SALON, they also provided a succinct *ab initio* study (basically the atomic positions and the electronic density of states). A full theoretical study of this promising material is thus still lacking, little is known for the moment on SALON.

The aim of this master thesis is precisely to provide such global characterization of SALON from a theoretical perspective. This is achieved with first-principles calculations in density functional theory (DFT) and with the help of theoretical models that allow one to describe luminescent properties of solids. On one hand, our goal is to check the predictive power of the methodology used as well as explaining from a theoretical perspective what is observed experimentally. On the other hand, we provide predictions that could be compared with future experimental results.

The first chapter of this manuscript is dedicated to the description of the working principle of phosphor based white LEDs and explains why red phosphors are challenging to produce. The key experimental results of the new SALON red phosphor are also presented in this chapter.

In the second chapter, the theoretical framework of the *ab initio* calculations performed for this work is presented. Density functional theory and its implementation on ABINIT (the software used) are detailed.

In chapter 3, the physical mechanisms of photoluminescence are detailed. An "atomic" point of view is first presented to get familiarised with emission of light and the importance

of the matrix dipole elements. Those notions are then extended to solids : first in an static lattice and then in a real vibrating lattice. Finally, one-dimensional and multi-dimensional models that enable to predict the shape of the emission spectrum are extensively presented.
Chapter 4 aims to present the *ab initio* ground state results obtained with ABINIT. This chapter begins with a first-principle characterization of bulk SALON (without europium) : crystal structure, electronic structure, phonon modes and thermal expansion coefficient. Then some preliminary results on Europium doped SALON that will be useful for the next chapter are presented.
In the two last chapters, the *ab initio* results of chapter 4 are combined with the theoretical formalism of chapter 3. More precisely, in chapter 5, we focus first on the 4f-5d electronic transition that is responsible for radiative processes in rare-earth ions (band structures in excited and ground state as well as the structural relaxation accompanying this transition). Relevant parameters of the one-dimensional configuration coordinate model are calculated and used to compute the photoluminescent (PL) spectrum. This PL spectrum is then compared to what is obtained with a multi-dimensional model based on a generating function approach.
In chapter 6, the dependence in temperature of the PL spectrum is theoretically studied. We first use the one dimensional model with a computation of the Franck-Condon overlaps to predict it. Then the effect of thermal expansion is explicitly added. Finally, a novel approach based on molecular dynamic simulation is exploited to determine the temperature dependence of PL spectrum.
To obtain the results of chapter 4, 5 and 6, I have used well established methods (DFT, DFPT, quasi-harmonic approximation, ΔSCF). Moreover, I have implemented some codes that allow us to predict PL spectrum to any temperature based on a quantum formulation of the 1D-CCM with the explicit computation of the Franck-Condon factors. In combination with DFT calculations, this method proved its predictive power by agreeing well with experimental PL spectrum. Following the work of Alkauskas et al. in [2], I have also implemented a multi-dimensional model based on the generating function approach that allows one to completely decompose the PL spectra in all the phonon modes at 0K. This analysis led to the identification of an important mode at 33.7 meV that strongly couples with optical 4f-5d transition. Finally, the innovative method based on molecular dynamic has been shown effective to correctly predict the experimental shift of the emission peak with temperature (quantity that the 1D model was not able to predict). To our knowledge, this is the first time that such analysis is performed on the study of PL spectrum of phosphor.

Chapter 1

Phosphor based white LEDs

Contents

1.1 Overwiew

Nowadays, light emitting diodes (LEDs) is a mature technology that compete with incandescent and fluorescent lamps. They have numerous advantages over the latter : small size, higher lifetime, robustness, fast switching and a higher efficiency [3]. It is commonly admitted that the replacement of incandescent lamps by alternative light sources such as LEDs could lead to a huge reduction of electricity consumption worldwide (assuming no considerable "rebound" effect [4]). This is of course in line with the urgent need of energy saving for CO_2 emission reduction. To fix the ideas, in their SSL (Solid State Lighting) plan that relies heavily on LEDs technology, the US department of energy estimated in 2019 that the energy savings could account to about a 5% reduction in the total primary energy budget of the United States [5]. One of the main drawback of LED technology is the lack of high color quality for white LEDs. There are typically two ways of producing white LEDs (see figure 1.1) :

- Use individual LEDs that emit primary colors (red, green and blue) and then mix all the colors to form a spectral distribution that appears white light to human eye. This approach is typically used for display technologies because of the flexibility of mixing different colors. One of the main drawback of this technology is that the three narrow-band LEDs do not exhibit the same behaviour under temperature increase or ageing, leading to an undesirable shift of performances (feedback electronics with colour sensors is typically used to handle this problem, making the overall system quite complex).

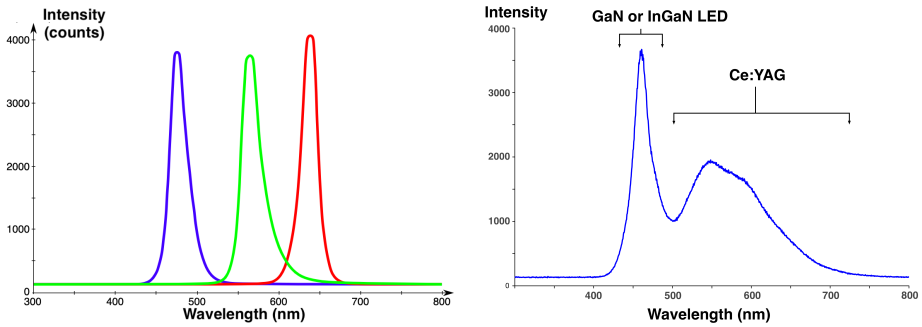

Figure 1.1: Left : Combined spectral curves resulting of the mixing of red-green-blue LEDs light sources to produce white color. Right : Spectrum of a phosphor-based white LED showing blue light directly emitted by the GaN-based LED and the more broadband Stokes-shifted light emitted by the Ce^{3+}:YAG phosphor. Images adapted from [6].

- Use a phosphor material to convert monochromatic light from a blue or UV LED (for instance blue GaN-based LED) to broad-spectrum white light. This approach is more popular due to its simpler and cheaper manufacturing process. The majority of high-intensity white LEDs on the market are manufactured using phosphor light conversion.

Phosphors consist of a crystalline host material doped with a relatively small amount of rare earth or ions such as Eu^{2+} that convert light from shorter wavelength to longer wavelength (process called Stokes shift) via electronic transitions. Within this second approach based on phosphors, two main families of LEDs are available depending on the origin of the short wavelength excitation :

Multi-phosphor approach The first family uses a near UV LED chip that is coated by a mixture of RGB phosphors (figure 1.2 left). The idea is to fully down-convert the near UV light to specific colours by using different phosphors.

Single-phosphor approach In this approach, the excitation light comes from a visible blue LED. The combination of the light generated by the phosphor layer (typically a yellow phosphor based on YAG:Ce^{3+}) and the blue light leaking through creates white light (figure 1.2 right.)
Two parameters are usually used to define the performances of any light source : the luminous efficacy (LE) and the color rendering index (CRI). The luminous efficacy of radiation is defined as the ratio of the total luminous flux (measure of the perceived power of light by human eye, in lumens) to the total spectral power (watts). Roughly speaking, it tells how well a light source produces visible light that is effectively perceived by human eye. The CRI describes the ability of a light source to reproduce the colors of objects faithfully in comparison with an ideal or natural light source. Incandescent lamps are often chosen as reference source based on black-body radiation, they have a CRI of 100. A high value of CRI is important for high quality and comfortable lighting. Another important quantity is the correlated color temperature (CCT) which is the temperature of an ideal black-body

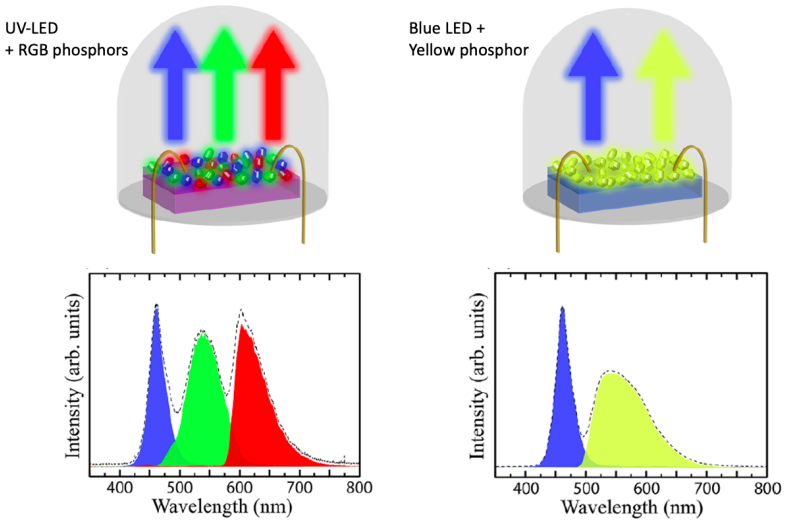

Figure 1.2: Schematic representation of phosphor-based white LEDs based on a near UV-LED and a mixture of RGB phosphors (left), and a blue LED combined with a yellow phosphor (right), and their corresponding emission spectra. Image adapted from [7]

radiator that radiates light of a color comparable to that of the light source. The higher the CCT is, the colder human eye perceives the light. Generally speaking, the light emitted from UV-based phosphor white LEDs is perceived as warmer light than the one from blue-based phosphor white LEDs [7]. Moreover, the UV-based LEDs shows higher efficiency for warmer white light emissions. On the other hand, they are more difficult to fabricate and thus of higher cost. Finally, we notice also that warm phosphor-based white LED can be obtained by exciting green and red phosphors by blue LEDs. This method shows high efficiency due to the small difference between excitation and emission wavelengths. For this reason, it is nowadays an important focus for the field to improve the technology based on blue-LEDs with a great effort to lower the CCT as well as increase the CRI. As we will see, one current active challenge is to find highly efficient red phosphors.

1.2 The challenge with red phosphors

While efficient blue, yellow and green phosphors are well established today, finding highly efficient red phosphors has been a limiting factor to a further increase in the overall luminous efficacy and is currently a big challenge for researchers. The main reason for this is the following : The spectral human eye response function (as depicted in grey in figure 1.3) shows a peak at 557 nm in the green and decay progressively in the red region. Our eyes are less sensitive to red colours. As a result, the part of the emission spectra of a light source that extend in the deep-red and near infra-red region is a waste of spectral power since this spectral region does not overlap with spectral human eye response, leading to an important decrease in the luminous efficacy. In order to sufficiently cover the red spectral region while minimizing the efficacy loss caused by low eye sensitivity at long wavelengths, red phosphors with very narrow emission bandwidth (shown in red on 1.3 as

opposed to large emission bandwidth in blue that causes a considerable decrease in luminous efficacy) showing a peak in the optimal red wavelength (610-620 nm) are required [1]. On the top of that, the performances of the phosphor should remain practically unchanged at LED working temperature. This means first that the total amount of emitted intensity should remain approximately constant upon increasing temperature, this is often measured trough the integrated photoluminescence intensity that should not decrease too much. This is known as the *thermal quenching* behaviour of the phosphor. Moreover, as a narrow band is required, the bandwidth of the emission spectrum should not increase dramatically with temperature. Also, the emission peak should not shift too much with temperature increase.

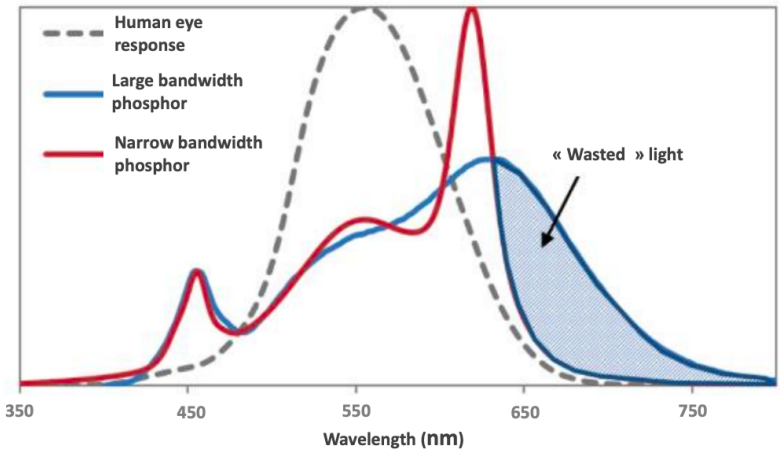

Figure 1.3: Spectral comparison of a narrow bandwidth phosphor and a large bandwidth phosphors with human eye response. Good red phosphor requires a narrow bandwidth to avoid a decrease in the luminous efficacy represented by blue area (the ≪wasted≫ light). Image adapted from [8]

1.3 SALON red phosphor

Until recently, only a few red phosphors were able to fulfil the requirements mentioned above. We can mention three red phosphors that are commercially available : $(Ba,Sr)_2Si_5N_8:Eu^{2+}$ (maximum peak at 590 nm to 625 nm, full width at half maximum (FWHM) of 71 to 101 nm), $(Ca,Sr)SiAlN_3:Eu^{2+}$ (maximum peak at 610 nm to 660 nm, FWHM of 78 to 108 nm) and the promising $Sr[LiAl_3N_4]:Eu^{2+}$ discovered recently in 2014 [9] (maximum peak at 654 nm and FWHM of 50 nm). The first two have very large FWHM and thus a low luminous efficacy, which is not suitable for high performance applications. On the other hand, SLA demonstrated a luminous efficacy gain of 14% compared to similar commercial red phoshors with high CRI. However, because of its emission peak located at longer wavelength, its drawback is that a considerable amount of radiation is located in a spectral region with low human eye sensitivity. It exists a red phosphor $SrMg_3SiN_4:Eu^{2+}$ combining narrow FWHM (43 nm) with a suitable emission peak location (615 nm). The problem is

that the latter suffers from high thermal quenching, making it not usable for LED application.

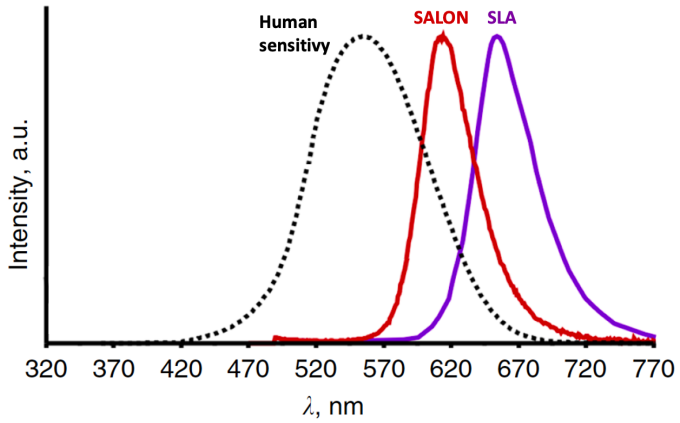

Figure 1.4: Emission spectrum (red, excited with λ_{exc} equals 460 nm) of SALON in comparison to $Sr[LiAl_3N_4]:Eu^{2+}$ (purple) and the human-eye sensitivity curve (black dotted). Figure adapted from [1].

In 2019, Hoerder et al. reported the experimental discovery of a new narrow-band red emission phosphor $Sr[Li_2Al_2O_2N_2]:Eu^{2+}$ abbreviated SALON that presents an emission peak located at 614 nm and a FWHM of 48 nm at room temperature [1]. The fact that the emission peak is located at shorter wavelength than its cousin SLA enables a gain of 16% in luminous efficacy, while keeping an excellent color rendering. This gain can be clearly seen by comparing the two spectra on figure 1.4. As this work focuses on the study of this material, let us detail a bit more the important experimental results. Hoerder et al. found that SALON crystal structure (shown on figure 1.5) is an ordered variant of the UCr_4C_4 structure type with strontium on the corresponding uranium site, aluminium and lithium on the corresponding chromium site and nitrogen and oxygen on the corresponding carbide site (more informations on this structure on the related results section). This kind of structure is well known in the research field of phosphor to provide a highly condensed and rigid framework structure [10]. It shows also a highly symmetrical coordination environment around the strontium sites (partially replaced by europium doping agent that is responsible for the luminescent properties, the experimental doping rate is 0.7%).

The authors make the link between this highly symmetrical coordination environment and the narrow emission band of SALON, they explained [1] : « The most probable reason for the narrow emission band of SALON is the high local symmetry around the Eu^{2+} activator position in the crystal structure as the ordered arrangement of four oxygen and four nitrogen atoms is forming a cube-like coordination polyhedron. This highly symmetrical coordination is expected to be the reason for the narrow emission as a result of a more isotropic structural relaxation of the Eu^{2+} in its excited state, which reduces the number of energetically different states involved in the emission process. »
The authors showed that SALON properties are relevant for application : a quantum effi-

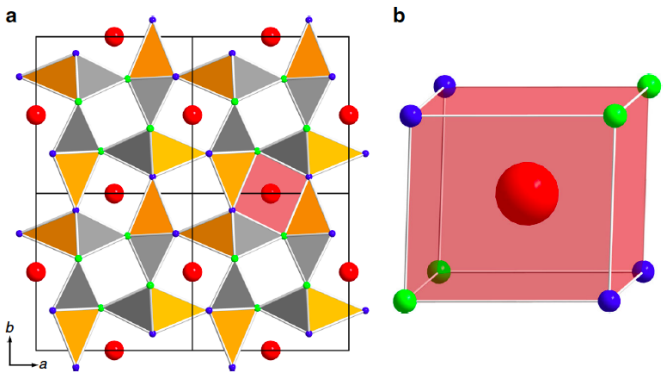

Figure 1.5: Structural overview of SALON. Red spheres represent strontium, blue spheres oxygen, and green spheres nitrogen atoms. The $[LiO_3N]^{8-}$ tetrahedra are shown in orange, the $[AlON_3]^{8-}$ tetrahedra in grey, and the red polyhedron represents the cube-like coordination of Sr^{2+}. (a) Viewing of a 2x2x2 supercell of $Sr[Li_2Al_2O_2N_2]:Eu^{2+}$ along c axis. (b) Perspective viewing of the eight-fold coordination of Sr^{2+} by O and N. Image and caption from [1]

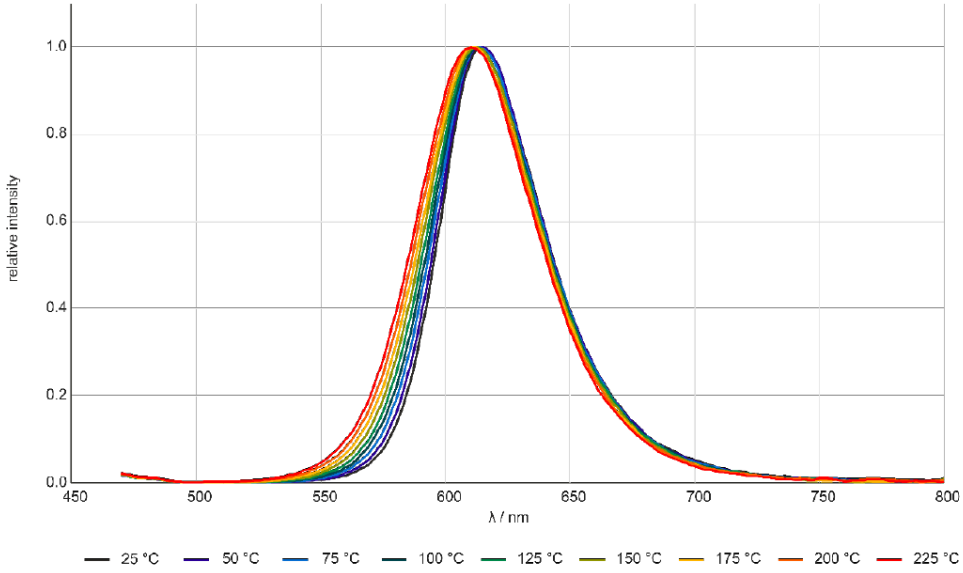

Figure 1.6: Emission spectra of SALON between 25°C to 225 °C in normalized intensities. Image from supplementary informations of [1].

ciency of greater than 80%, a low thermal quenching of only 4% at operating temperatures, reasonable thermal and chemical stability. They also provide useful informations on the temperature dependence of the emission spectrum. Namely, a low-temperature (15K) full width at half maximum measured at 41 nm (48 nm at room temperature). They also measured emission spectra for 9 temperatures (from 25°C to 225 °C), this is shown on figure 1.6. From these measurements, they observed that the peak of the emission peak is

blue-shifted (it goes toward shorter wave-length) from 614 nm at 25°C to 610 nm at 225 °C.

In this work, we will try to answer the following question : Is it possible to reproduce such results based on *ab initio* calculations? The idea is simple but quite profound: given the the crystal structure of the material and no other experimental input parameter, are we able to predict the luminescent properties just based on our physical comprehension of luminescent mechanisms (and the help of a computer, of course)? In addition to this "prediction" aspect, the comparison between experiment and *ab initio* calculations is very useful to make sure that the physical interpretation of the experimental results are correct (it would be in general the case if experimental and *ab initio* calculations are matching). Discrepancies between experiment and calculations are also useful : it generally means that something is missing in the physical understanding of a phenomenon. What is missing? What effect have we neglected in the calculation? Of course, such discrepancy can also comes from an intrinsic limitation of the calculation (for instance the classical band gap problem in DFT).

More precisely, we will focus in this work on the understanding of the properties of the emission spectrum of SALON as depicted in figure 1.6 : the location of the peak, the FWHM, the temperature dependence,... To sum-up in one question : **What physical mechanisms are hidden behind those apparently innocent slightly asymmetrical gaussian curves?**

Chapter 2

Numerical simulation method

Contents

2.1 Foreword on quantum mechanics

All the matter surrounding us is made of positively charge nuclei and their respective electrons. To understand some of its properties that could not be explained by classical physics (such as the black-body radiation, the photo-electric effect or the spectral lines), physicists of the early twenties came up with a new theory : quantum mechanics. In the case of a non-relativistic problem, this theory states that the dynamical evolution of a system (described by its wavefunction $\Psi(t)$) is governed by the time-dependent Schrödinger equation

$$i\hbar\frac{\partial\Psi}{\partial t} = H\Psi \tag{2.1}$$

where $\hbar$ is the reduced Planck constant and H is the Hamiltonian operator that represents the total energy of the system. This physical theory has been successfully confirmed experimentally many times and is at the heart of the understanding of many daily-life technologies (semi-conductors, lasers,...). It is worthy to note that while the mathematical formalism is well known for almost one century and described in many excellent textbooks (for instance the Cohen Tanoudji book series [11]), there is however still a animated debate on how we should interpret quantum mechanics (see for instance F. Laloé's book [12] that tries to clarify remaining conceptual problems and their different interpretations). What does the wavefunction represent exactly? Is is something "real", or just a mathematical tool that allows to calculate probabilities? Why and how does the wavefunction "collapse" under measurement? Plenty of conceptual questions are still open. But since it "works" and give

the correct predictions, does it matter at the end? One should simply say that quantum theory needs no interpretation after all [13] : Mermin in [14] ironically summarized this attitude in the famous quote “shut up and calculate”.

2.2 An interacting many-body problem

The structure of the two next sections are inspired by [15] and [16]. If the problem to solve is time-independent and after having decoupled nuclei dynamics from electron dynamics (Born Oppenheimer approximation described in section 3.2.1), the behaviour of N interacting electrons is governed by time-independent Schrödinger equation that stipulates that the Hamiltonian operator acting on the electronic wavefunction ψ gives this same wavefunction multiplied by the total energy of the system :

$$H\psi = E\psi \tag{2.2}$$

$$H = \sum_n \left(\frac{-\nabla_n^2}{2} + \sum_I \frac{Z_I}{|\boldsymbol{r}_n - \boldsymbol{R}_I|} + \sum_{m>n} \frac{1}{|\boldsymbol{r}_n - \boldsymbol{r}_m|} \right) \tag{2.3}$$

Here we have used atomic units ($\hbar = m_e = 4\pi\epsilon_0 = 1$). The first term of the Hamiltonian stands for the kinetic energy of the electrons. The second is a constant potential that originates from the Coulomb interaction between electrons and the fixed nuclei that is often referred as an external potential V_{ext}, even if V_{ext} is in principle not restricted to the electron-ion interaction and can take into account arbitrary external applied potential. Actually, if only those two first terms are used and the third is ignored, the problem becomes way easier since electrons are independent of each other : the wavefunction of the system that depends on the configuration of N electrons position $\psi = \psi(\boldsymbol{r}_1, ..., \boldsymbol{r}_N)$ can thus be expressed simply as a product of N one-electron wavefunctions that are solutions of one-electron Schrödinger equation : $\psi = \phi(\boldsymbol{r}_1)...\phi(\boldsymbol{r}_N)$. This is known as the independent-electron approximation.
The real difficulties are occurring when considering the last term of equation 2.3 because the motion of one electron is now correlated to the motion of all the other electrons, making the electronic problem hard to solve for large number of particles. Many approaches exist to handle the problem. For instance the Hartree-Fock approximation where the electronic repulsion is averaged trough an integration on the electronic density (known as the Hartree potential) and the electronic wavefunction is replaced by Slater determinant to respect Pauli exclusion principle. In the next section, we will describe in more details another approach implemented in the software ABINIT that was used during this master thesis : the density functional theory.

2.3 Density functional theory

Density Functional Theory (DFT) is a powerful method that, as its name suggests, uses the electron density $n(\boldsymbol{r})$ as the central quantity to compute the total energy of a system, in principle in an exact way. Let us show the main features of DFT by starting with two theorems that are the building blocks of DFT.

Hohenberg-Kohn theorems

Hohenberg and Kohn, in 1964, introduced two theorems that are at the basis of DFT [17]. The first theorem stipulates that the external potential $V_{ext}(\boldsymbol{r})$ is uniquely defined (within an additive constant) by the ground state density $n_0(\boldsymbol{r})$. It means that two external potentials that differ by more than a constant and providing the same ground state energy, do not exist. It implies that $n_0(\boldsymbol{r})$ provides all informations to uniquely determine the many-body Hamiltonian and thus the exact total ground state energy E_0. This energy is a functional (a function of a function) of the density :

$$E[n_0] = F_{HK}[n_0(\boldsymbol{r})] + \int V_{ext}(\boldsymbol{r}) n_0(\boldsymbol{r}) d\boldsymbol{r} \tag{2.4}$$

$$F_{HK}[n_0] = T[n_0] + E_{ee}[n_0] \tag{2.5}$$

The term $F_{HK}[n_0]$ describes the universal Hohenberg-Kohn functional and includes the kinetic energy $T[n_0]$ and the electron-electron interaction $E_{ee}[n_0]$. On the other hand, the external potential term governs specifically the system studied. Actually, $F_{HK}[n_0]$ is not known explicitly. It is however possible to decompose it into a classical electrostatic Hartree energy E_H and a non-classical energy E_{ncl} :

$$E_{ee} = \underbrace{\frac{1}{2}\int \frac{n_0(\boldsymbol{r}) n_0(\boldsymbol{r'})}{|\boldsymbol{r} - \boldsymbol{r'}|} d\boldsymbol{r} d\boldsymbol{r'}}_{E_H} + E_{ncl} \tag{2.6}$$

The second Hohenberg-Kohn theorem uses the variational principle on the energy that is a functional of the density. It establishes that $E[n]$ has its minimum at the ground state equilibrium density $n_0(\boldsymbol{r})$ allowing to systematically obtain the ground state energy from trial densities.

$$\left.\frac{\partial E[n(\boldsymbol{r})]}{\partial [n(\boldsymbol{r})]}\right|_{n_0} = 0 \tag{2.7}$$

$$n_0(\boldsymbol{r}) = N \int |\Psi_0(\boldsymbol{r}, \boldsymbol{r}_2, ..., \boldsymbol{r}_N)|^2 d\boldsymbol{r}_2 ... d\boldsymbol{r}_N \tag{2.8}$$

Kohn-Sham equations

As we have seen, the first Hohenberg-Kohn theorem shows that the ground state density gives all necessary information of the system of interest, while the second theorem gives a way to find it. The problem is that the Hohenberg-Kohn functional F_{HK} is not known. A clever way to get around it was found by Kohn and Sham in [18] : their idea is to introduce a reference system of N non-interacting electrons of density $n_s(\boldsymbol{r})$ equals to the density $n(\boldsymbol{r})$ of the system with interacting electrons. Since the wavefunction of a system of non-interacting electron is a slater determinant, the non-interacting density $n_s(\boldsymbol{r})$ is determined completely by single-electron orbitals : the Kohn-Sham wavefunctions $\phi_{KS,i}(\boldsymbol{r})$ simply written $\phi_i(\boldsymbol{r})$ in the following.

$$n_s(\boldsymbol{r}) = \sum_i^N |\phi_i(\boldsymbol{r})|^2 \triangleq n(\boldsymbol{r}) \tag{2.9}$$

The kinetic energy of the reference system T_s (that is supposed to be a major fraction of the kinetic energy of interacting-electron system) can then be obtained from Kohn-Sham orbitals :

$$T_s[n] = \sum_i^N \int \phi_i^*(\boldsymbol{r}) \frac{\nabla^2}{2} \phi_i(\boldsymbol{r}) d\boldsymbol{r} \tag{2.10}$$

Hence, the Hohenberg-Kohn functional can be rewritten as :

$$F_{HK}[n] = T_s[n] + E_H[n] + E_{xc}[n] \tag{2.11}$$

where E_{xc} is known as the exchange correlation functional that accounts for all unknown contributions : the residual part of the kinetic energy, repulsive and correlation effects due to Pauli's exclusion principle and Coulomb interaction :

$$E_{xc} = (T - T_s) + (E_{ee} - E_H) \tag{2.12}$$

The exact form of this exchange functional is unfortunately not known and finding a good approximation of it has been and is still an active field of research. Finally, taking the one-particle Kohn-Sham orbitals ϕ_i as variational parameters leads to the Kohn-Sham equations :

$$\Big(-\frac{1}{2}\nabla^2 + V_{KS}(\boldsymbol{r}) \Big) \phi_i(\boldsymbol{r}) = \epsilon_i \phi_i(\boldsymbol{r}) \tag{2.13}$$

which is a set of N single-electron equations where an electron moves in the the effective Kohn-Sham potential defined as :

$$V_{KS}(\boldsymbol{r}) = V_{ext}(\boldsymbol{r}) + \underbrace{\int \frac{n(\boldsymbol{r})}{|\boldsymbol{r} - \boldsymbol{r'}|} d\boldsymbol{r}}_{V_H(\boldsymbol{r})} + \underbrace{\frac{\delta E_{xc}[n]}{\delta n}}_{V_{xc}(\boldsymbol{r})} \tag{2.14}$$

One has to note that V_{KS} depends on the density and so on the solution of the problem itself. Hence, it is required to use a self-consistent field (SFC) method by starting with an initial guess of the density and iterate (see figure 2.1 for a recap of the method). Typically, the SCF scheme is stopped when a convergence criterion is reached.
The solution of the Kohn-Sham self consistent set of equations 2.13 is in fact equivalent to the minimization of the total energy functional of the KS orbitals :

$$E[\{\phi_i\}] = \sum_i \langle \phi_i | -\frac{1}{2}\nabla^2 | \phi_i \rangle + \int n(\boldsymbol{r}) V_{ext}(\boldsymbol{r}) d\boldsymbol{r} + \frac{1}{2} \int \frac{n(\boldsymbol{r}) n(\boldsymbol{r'})}{|\boldsymbol{r} - \boldsymbol{r'}|} d\boldsymbol{r} d\boldsymbol{r'} + E_{xc}[n] \tag{2.15}$$

under an orthonormalization constraint $\langle \phi_i | \phi_j \rangle = \delta_{ij}$ for the occupied orbitals.
Notice that, by construction, if the exchange-correlation functional is exact, the electronic density and the total energy are also the exact ones. This is why it is often said that DFT is "in principle" an exact theory. However, the Kohn-Sham orbitals ϕ_i and their corresponding eigenenergies ϵ_i do not correspond to real quantities, since they correspond to a fictitious reference system of non-interacting electrons.

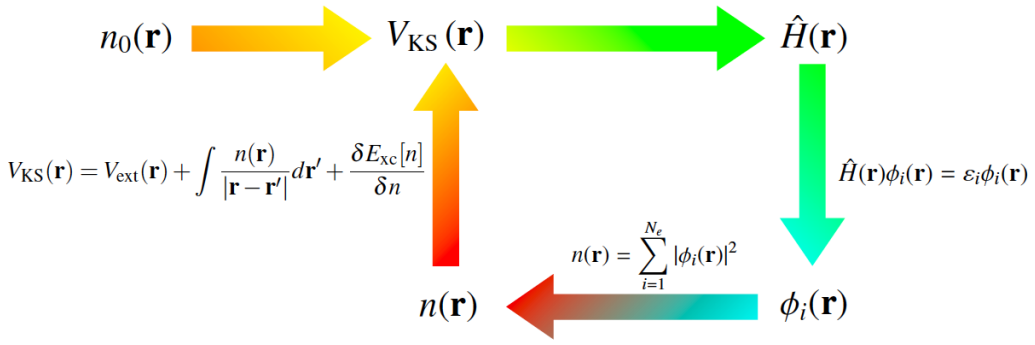

Figure 2.1: Recap of the self-consistent method used in DFT to predict the total energy and the the electronic density of a system of N interacting electrons [16].

Indeed, finding a correct approximation of the exchange-correlation functional E_{xc} is crucial. Among the multitude of exchange-correlation functionals available today, the Local Density Approximation (LDA) is the simplest one and has been the first proposed by Kohn and Sham. It assumes that the charge density slowly varies and hence that each volume element can be described by the density $n(\boldsymbol{r})$ of a uniform electron gas. Using then the exchange-correlation energy $\epsilon_{xc}(\boldsymbol{r}, n)$ per electron in a homogeneous gas (that can be calculated with Quantum Monte Carlo techniques [19]), one finds the exchange-correlation energy for the entire volume :

$$E_{xc}^{LDA}[n] = \int \epsilon_{xc}(\boldsymbol{r}, n) n(\boldsymbol{r}) d\boldsymbol{r} \tag{2.16}$$

It is possible to go beyond LDA by considering informations about the density gradient in the calculation of the exchange-correlation energy per electron. This is known as Generalized gradient approximation (GGA), among which the functional PBE (Perdew, Burk and Burk) is very popular [20]

2.4 Implementation of DFT

Now that the basics of DFT have been introduced, let us see how it is practically implemented in a DFT code such as ABINIT that was used during this master thesis. But first, some words on this software. ABINIT is defined in its website [21] as
" ... a software suite to calculate the optical, mechanical, vibrational, and other observable properties of materials. Starting from the quantum equations of density functional theory, you can build up to advanced applications with perturbation theories based on DFT, and many-body Green's functions (GW and DMFT) . ABINIT can calculate molecules, nanostructures and solids with any chemical composition, and comes with several complete and robust tables of atomic potentials. On-line tutorials are available for the main features of the code, and several schools and workshops are organized each year." ABINIT is a project that favors development and collaboration. It is distributed under the GNU General Public License (like Linux).
Actually, the short description below is more general than just the implementation of DFT

in ABINIT, it can be transposed to DFT softwares that are based on plane-waves and periodic conditions. The following is inspired by [16] and more details can be found in [22].

Bloch theorem and plane wave basis set

A crystal is a solid in which the atoms are packed regularly with a repeating pattern (the primitive cell). The lattice can thus be defined by its primitive vectors $\boldsymbol{a}_1$, $\boldsymbol{a}_2$, $\boldsymbol{a}_3$ (often referred as $\boldsymbol{a}$, $\boldsymbol{b}$, $\boldsymbol{c}$) that allow to locate any point of the lattice : $\boldsymbol{R} = l\boldsymbol{a_1} + m\boldsymbol{a_2} + n\boldsymbol{a_3}$. This primitive cell has a volume $\Omega = \boldsymbol{a_1}.(\boldsymbol{a_2} \times \boldsymbol{a_3})$. One can also define the asymmetric unit which is the smallest part of the cell from which it is possible to construct entirely the primitive cell by applying symmetry operations of the system (this is what defines the space group).
As we work with periodic system, Bloch theorem applies : it stipulates that the general form of the wavefunction in a periodic crystal takes the form :

$$\phi_{n\boldsymbol{k}}(\boldsymbol{r}) = e^{i\boldsymbol{k}.\boldsymbol{r}} u_{n\boldsymbol{k}}(\boldsymbol{r}) \tag{2.17}$$

where $u_{n\boldsymbol{k}}(\boldsymbol{r})$ has the periodicity of the crystal such that $u_{n\boldsymbol{k}}(\boldsymbol{r}) = u_{n\boldsymbol{k}}(\boldsymbol{r} + \boldsymbol{R})$ and $\phi_{n\boldsymbol{k}}(\boldsymbol{r})$ is called the Bloch wave. This spatial periodicity suggests to write $u_{n\boldsymbol{k}}(\boldsymbol{r})$ as a spatial Fourier expansion :

$$u_{n\boldsymbol{k}}(\boldsymbol{r}) = \sum_{\boldsymbol{G}} \tilde{u}_{n\boldsymbol{k}}(\boldsymbol{G}) e^{i\boldsymbol{G}.\boldsymbol{r}} \tag{2.18}$$

with $\tilde{u}_{n\boldsymbol{k}}(\boldsymbol{G})$ the Fourier coefficients defined as :

$$\tilde{u}_{n\boldsymbol{k}}(\boldsymbol{G}) = \frac{1}{\Omega} \int_{\Omega} u_{n\boldsymbol{k}}(\boldsymbol{r}) e^{-i\boldsymbol{G}.\boldsymbol{r}} d\boldsymbol{r} \tag{2.19}$$

We have introduced here the reciprocal lattice vector $\boldsymbol{G} = u\boldsymbol{b_1} + v\boldsymbol{b_2} + w\boldsymbol{b_3}$ that is defined such that $e^{i\boldsymbol{G}.\boldsymbol{R}} = 1$. In that way, $\boldsymbol{b_1} = \frac{2\pi}{\Omega}(\boldsymbol{a_2} \times \boldsymbol{a_3})$, $\boldsymbol{b_2} = \frac{2\pi}{\Omega}(\boldsymbol{a_3} \times \boldsymbol{a_1})$, $\boldsymbol{b_3} = \frac{2\pi}{\Omega}(\boldsymbol{a_1} \times \boldsymbol{a_2})$. Finally, the Bloch wavefunction of state n with a wave-vector $\boldsymbol{k}$ writes :

$$\phi_{n\boldsymbol{k}}(\boldsymbol{r}) = \sum_{\boldsymbol{G}} \tilde{u}_{n\boldsymbol{k}}(\boldsymbol{G}) e^{i(\boldsymbol{k}+\boldsymbol{G}).\boldsymbol{r}} \tag{2.20}$$

Numerically speaking, this infinite sum should be truncated. The number of plane waves to consider in the sum is given by a threshold value of the kinetic energy that is called the maximum kinetic energy cut-off named E_{cut} in ABINIT : $\frac{(\boldsymbol{k}+\boldsymbol{G})^2}{2} < E_{cut}$ (it comes from the term $-\frac{1}{2}\nabla^2 e^{i(\boldsymbol{k}+\boldsymbol{G}).\boldsymbol{r}}$ of the Hamiltonian). When computing any property in DFT, one should always check the convergence of this property with respect to this cut-off energy.

Brillouin zone integration

In periodic systems, computing quantities like the density implies a summation on all the bands (or "states") and an integration over the whole Brillouin Zone (BZ) which is defined as the the primitive cell in the reciprocal space. This BZ can be further reduced to the Irreducible Brillouin zone (IBZ) by considering symmetry operations by rotation and inversion.

In practice, this integration is replaced by a weighted sum over a set of special k-points (this is allowed because generally, the wavefunction and other properties vary smoothly over the BZ). One can also integrate using a Monkhorst-Pack grid [23] which is a grid of $n_{\boldsymbol{k}1} \times n_{\boldsymbol{k}2} \times n_{\boldsymbol{k}3}$ points uniformly spaced as depicted on figure 2.2. As always in DFT, the choice of the k-point sampling is a trade off between computational time and the desired precision on the property of interest (as for the cut-off energy, convergence study should be performed).

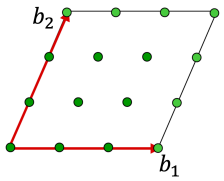

Figure 2.2: Monkhorst-Pack grid of 3x3x3, adapted from [16].

Pseudopotential

Fourier analysis teaches us that, roughly speaking, the more details we want in real space, the more plane waves we have to add with high k-vector norm in the sum 2.18. This can be computationally problematic to describe localized features such as the core orbitals. This problem can be solved by using what we call a pseudopotential. The basic idea is simple : it is assumed that the behaviour of core electrons in the bonding environment of the crystal is approximately the same than the one of those core electrons in an atomic environment. Since chemical bonds involve valence electrons, highly localized core electrons have only little influence on the overall material properties of a solid. In this spirit, the ≪frozen-core approximation≫ consists in averaging the core of an atom (nucleus and core electrons) and only consider valence electrons in the computation.
The pseudopotential (PP) method goes one step further by performing a pseudization of the valence electrons. It means that an all-electron calculation is performed for an atom at a reference energy. Then, a cutoff radius r_c is selected such that the pseudo and all-electron valence eigenstates have the same energies and amplitude (and thus density) outside r_c. A simplified pseudo wavefunction and a pseudopotential are constructed (see figure 2.3). This pseudization allows one also to soften out the quick oscillations of wavefunctions in the core region that comes from orthogonality criterion. To recap in one sentence, the system is reduced to a limited amount of pseudo-wavefunctions describing the valence electrons moving in pseudopotentials approximating the atomic cores. This technique is useful since its reduces the number of plane waves needed to describe the system and so it decreases the computational load. Within this approximation, the KS equation and the density are rewritten as:

$$\left(-\frac{1}{2}\nabla^2 + V_{PP} \right) \phi_i^{PP}(\boldsymbol{r}) = \epsilon_i^{PP} \phi_i^{PP}(\boldsymbol{r}) \tag{2.21}$$

$$n(\boldsymbol{r}) = \sum_i |\phi_i^{PP}(\boldsymbol{r})|^2 \tag{2.22}$$

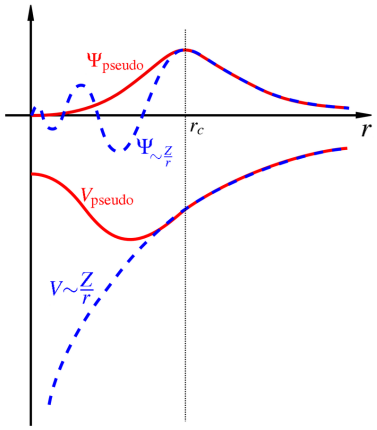

Figure 2.3: Comparison of a wavefunction in the Coulomb potential of the nucleus (blue) to the one in the pseudopotential (red). The real and the pseudo-wavefunction and potentials match above a certain cutoff radius. Image and caption from [24].

It exists different ways to construct those pseudopotentials. We describe here briefly what was used during this master thesis : *norm conserving* (NC) pseudopotentials and projector augmented wave method (PAW).

Norm conserving The idea of NC pseudopotential is to set, within the core, the electron density based on the pseudopotential approach equals to the the one based on all-electron (AE) approach. The criterion is thus :

$$\int_0^{r_c} |\phi_i^{PP}|^2 d\boldsymbol{r} = \int_0^{r_c} |\phi_i^{AE}|^2 d\boldsymbol{r} \tag{2.23}$$

PAW Projector-augmented wave (PAW) potential may be classified as a frozen-core all-electrons potential. It was first proposed by Blöchl in 1994 [25] and adopted by Kresse and Joubert in 1999 [26] and it looks for the efficiency of the pseudopotential approach while keeping the accuracy of the all-electron potential. It divides core and valence wavefunctions into two separate descriptions as shown in 2.4.
The ϕ^{inter} of the valence part is decomposed with the plane wave expansion, while the ϕ^{core} of the core part is projected on a radial grid at the atom center. The overlapping part, ϕ^{net}, is then trimmed off to obtain the final wavefunction, ϕ^{PAW}, which is very close to the all-electron wavefunction:

$$\phi^{PAW} = \phi^{core} + \phi^{inter} + \phi^{net} \tag{2.24}$$

Thank's to the use of ϕ^{core}, the core part is well reproduced, and many plane waves become unnecessary in the expansion of ϕ^{inter}, leading to much less computational effort.

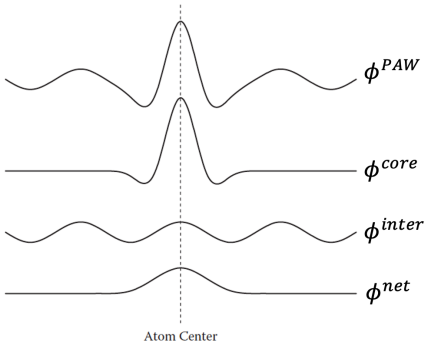

Figure 2.4: Schematic illustration of the wavefunction components used for the construction of PAW. Adapted from [22]

2.5 Crystals lattice vibration within DFT

As we will see in the following chapter, lattice vibrations are a key aspect of luminescence theory. Let us summarize the formalism of lattice dynamics in crystals as calculated in DFT. Only the key equations will be given following the review of F. Giustino on electron-phonon interaction from first principles [27], a complete derivation can be found in [28]. Note that it was decided to follow the notations of article [27] that are classical notations for the field. Those notations will be only used in this section.
We consider M nuclei in the unit cell that are located by their cartesian coordinates $\tau_{\kappa\alpha}$ where κ and α stand respectively for the nuclei label and cartesian direction x,y,z. The system is defined as a large supercell with Born-von Karman (BvK) periodic boundary conditions. It contains N_p units cells identified by their lattice vector $\boldsymbol{R}_p$ with p going from 1 to N_p. The position of nucleus κ in unit cell p is given by $\boldsymbol{\tau}_\kappa = \boldsymbol{R}_p + \boldsymbol{\tau}_\kappa$. The Bloch wavevectors $\boldsymbol{q}$ defines a uniform grid of N_p points in one unit cell of the reciprocal lattice. The idea is to use the total potential energy $U(\{\boldsymbol{\tau}_{\kappa p}\})$ of electrons and nuclei in the BvK supercell (the braces indicate that we take the coordinates of all ions into account). This potential energy is calculated with the electrons in their ground state with the nuclei acting as classical particles clamped to their coordinates $\boldsymbol{\tau}_{\kappa p}$. This energy is a common output variable that DFT software such as ABINIT can provide. We begin by expanding the total potential energy to the second order (harmonic approximation) with respect to the displacement of the ions $\Delta\tau_{\kappa\alpha p}$ away from their equilibrium position.

$$U = U_0 + \frac{1}{2} \sum_{\substack{\kappa\alpha p \\ \kappa'\alpha' p'}} \frac{\partial^2 U}{\partial \tau_{\kappa\alpha p} \partial \tau_{\kappa'\alpha' p'}} \Delta\tau_{\kappa\alpha p} \Delta\tau_{\kappa'\alpha' p'} \tag{2.25}$$

where U_0 is the total energy calculated with the ions in their respective equilibrium positions. First-order terms are vanishing since the system is at equilibrium, no forces are expected. The second derivative with respect to nuclei displacements is known as the matrix of interatomic force constants (IFC):

$$C_{\kappa\alpha p, \kappa'\alpha' p'} = \frac{\partial^2 U}{\partial \tau_{\kappa\alpha p} \partial \tau_{\kappa'\alpha' p'}} \tag{2.26}$$

This matrix can be easily computed by ABINIT software by moving one atom at a time and looking at the change in energy. This can be done in standard density functional perturbation theory (DFPT). The Fourier transform of the IFC matrix gives the "dynamical matrix" ([29]):

$$D_{\kappa\alpha,\kappa'\alpha'}(\boldsymbol{q}) = \frac{1}{\sqrt{M_\kappa M_{\kappa'}}} \sum_p C_{\kappa\alpha 0,\kappa'\alpha' p} e^{i\boldsymbol{q}.\boldsymbol{R}_p} \tag{2.27}$$

with M_κ the mass of κ-th ion. This dynamical matrix is Hermitian and consequently admits real eigenvalues, known as the eigenfrequencies $\omega^2_{\boldsymbol{q}\nu}$:

$$\sum_{\kappa'\alpha'} D_{\kappa\alpha,\kappa'\alpha'}(\boldsymbol{q}) e_{\kappa'\alpha',\nu}(\boldsymbol{q}) = \omega^2_{\boldsymbol{q}\nu} e_{\kappa'\alpha',\nu}(\boldsymbol{q}) \tag{2.28}$$

where the index ν runs from 1 to 3M and design the 'mode' label. From a classical point of view, those eigenfrequencies correspond to the vibrational frequencies of independent harmonic oscillators. Since the dynamical matrix is hermitian, the eigenvectors $e_{\kappa\alpha,\nu}(\boldsymbol{q})$ verify orthonormal and completeness relations for each $\boldsymbol{q}$:

$$\sum_\nu e^*_{\kappa'\alpha',\nu}(\boldsymbol{q}) e_{\kappa\alpha,\nu}(\boldsymbol{q}) = \delta_{\kappa\kappa'}\delta_{\alpha\alpha'} \tag{2.29}$$

$$\sum_{\kappa\alpha} e^*_{\kappa\alpha,\nu}(\boldsymbol{q}) e_{\kappa\alpha,\nu'}(\boldsymbol{q}) = \delta_{\nu\nu'} \tag{2.30}$$

Those vectors are called the "normal modes" of vibration. Finally, we can also write the Hamiltonian for nuclei considered as quantum particles :

$$H_{\mathrm{p}} = \frac{1}{2} \sum_{\kappa\alpha p} C_{\kappa\alpha p,\kappa'\alpha' p'} \Delta\tau_{\kappa\alpha p} \Delta\tau_{\kappa'\alpha' p'} - \sum_{\kappa\alpha p} \frac{\hbar^2}{2M_\kappa} \frac{\partial^2}{\partial\tau^2_{\kappa\alpha p}} \tag{2.31}$$

2.6 Impurities within DFT, the super-cell method

The main goal of this work is to study the luminescent properties of a bulk solid ($Sr[Li_2Al_2O_2N_2]$) that is doped with impurity atoms (europium) that will play the role of optical centers in the lattice. The presence of a small amount of such impurities is crucial to obtain the desired luminescent properties.

A first important feature of such doping is that the doping agents (here europium) are not periodically arranged in the lattice. This means that, strictly speaking, the DFT method based on periodic boundary conditions we described previously is not suitable for such calculation. One way to get around this problem is to model the defect in a supercell, consisting of the defect surrounded by a few dozen to a few hundred atoms of the bulk. The system is then repeated periodically throughout space [30].

A second feature appears to be more problematic : experimental doping rates are quite small (0.7 % for the experimental study on SALON:Eu^{2+}), this means that, if we want to reproduce this doping rate, the number of atoms to put in the simulation will be very large (nearly 1300 for our situation) which is computationally way too demanding. For instance, in this work, it was decided to use a supercell composed of 54 atoms for most of the studies (doping rate of 16.67%) that resulted from a trade-off between computational

time saving and minimization of overlap between $5d_{z^2}$ orbitals of neighbouring europium that is unphysical (see the section dedicated to the supercell choice in the results chapter for more details). This means that when simulating the properties of the doped material, we must keep in mind that the use of supercells implies that the isolated defect is replaced by a periodic array of defects. Since the doping rate is quite high, such periodic array may contain artificial interactions between the defects that can lead to unphysical results. Still, it will be shown that this choice of doping rate is sufficient to predict correctly the luminescent properties of the material of interest.

Chapter 3

Theory of photoluminescence

Contents

Luminescence in solids is the phenomenon by which electronic states of solids are excited by some energy from an external source and the excitation energy is released as light. When the energy comes from short-wavelength light, usually ultraviolet or visible light, the phenomenon is called photoluminescence.
The understanding of such phenomenon of interaction of radiation with a physical system is usually split in three parts : 1) Treatment of the radiation alone. 2) Treatment of the physical system alone (here a solid). 3) Treatment of their interactions. In this chapter, we will try to follow this understanding process. In addition to this usual splitting, we will also first describe the process of emission or absorption of light in a simplified two-level atom, this simplified "atomic" point of view will be very useful to generalize then to an optical center incorporated in a solid lattice.
In the first section of this chapter, the radiation will be treated by means of Einstein coefficients [1]. A link will be made between those coefficients and the dipole matrix elements of the transition for a simple two-level system.
In the second section, we will show how a solid can be treated quantum mechanically by the means of Born-Oppenheimer approximation. In the third section, we will treat our solid as frozen and see how the electronic eigenenergies of an optical center are influenced by the crystal (with a focus of the energies of interest for this work : the 4f and 5d energies in Lanthanide). In the next chapter, we will remove the frozen lattice condition and see how we can study the radiative processes of interest in a vibrating lattice. Finally, with all these ingredients in mind, the configuration coordinate model, that allows one to predict emission spectra and other important luminescent properties, will be extensively presented in the two last sections.

3.1 Absorption and emission of light by impurity atoms

Emission of light we are interested in comes from a small number of impurities generally intentionally incorporated in a crystal matrix (in the case of this master thesis, europium atoms replace strontium atoms in bulk SALON). These impurities can be excited (by the means of photon absorption in the case of photoluminescence) and go back to their ground state by emitting light. This system is called an emitting center. In this section, we will see how these emitting centers can absorb or emit light and how we can quantitatively describe these phenomena from an atomic point of view.
We simplify the problem by only considering a two-level center with energy levels E_1 and E_2 (with $E_2 - E_1 = \hbar\omega_{21}$) that is perturbed by an electromagnetic radiation of energy density $u(\omega)$. This system can undergo 3 processes : absorption of a photon, stimulated emission and spontaneous emission of photon (see figure 3.1). Absorption and stimulated emission can be treated in a semi-classical way (energy levels=quantum, light=classical electromagnetic wave) by the means of perturbation theory as we will see. To be fully explained, spontaneous emission requires however to quantize electromagnetic field, which is more complex. Luckily, a clever thermodynamical argument based on Einstein coefficients allows us to make the link between spontaneous emission and the two other phenomena.

[1] Indeed, a full understanding of this subject would require to quantize electromagnetic field but since the results we need are accessible from the simpler Einstein approach, only the latter will be exposed.

Let us begin by explaining this link.

3.1.1 Einstein coefficients

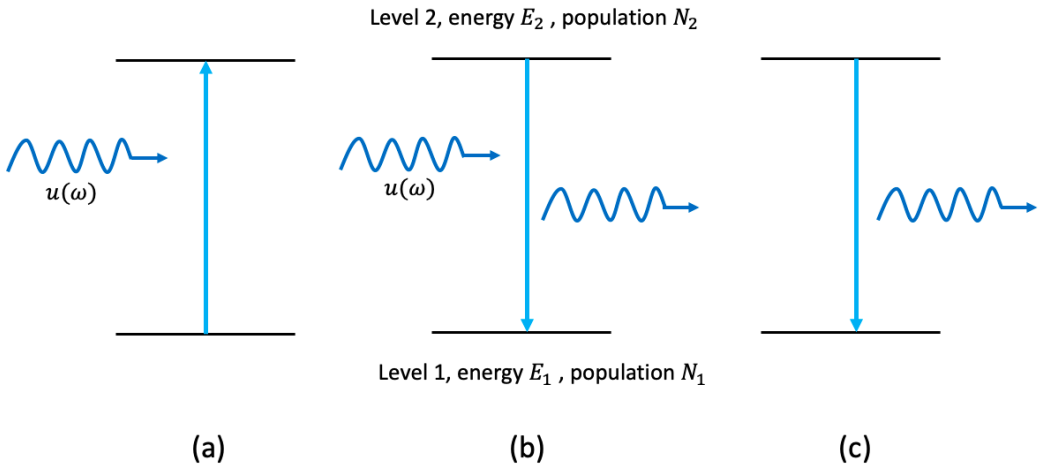

Figure 3.1: Light can interact with matter by 3 processes : (a) absorption (b) stimulated emission (c) spontaneous emission.

The following reasoning is inspired by [31]. We consider that at each time, a system in state 1 can absorb an electromagnetic energy quantum, and make a transition to state 2. Similarly, at each time, a system in state 2 can emit spontaneously an electromagnetic energy quantum, or emit it because it is stimulated by the electromagnetic field. Statistically, for a large ensemble of systems, the number of spontaneous transitions is proportional to the population in state 2, as well as to the inverse of a lifetime, parameterised by the so-called Einstein coefficient A. The transition rates for level 1 to level 2 absorption, or for level 2 to level 1 stimulated emission depend on the level 1 (or level 2) populations and are proportional to the Einstein B coefficient, but also on the energy density of the electromagnetic radiation. This is summarized by this set of equations :

$$\frac{dN_1}{dt} = -B_{12}N_1u(\omega) \qquad \frac{dN_2}{dt} = -B_{21}N_2u(\omega) \qquad \frac{dN_2}{dt} = -A_{21}N_2 \tag{3.1}$$

Consider a set of such 2-levels systems at thermal equilibrium at temperature T. By equating the number of photons absorbed and emitting and considering that A and B coefficients do not depend on temperature (since they characterise only the interaction of a system with one photon and should not depend on temperature), it gives :

$$B_{12}N_1(T)u(\omega,T) = A_{21}N_2(T) + B_{21}N_2(T)u(\omega,T) \tag{3.2}$$

Assuming that the populations of two level systems are governed by Maxwell-Boltzmann statistics

$$\frac{N_2(T)}{N_1(T)} = e^{-\frac{\hbar\omega}{k_BT}} \tag{3.3}$$

and by combining equations 3.2 and 3.3, we can write :

$$B_{12} = e^{-\frac{\hbar\omega}{k_B T}} \left(\frac{A_{21}}{u(\omega, T)} + B_{21} \right) \tag{3.4}$$

Quantizing electromagnetic field leads to a spectral energy density at temperature T that is governed by Bose-Einstein statistics (black-body radiation) :

$$u(\omega, T) = \frac{n_D \hbar \omega^3}{\pi^2 c^3} \frac{1}{e^{\frac{\hbar\omega}{k_B T}} - 1} \tag{3.5}$$

with n_D the refractive index of the material and c the speed of light. After some manipulations, it gives :

$$B_{12} = \left[\frac{\pi c^3}{n_D \hbar \omega^3} A_{21} + e^{-\frac{\hbar\omega}{k_B T}} \left(B_{21} - \frac{\pi c^3}{n_D \hbar \omega^3} A_{21} \right) \right] \tag{3.6}$$

This equality must be true for all temperatures, the second term must vanish! This leads finally to the link between A and B coefficients :

$$A_{21} = \frac{n_D \hbar \omega^3}{\pi c^3} B_{21} \qquad B_{12} = B_{21} \tag{3.7}$$

3.1.2 Electronic dipole transition probability

Thanks to the Einstein model, we have obtained a mathematical link between Einstein A and B coefficients. We will see in the following two subsections how we can compute B coefficients with time-dependent perturbation theory. Einstein A coefficient will then be simply given by equation 3.7. For pedagogical reason, the method that will be shown is based on the fact that the system is not incorporated in a solid. Still, it will provide useful results that remain valid for the study of solids. Our two-level system is governed by time-dependent Schrödinger equation :

$$H \left| \Psi \right\rangle = i\hbar \frac{\partial \left| \Psi \right\rangle}{\partial t} \tag{3.8}$$

where $H = H_0 + V$ is composed of the unperturbed Hamiltonian H_0 and V is the perturbation. In the semi-classical approach, the light–atom interaction is given by the energy shift of the atomic dipole in the electric field of the light of frequency ω that is supposed to travel along z direction : $\boldsymbol{E_0} = (0, 0, E_0) cos(\omega t)$

$$V(t) = -e\boldsymbol{r}.\boldsymbol{E}(t) = -e\boldsymbol{r}.\boldsymbol{E_0} cos(\omega t) = -e\boldsymbol{r} E_0 \frac{e^{i\omega t} + e^{-i\omega t}}{2} \tag{3.9}$$

with $-e$ the charge of the concerned electron. The solution of Schrödinger equation for the unperturbed system can be written as :

$$\left| \Psi_{unperturbed} \right\rangle = c_1(t) \left| \psi_1 \right\rangle e^{\frac{-iE_1 t}{\hbar}} + c_2(t) \left| \psi_2 \right\rangle e^{\frac{-iE_2 t}{\hbar}} \tag{3.10}$$

with

$$H_0 \left| \psi_1 \right\rangle = E_1 \left| \psi_1 \right\rangle \qquad H_0 \left| \psi_2 \right\rangle = E_2 \left| \psi_2 \right\rangle \tag{3.11}$$

The idea is then to inject the solution 3.10 into equation 3.8 and project the result on $\langle\psi_1|$ and $\langle\psi_2|$ to obtain differential equations linking $c_1(t)$ and $c_2(t)$. To do this, it is imposed first that $\langle\psi_i|\psi_j\rangle = \delta_{ij}$. Then the perturbation matrix elements are written as :

$$V_{ij}(t) = \frac{E_0}{2}(e^{i\omega t} + e^{-i\omega t})\boldsymbol{\mu}_{ij} \tag{3.12}$$

with $\boldsymbol{\mu}_{ij}$ the dipole matrix element defined as $\boldsymbol{\mu}_{ij} = -e\langle\psi_i|\boldsymbol{r}|\psi_j\rangle$. Since $\boldsymbol{r}$ is an odd parity operator, we have $\boldsymbol{\mu}_{ij} = 0$ if $i = j$. Moreover, the dipole matrix element represents a measurable quantity and must be real, which implies that $\boldsymbol{\mu}_{ij} = \boldsymbol{\mu}_{ij}$ because $\boldsymbol{\mu}_{ij} = \boldsymbol{\mu}_{ij}^*$. Using all these informations and after some manipulations, we end-up with two coupled differential equations (the derivation can be found in any quantum optic textbook such as [32]):

$$\begin{cases} \dot{c}_1(t) = i\frac{E_0\boldsymbol{\mu}_{12}}{2\hbar}\left(e^{i(\omega-\omega_{21})t} + e^{-i(\omega+\omega_{21})t}\right)c_2(t) \\ \dot{c}_2(t) = i\frac{E_0\boldsymbol{\mu}_{12}}{2\hbar}\left(e^{-i(\omega-\omega_{21})t} + e^{i(\omega+\omega_{21})t}\right)c_1(t) \end{cases} \tag{3.13}$$

Actually, this system of differential equations does not have simple analytical solutions. Some appropriate approximations must be done. In our case, we can first assume that we are in the weak-field limit (low electric field amplitude and thus small perturbation). The number of transitions expected is small, and it will always be the case that $c_1(t) \gg c_2(t)$. We can put $c_1(t) \approx 1$ for all t and thus $\dot{c_1}(t) \approx 0$. Solving the second equation gives for $c_2(t)$:

$$c_2(t) = \frac{iE_0\boldsymbol{\mu}_{12}}{2\hbar}\left[\frac{e^{-i\delta\omega t} - 1}{-i\delta\omega} + \frac{e^{i(\omega+\omega_{21})t} - 1}{i\left(\omega + \omega_{21}\right)}\right] \tag{3.14}$$

with $\delta = \omega - \omega_{21}$ the detuning. Supposing that $\omega \approx \omega_{21}$, we neglect the second term in the brackets that is much smaller than the first term (rotating wave approximation).This gives :

$$c_2(t) = \frac{iE_0\boldsymbol{\mu}_{12}}{2\hbar}\left[\frac{e^{-i\delta\omega t} - 1}{-i\delta\omega}\right] = \frac{iE_0\boldsymbol{\mu}_{12}}{2\hbar}\left[\frac{e^{-i\frac{\delta t}{2}}(e^{-i\frac{\delta t}{2}} - e^{+i\frac{\delta t}{2}})}{-i\delta\omega}\right] \tag{3.15}$$

$$|c_2(t)|^2 = \left(\frac{E_0\boldsymbol{\mu}_{12}}{2\hbar}\right)^2\left(\frac{\sin\left(\frac{\delta t}{2}\right)}{\frac{\delta}{2}}\right)^2 \tag{3.16}$$

Actually, this result is not totally correct : transitions are not infinitely sharps, spectral lines present finite width $\Delta\omega$. Hence, this must be integrated around ω_{21} by taking into account the spectral energy density $u(\omega)$ of the source defined such that $\frac{1}{2}\epsilon_0 E_0^2 = \int u(\omega)d\omega$.

$$|c_2(t)|^2 = \frac{\boldsymbol{\mu}_{12}^2}{2\epsilon_0\hbar^2}\int_{\omega_{21}-\Delta\omega/2}^{\omega_{21}+\Delta\omega/2} u(\omega)\left(\frac{\sin(\omega-\omega_{21})\frac{t}{2}}{\frac{\omega-\omega_{21}}{2}}\right)^2 d\omega = \frac{\boldsymbol{\mu}_{12}^2\pi}{\epsilon_0\hbar^2}u(\omega_{21})t \tag{3.17}$$

The last equality is obtained by considering that $u(\omega)$ is nearly constant within the integral limits and by using the definite integral $\int_{-\infty}^{+\infty}\frac{\sin^2(ax)}{x^2} = \pi a$. Notice that we can use these integral limits because at long t, the integrand peaks around ω_{21} and is approximately 0 elsewhere.

3.1.3 Connection with Einstein coefficients

We can now relate the result of equation 3.17 to Einstein B coefficient defined as :

$$\frac{dN_2}{dt} = -B_{21}u(\omega_{21})N_2 \tag{3.18}$$

which says that the transition probability per unit time per atom is $B_{21}u(\omega_{21})$. In the derivation we assumed implicitly that the atomic dipole moment was aligned parallel to the polarization vector of the light. However, in a collection of atoms, the direction of the atomic dipoles will be random. If the angle between the polarization and a given dipole is θ, then we have to take the average of $\boldsymbol{\mu}_{12}\cos^2(\theta)$ for all the atoms. Using $<\cos^2(\theta)>= 1/3$, we replace $\boldsymbol{\mu}_{12}^2$ by $\boldsymbol{\mu}_{12}^2/3$. This gives finally the transition probability rate W_{12} as :

$$W_{12} = B_{12}u(\omega_{21}) = \frac{|c_2(t))|^2}{t} = \frac{\pi}{3\epsilon_0\hbar^2}\boldsymbol{\mu}_{12}^2 u(\omega_{21}). \tag{3.19}$$

This allows us to write an expression for Einstein coefficients based on the dipole matrix element and using the link between A and B coefficients of previous chapter :

$$B_{12} = B_{21} = \frac{\pi}{3\epsilon_0\hbar^2}\boldsymbol{\mu}_{12}^2 \qquad A_{21} = \frac{n_D\omega_{21}^3}{3\epsilon_0\pi\hbar c^3}\boldsymbol{\mu}_{12}^2 \tag{3.20}$$

3.1.4 Light intensity of emission and absorption

Generally, the intensity of light is measured as the number of photons detected per second trough a unit area perpendicular to the direction of light. The spontaneous emission intensity of a simple two-level atom at frequency ω_{21} is thus expressed as the transition probability per second through the Einstein A coefficient [33] :

$$I(\omega_{21}) = A_{21} = \frac{n_D\omega_{21}^3}{3\pi\hbar\epsilon_0 c^3}\boldsymbol{\mu}_{12}^2 \tag{3.21}$$

If we extend this equation to account for any transitions between any states i and j, it gives :

$$I(\hbar\omega) = \frac{n_D\omega^3}{3\pi\hbar\epsilon_0 c^3}\sum_{ij}\boldsymbol{\mu}_{ij}\delta(\hbar\omega_{ij} - \hbar\omega) \tag{3.22}$$

with $\hbar\omega_{ij} = E_i - E_j$.
We see that the intensity of a transition is proportional to the squared dipole matrix element of this transition. Notice also the cubic power dependence to ω for the emission that indeed will have an effect on any emission spectrum. It is often convenient to work with radiative lifetime τ_{21} defined as the inverse of spontaneous emission probability :

$$\tau_{21} = (A_{21})^{-1} \tag{3.23}$$

If they are many terminal states, then the total decay rate of the emitting center is determined by a sum of the transition probabilities of all final states n:

$$A_2 = \sum_n A_{2n} \tag{3.24}$$

The number of excited atoms decreases exponentially ($\propto e^{-t/\tau_{21}}$) with a time constant τ_{21} called the natural lifetime. Since atoms go back to their ground state with photon emission, we call it a radiative process. However, in general, the real life time of the excited state is also controlled by non-radiative processes with decay rate A_{nr}. From that, it is possible to define what is called the quantum efficiency of the emitting center as :

$$\eta = \frac{A_2}{A_2 + A_{nr}} \tag{3.25}$$

3.1.5 Selection rules

We have seen that the transition probability depends on the electric dipole matrix elements $\boldsymbol{\mu}_{12} \propto \langle \psi_1 | \boldsymbol{r} | \psi_2 \rangle$. This type of transition (induced by the interaction of the electric field of the incident wave and the electric dipole moment) is called *electric dipole transition* and is allowed when $\boldsymbol{\mu}_{12} \neq 0$. Since the operator $\boldsymbol{r}$ has odd parity, $\boldsymbol{\mu}_{12}$ is zero whenever the wavefunctions ψ_1 and ψ_2 have the same parity. Thus, electric dipole transition is allowed when initial and final states have opposite parity (parity of a state is given by $(-1)^l$, with l the orbital quantum number), this is the *Laporte rule*. Conversely, it can be shown that *magnetic dipole transition* (interaction of the center with the magnetic field of the incident wave) is allowed for states with the same parity. However, this type of transition is much weaker than electric dipole transition. More generally, by adding other interactions (such as electron-electron or spin-orbit), transition rules read [34]:

- For ${}^{2S+1}L$ terms, allowed transition are when $\Delta S = 0$ and $\Delta L \neq 0$
- For ${}^{2S+1}L_J$ states ($J = L + S$), it becomes $\Delta J = \pm 1, 0$ but $J = 0$ to $J = 0$ is forbidden.

Effect of the crystal

Until now, we have considered that the the electric field perceived by the center was the electric field of the incident radiation $\boldsymbol{E}_0$. However, in dense media such as crystals, a correction must be added to take into account the actual local electric field $\boldsymbol{E}_{loc}$ acting on valence electrons of the center. To do that, the factor $|\boldsymbol{\mu}_{12}|^2$ must be replaced by $(\boldsymbol{E}_{loc}/\boldsymbol{E}_0)^2 |\boldsymbol{\mu}_{12}|^2$. Another important effect is to consider the fact that the eigenfunctions ψ_1 and ψ_2 needed to evaluate the matrix element $\boldsymbol{\mu}_{12}$ are no longer those of the free ion but those of the ion in the crystal. Therefore, the established selection rules can be modified. Nevertheless, the Laporte rule stays valid in local environment with inversion symmetry. This is because the parity character of the free-ion eigenfunctions is still preserved under inversion.

3.2 Quantum theory of solids

Let us consider a solid composed of n electrons of mass m (labelled by $i = 1, 2, ..., n$) at position $\boldsymbol{r}_i$ and momenta $\boldsymbol{p}_i$ and N nuclei labelled by $l = 1, 2, ..., N$ of mass M_l, charge Z_l at position $\boldsymbol{R}_l$ and momenta $\boldsymbol{P}_l$. The Hamiltonian, if spin-orbit interaction and other small effects are neglected, can be written as :

$$H = \sum_{i=1}^{n} \frac{\boldsymbol{p}_i^2}{2m} + \sum_{l=1}^{N} \frac{\boldsymbol{P}_l^2}{2M_l} + V(\boldsymbol{r}_i, \boldsymbol{R}_l) \tag{3.26}$$

In this equation, the potential term can be decomposed into three parts, accounting respectively for electron-electron V_{ee}, nuclei-nuclei V_{nn}, nuclei-electron V_{ne} interactions :

$$V(\boldsymbol{r}_i, \boldsymbol{R}_l) = \underbrace{\sum_i \sum_{j<i} \frac{e^2}{|\boldsymbol{r_i} - \boldsymbol{r_j}|}}_{V_{ee}} + \underbrace{\sum_l \sum_{m<l} \frac{e^2 Z_l Z_m}{|\boldsymbol{R_l} - \boldsymbol{R_m}|}}_{V_{nn}} - \underbrace{\sum_i \sum_l \frac{e^2 Z_l}{|\boldsymbol{R}_l - \boldsymbol{r}_i|}}_{V_{ne}} \tag{3.27}$$

The stationary states of the system are obtained by solving time-independent Schrödinger equation. Using the general definition of momentum operator ($\boldsymbol{p} = -i\hbar\nabla$), it gives :

$$H\Psi(\boldsymbol{r}_i, \boldsymbol{R}_l) = -\frac{\hbar^2}{2m} \sum_{i=1}^{n} \nabla_i^2 \Psi - \frac{\hbar^2}{2} \sum_{l=1}^{N} \frac{\nabla_l^2}{M_l} \Psi + V\Psi = E\Psi(\boldsymbol{r}_i, \boldsymbol{R}_l) \tag{3.28}$$

3.2.1 Born-Oppenheimer approximation

The starting point of the so-called Born-Oppenheimer (B-O) approximation (or adiabatic approximation) is to assume an eigensolution of equation 3.28 of the type :

$$\Psi(\boldsymbol{r}_i, \boldsymbol{R}_l) = \chi(\boldsymbol{R}_l)\psi(\boldsymbol{r}_i, \boldsymbol{R}_l) \tag{3.29}$$

We can replace this solution into equation 3.28. We write :

$$-\frac{\hbar^2}{2m}\chi \sum_i \nabla_i^2 \psi - \frac{\hbar^2}{2} \sum_l \frac{\nabla_l^2}{M_l} \chi\psi + V\chi\psi = E\chi\psi \tag{3.30}$$

with

$$\nabla_l^2 \chi\psi = \chi\nabla_l^2\psi + \psi\nabla_l^2\chi + 2\nabla_l\chi\nabla_l\psi \tag{3.31}$$

If we assume a weak dependence of the electronic state on the ionic coordinate, the terms $\chi\nabla_l^2\psi$ and $2\nabla_l\chi\nabla_l\psi$ can be neglected. Dividing each term by χ, equation 3.30 is rewritten as :

$$-\frac{\psi}{\chi} \sum_l \frac{\hbar^2}{2M_l} \nabla_l\chi + \{-\sum_i \frac{\hbar^2}{2m}\nabla_i^2 + V\}\psi = E\psi \tag{3.32}$$

We note that the term in the brackets $\{\}$ represent the Hamiltonian of the system if the nuclei are frozen. Let us call this Hamiltonian H_e:

$$H_e = -\sum_i \frac{\hbar^2}{2m}\nabla_i^2 + V(\boldsymbol{r}, \boldsymbol{R}) \tag{3.33}$$

In this expression, the positions of all the nuclei (simply noted $\boldsymbol{R}$) enter H_e as parameters (the positions of all the electrons will now be noted $\boldsymbol{r}$). The eigenvalues of this Hamiltonian are obtained by solving :

$$-\sum_i \frac{\hbar^2}{2m}\nabla_i^2\psi(\boldsymbol{r},\boldsymbol{R}) + V(\boldsymbol{r},\boldsymbol{R})\psi(\boldsymbol{r},\boldsymbol{R}) = \varepsilon(\boldsymbol{R})\psi(\boldsymbol{r},\boldsymbol{R}) \tag{3.34}$$

The energy eigenvalues $\varepsilon(\boldsymbol{R})$ depends parametrically on $\boldsymbol{R}$ and the eigenfunction of H_e are written $\psi(\boldsymbol{r},\boldsymbol{R})$, which indicates that equation 3.34 determines the choice of the function ψ that enters the B-O product of equation 3.29. Using equation 3.34, equation 3.32 is rewritten as follows :

$$-\frac{\psi}{\chi}\sum_l \frac{\hbar^2}{2M_l}\nabla_l^2\chi + \varepsilon(\boldsymbol{R})\psi = E\psi \tag{3.35}$$

or by multiplying by $\frac{\chi}{\psi}$

$$-\sum_l \frac{\hbar^2}{2M_l}\nabla_l^2\chi + \varepsilon(\boldsymbol{R})\chi = E\chi \tag{3.36}$$

This last formulation allows to determine the other function, χ, that enters B-O product. Assuming that B-O approximation is valid (in particular that the terms $\chi\nabla_l^2\psi$ and $2\nabla_l\chi\nabla_l\psi$ can be safely neglected), the solution of the Schrödinger equation for the complete system is reduced to the solution of two equations :

$$-\sum_i \frac{-\hbar^2}{2m}\nabla_i^2\psi_a(\boldsymbol{r},\boldsymbol{R}) + V(\boldsymbol{r},\boldsymbol{R})\psi_a(\boldsymbol{r},\boldsymbol{R}) = \varepsilon_a(\boldsymbol{R})\psi_a(\boldsymbol{r},\boldsymbol{R}) \tag{3.37}$$

$$-\sum_l \frac{\hbar^2}{2M_l}\nabla_l^2\chi_{am}(\boldsymbol{R}) + \varepsilon_a(\boldsymbol{R})\chi_{am}(\boldsymbol{R}) = E_{am}\chi_{am}(\boldsymbol{R}) \tag{3.38}$$

where we have added the correct subscript to the eigenvalues and eigenfunctions (a for the electronic state and m for the lattice state). Finally, the stationary state of the system we were looking for writes :

$$\Psi_n(\boldsymbol{r},\boldsymbol{R}) = \psi_a(\boldsymbol{r},\boldsymbol{R})\chi_{am}(\boldsymbol{R}) \tag{3.39}$$

where ψ_a are eigenfunctions of the "electronic" Hamiltonian :

$$H_e = -\sum_i \frac{\hbar^2}{2m}\nabla_i^2 + V(\boldsymbol{r},\boldsymbol{R}) \tag{3.40}$$

and χ_{am} are eigenfunctions of the "vibrational" Hamiltonian :

$$H_v = -\sum_l \frac{\hbar^2}{2M_l}\nabla_l^2 + \varepsilon_a(\boldsymbol{R}) \tag{3.41}$$

3.2.2 Discussion on the meaning of Born-Oppenheimer approximation

Let us first look closely at equation 3.37 that can be short-written as

$$H_e\psi_a(\boldsymbol{r},\boldsymbol{R}) = \varepsilon_a(\boldsymbol{R})\psi_a(\boldsymbol{r},\boldsymbol{R}) \tag{3.42}$$

The eigenfunctions $\psi_a(\boldsymbol{r},\boldsymbol{R})$ of H_e represent the state of the electrons when the nuclei are at fixed positions $\boldsymbol{R}$: those eigenfunctions and their corresponding energy eigenvalues $\varepsilon_a(\boldsymbol{R})$ depends parametrically on $\boldsymbol{R}$. This indicates that, as the positions $\boldsymbol{R}$ change over time, both $\psi_a(\boldsymbol{r},\boldsymbol{R})$ and $\varepsilon_a(\boldsymbol{R})$ follow this change "adiabatically", while the system stays in electronic state a.

The validity of this B-O approximation comes from the fact that, from a classical point of view, the electrons (way lighter than the nuclei) run through their orbits many times before the nuclei shift their positions by a considerable amount. In other words, the eigenfunctions $\psi_a(\boldsymbol{r},\boldsymbol{R})$ varies slowly with the nuclear coordinates $\boldsymbol{R}_l$. This means that, if the conditions of validity are met, an electron in a given state a moves in a potential $V(\boldsymbol{r},\boldsymbol{R})$ and follow the lattice displacement (change in $\boldsymbol{R}$) without making transitions to other electronic states. We can also look at equation 3.38 :

$$H_v\chi_{am}(\boldsymbol{R}) = E_{am}\chi_{km}(\boldsymbol{R}) \tag{3.43}$$

The eigenfunctions $\chi_{am}(\boldsymbol{R})$ represents the state of the lattice in the potential given by $\varepsilon_a(\boldsymbol{R})$. We see that the energy eigenvalues of equation 3.37 plays the role of the potential energy. Notice also the important fact that $\chi_{am}(\boldsymbol{R})$ depends on a, the electron state.

3.3 Optical center in a static lattice

Let us first focus on the optical features of an optical center incorporated in a static lattice. We are interested in the locations of the energy levels of this optical center. To simplify the problem, only the first anion coordination shell (the ligand ions) is considered in the interaction with the dopant ion (the central ion). Those levels are modified compared the free dopant ion case because of the influence of the ligand ions through the electric field that they produce on the central ion. This static electric field is often called the *crystal field*. We must determine the energy levels of the optical center E_i by solving Schrödinger equation $H\psi_i = E_i\psi_i$ with H the Hamiltonian that accounts for the different interactions and ψ_i are the eigenfunctions of the optical center. One way to do is to use crystal field theory.

3.3.1 Crystal field theory

In crystal field theory, the valence electrons (located at distance r_i from central ion) belong to the central ion and the effect of the lattice is considered through the electrostatic field created by the surrounding ligand ions at the central ion position. The Hamiltonian writes :

$$H = H_{FI} + H_{CF} \tag{3.44}$$

with H_{FI} the Hamiltonian describing the free ion and H_{CF} the crystal field Hamiltonian accounting for the interaction between valence electrons of the central ion (labelled as i) with electrostatic crystal field created by ligand ions (labelled as l) considered as point charges [35] :

$$H_{CF} = \sum_i (-e)\phi(\boldsymbol{r}_i) \tag{3.45}$$

$$\phi(\boldsymbol{r}) = \frac{1}{4\pi\epsilon_0} \sum_l \frac{-Z_l e}{|\boldsymbol{R}_l - \boldsymbol{r}|} \tag{3.46}$$

The free ion Hamiltonian can be decomposed into the sum of a central field Hamiltonian H_0, a coulomb interaction interaction H_{ee} and a spin-orbit interaction H_{so} :

$$H_{FI} = \underbrace{\sum_i \frac{\boldsymbol{P}_i^2}{2m_i} + \frac{Ze^2}{4\pi\epsilon_0 r_i}}_{H_0} + \underbrace{\sum_{i<j} \frac{e^2}{4\pi\epsilon_0 r_{ij}}}_{H_{ee}} + \underbrace{\sum_i \zeta(r_i)\boldsymbol{l}_i.\boldsymbol{s}_i}_{H_{so}} \tag{3.47}$$

From there, depending on the size of the H_{CF} term compared to the three free ion terms, different approaches can be considered to solve the problem by perturbation methods [34] :

Weak crystal field : $H_{CF} << H_{SO}, H_{ee}, H_0$ In this case, energy levels of free ion are slightly perturbed by the crystal field. The free ion wavefunctions are used as basis functions to apply perturbation theory. H_{CF} being the perturbed Hamiltonian. This approach can be used to describe 4f electrons in lanthanides since those electrons are partially screened by the outer $5s^2 5p^6$ electrons, reducing the effect of the crystal field created by ligands ions.

Strong crystal field : $H_{SO} < H_{ee} < H_{CF}$ Here, crystal field term dominates over the H_{ee} and H_{SO}. This method is applied to describe d electrons of metals in some crystal environments.

3.3.2 Lanthanide 4f-5d transition energies

Going trough the lanthanide elements in the periodic table, the $4f$ shell becomes filled with n electrons (n going from 1 to 14). For instance, Ce^{3+} ion has a $[Xe]4f^1$ electron configuration and Eu^{2+} has $[Xe]4f^7$ configuration. This $4f$ shell is considered as an inner shell since it is surrounded by $5p^6$ and $5s^2$ sub-shells of the $[Xe]$ configuration. This means that the crystal field has very little influence on the $4f^n$ states. As a result, the level spacing between those $4f^n$ states is almost completely influenced by the electron-electron interaction within this $4f$ shell.
When an electron is excited from the $4f$ state to the $5d$ empty state, a configuration $[Xe]4f^{n-1}5d$ is obtained. In this case, the $5d$ orbital extends beyond the $[Xe]$ core and it can strongly interact with the ligand anions. In fact, the crystal field interaction with $5d$ electron is about 50 times stronger than with the $4f$ electron [36], which also means that the $5d$-levels energies are highly dependent on the type of compound in which lanthanide ion is placed. For the sake of simplicity, let us take the simplest lanthanide ion to detail the 4f-5d

transition energy : Ce^{3+} that has only one 4f electron (no electron-electron interaction within the 4f shell, which is not the case for Eu^{2+} studied in this master thesis).

4f energy level As mentioned before, 4f energy level of Ce^{3+} in its $[Xe]4f^1$ electronic configuration does not interact strongly with the crystal field. As a result, only a spin-orbit coupling ($^2F_{5/2} - ^2F_{7/2}$) that is already present in the free ion is observed. In the case of Eu^{2+}, the 4f bands split into seven ^7F_J states that spread about 0.6 eV in energy [36].

5d energy level Things are more complicated in the $[Xe]4f^05d^1$ electronic configuration. In that situation, we are in the case of a strong crystal field (but with only one $5d$ electron, H_{ee}=0 for d electron). For the d orbitals (orbital number $l = 2$), five states are possible $(2l + 1)$. In the free ion case, if spin-orbit coupling is ignored, those five d orbitals are degenerate. Let us add the effect of crystal field in two steps.
First, consider that the central ion is surrounded by a spherical electrostatic field caused by anion ligands. Due to the preserved spherical symmetry, the five states are still degenerate but the $5d$ energy can be shifted by the *centroid shift* ε_c defined as the lowering of the energy of the 5d-configuration relative to the value of the free-ion case. This centroid shift is affected by the chemical (covalence) and physical (polarizability) properties of the ligand anions.

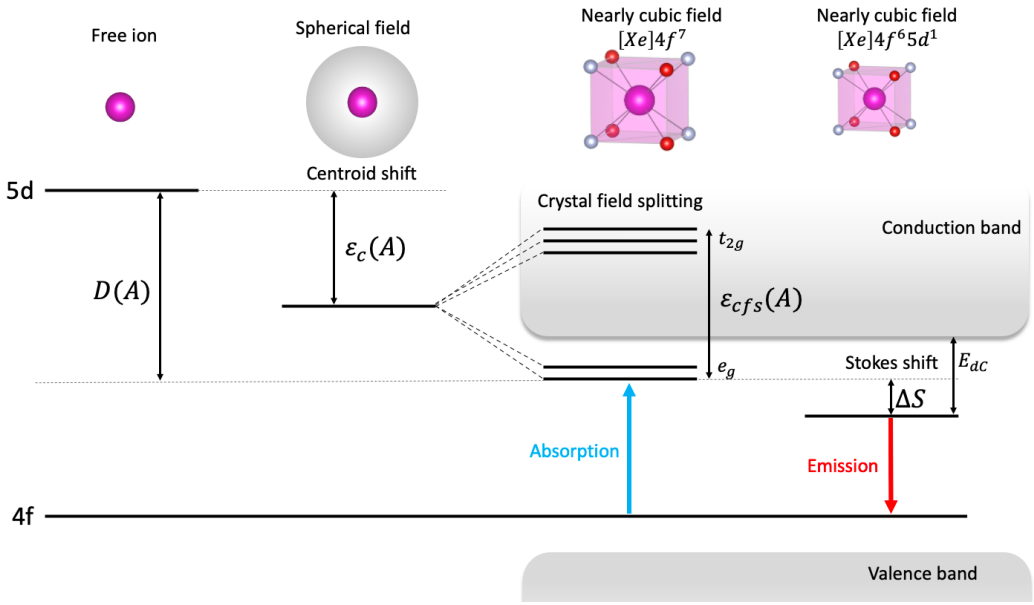

Figure 3.2: Schematic representation of the Dorenbos 's model of the 4f-5d transition energy of Eu^{2+} ion in SALON lattice that has nearly cubic coordination environment composed of oxygen (red) and nitrogen (grey). The $\varepsilon_c(A)$, $\varepsilon_{cfs}(A)$, and $D(A)$ indicate the centroid shift, crystal field splitting and total redshift of Eu^{2+}-5d energy level in compound A (SALON in this work), respectively. The seven 4f energy levels are reduced to one 4f level that is fixed for the representation.

Then, we consider that the ligands anions are coordinated in a given polyhedron shape

(cubic, tetrahedral,...). The five $5d$ orbitals are not equivalent anymore and they are split in energy. This is known as the *crystal field splitting* that is mainly determined by the size and the shape of the first anion coordination polyhedron around Ce^{3+}. For instance, in a cubic coordination environment, the $5d$ energy levels are split into high-energy t_{2g} states (d_{xy}, d_{xz}, d_{yz}) and low-energy e_g states $(d_{x^2-y^2}, d_{z^2})$ (this is the opposite for octahedral symmetry). Those e_g and t_{2g} orbitals can further split if the anion coordination is not perfectly cubic or if two anion types are involved in the anion coordination polyhedron. This crystal field splitting is characterized by the energy difference between the highest $5d_5$ level and the lowest $5d_1$ level noted as ε_{cfs}. In total, when accounting for these two effects, a global redshift (decrease in energy) often denoted as $D(A)$ is observed in the 4f-5d transition energy (where A denotes the compound in which the lanthanide ion is included). Of course, this accounts for absorption energy. To determine the 5d-4f emission energy, we have to add the Stokes shift ΔS which is related to the change in the lowest $5d$ energy due to the atomic relaxation in the excited 5d state (see section on the configuration coordinate model).
Figure 3.2 presents a schematic representation of the model described (often referred to as the Dorenbos's model). Notice that the energy scales as well as the distances scale are not respected. The position of the conduction and valence band in the solid was added in this representation. It allows us to define the quantity E_{dC} which is the energy difference between the bottom of the conduction band and the lowest $5d$ level in the relaxed excited state. This quantity is supposed to play an important role in the temperature quenching process through auto-ionization of the 5d electron in the conduction band due to thermal excitation.

Only a qualitative explanation of this 4f-5d energy difference was given here since this model was not used for this present work. Still, it provides an easy visualisation of what is happening with the 5d levels in the crystal field. For a more quantitative understanding of the phenomena and a deeper physical interpretation, we refer to the thorough work of Dorenbos that analysed during fifteen years divalent and trivalent lanthanides in more than 1000 compounds ([36] for a review of its work). He extracted from these data many tendencies and semi-empirical formulas on the 4f-5d transition energies based on the fitting of ε_{cfs} and ε_c of many compounds as a function of relevant parameters (such as the average distance between the center ion and first coordination shell).

3.4 Radiative processes in a vibrating lattice

The following section is inspired by the book of Di Bartolo et al. [37], which is a compilation of lectures and seminars about the "Luminescence of inorganic solids", held in 1977 at Erice (Italy).

3.4.1 Statement of the problem

Let us focus on the study of luminescence spectra of optically active ions in a solid that is vibrating. We assume here that two conditions are met : First, the concentration of optically active ions is very low such that the interaction between those ions is negligible.

We assume also that electronic energy levels of those ions do not overlap with electronic energy bands of the bulk solid. It is important to note that when dealing with radiative processes of optically active ions in solids, we need to consider that those ions are part of the structure that undergoes vibrational motion. Before going further, it is worth to make some observations on the problem we are interested in :

- "Electronic" energy eigenvalues $\varepsilon_a(\boldsymbol{R})$ plays the role of a potential in which atoms perform vibrational motions. Letter a labels the electronic level.
- These motions can be understood as a superposition of normal modes represented by normal coordinates Q_ν with ν (the label of the mode) going from 1 to 3N (N the number of atoms in the supercell considered).
- A normal mode ν is a vibrational pattern in which all atoms participate in general. It is also possible to observe localized modes that involve a small number of atoms.
- In the following, we will make the harmonic approximation. There is no exchange of energy between normal modes, they are independent. In this approximation, the potential energy $\varepsilon_a(\boldsymbol{R})$ is a sum of independent terms proportional to Q_ν^2, one for each normal mode.
- Each normal mode can be thought as a harmonic oscillator. The vibrations in the solid are thus equivalent to a set of 3N harmonic oscillator. When an oscillator of frequency ω is in its n-th vibrational state, we say that n phonons of energy $\hbar\omega$ are present in the solid.

A big advantage to work with harmonic oscillator is that it is one of the most studied system in quantum mechanics. The key points of such system thought as a set of 3N independent harmonic oscillator is the following : the vibrational state of the lattice $\chi_{a,m}(\boldsymbol{R})$ (that depends on electronic state a!) can be decomposed as a product of harmonic oscillators eigenfunctions $\chi_{a,\nu,n_\nu}(Q_\nu)$, one for each normal mode ν. χ_{a,ν,n_ν} is thus the vibrational eigenfunction of mode ν in the vibrational state n_ν in electronic state a. We write :

$$\chi_{a,m}(\boldsymbol{R}) = \prod_{\nu=1}^{3N} \chi_{a,\nu,n_\nu}(Q_\nu) \tag{3.48}$$

In this approximation, the total vibrational energy is simply the sum of vibrational energy of each mode :

$$E_{vib} = \sum_{\nu=1}^{3N} \hbar\omega_{a,\nu}(n_\nu + \frac{1}{2}) \tag{3.49}$$

n_ν is the number of quanta of vibrational energy (phonons) in mode ν that respects Bose-Einstein statistics. The average number of phonons in mode ν at temperature T writes :

$$< n_\nu >= \frac{1}{\exp\left\{\frac{\hbar\omega_{a,\nu}}{k_B T}\right\} - 1} \tag{3.50}$$

3.4.2 The Franck-Condon principle

We shall now study the interaction of radiation with optically active ion. To do that, we will base our analysis on what is called the "Franck-Condon (F-C) principle". When light is absorbed or emitted, the electronic state changes which induces a change in the lattice structure. In short, Franck-Condon principle assumes that, during an optical transition, the change in the electronic state is much faster than changes in the lattice structure (changes in the internuclear distances for instance) associated to this same transition. From there, three formulations are possible : the classical, the semi-classical and quantum approach. Let us see what those terms means.

Classical formulation

In its classical formulation, F-C principle can be understood as follow : During an electronic transition, electronic state changes so fast that 1) nuclei do not move and 2) nuclei do not change their momenta. Let us detail this with a simple diatomic molecule. Figure 3.3 presents the electronic potential curves (in the harmonic approximation) as a function of the distance R between the two nuclei. The first condition states that R is constant during transitions that are thus represented by vertical lines. The second condition implies that kinetic energy does not change. For instance, if initial state is A', then excited state will be B' with AA'=BB'. Considering a classical harmonic oscillator, the molecule is most of the time located at its turning points, at which the kinetic energy is zero. A third crude condition in the classical formulation is thus to assume that the molecule is found at its turning point when the electronic transition occurs. On figure 3.3, it implies that only AB and CD transitions are allowed. A'B' and C'D' are forbidden.

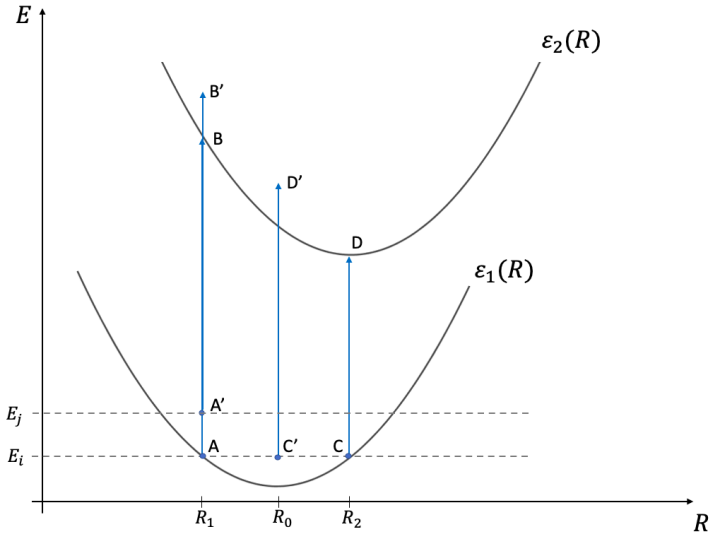

Figure 3.3: Diagram illustrating the classical and semi-classical formulation of the Franck-Condon principle.

Semi-classical formulation

The semi-classical formulation uses the same two first conditions than the classical formulation (constant R, constant momenta). However, the third condition changes. In this formulation, electronic transition can take place for any value of R with a probability $W(R)$ that is given by quantum mechanics. If the system is in its n-th vibrational state, we have :

$$W(R) = |\chi_{a,n}(R)|^2 \tag{3.51}$$

If the system is at thermal equilibrium at temperature T, this generalizes to :

$$W_T(R) = \frac{\sum_n e^{\frac{-E_n}{kT}} |\chi_{a,n}(R)|^2}{\sum_i e^{\frac{-E_n}{kT}}} \tag{3.52}$$

with $E_n = \hbar\omega(n + \frac{1}{2})$. On figure 3.3, it means that all the transitions displayed are allowed (AB, CD, A'B', C'D') but with different probabilities, respectively $|\chi_i(R_1)|^2$, $|\chi_i(R_2)|^2$, $|\chi_j(R_1)|^2$, $|\chi_i(R_0)|^2$. In particular, if the system is in its lowest vibrational state, $W(R)$ is gaussian shaped, the maximum probability will be located at R_0 and transition C'D' will have the greatest importance.
In the case of a system with many degrees of freedom (for instance a periodic solid with normal modes ν), the relevant probability becomes:

$$W_T = \prod_\nu W_{\nu,T}(Q_\nu) \tag{3.53}$$

where $W_{\nu,T}(Q_\nu)$ is of the type in equation 3.52 but with $\omega = \omega_\nu$ and $R = Q_\nu$ (vibrational coordinates).

Quantum formulation

This approach is the one that will be extensively used during the next chapters. This is why the quantum formulation will be seen in more details. Simply put, this formulation states that the transition probability is proportional to the square of the dipole matrix element (as presented for a two two-level atom in section 3.1.2) M_{fi}:

$$M_{fi} = \langle \Psi_f | \boldsymbol{\mu} | \Psi_i \rangle \tag{3.54}$$

with $\Psi_i = \psi_a(\boldsymbol{r}, \boldsymbol{R})\chi_{a,m}(\boldsymbol{R})$ the wavefunction of the system in its initial state expressed as a Born-Oppenheimer product of the electronic wavefunction ψ_a and the lattice wavefunction $\chi_{a,m}$. $\Psi_f = \psi_{a'}(\boldsymbol{r}, \boldsymbol{R})\chi_{a',n}(\boldsymbol{R})$ is the wavefunction of the system in its final state. Staying as general as possible, the electric dipole operator $\boldsymbol{\mu}$ must account for all electrons and nuclei, it can be written as :

$$\boldsymbol{\mu} = \underbrace{-e \sum_i \boldsymbol{r}_i}_{\boldsymbol{\mu}_{el}(\boldsymbol{r})} + \underbrace{e \sum_l Z_l \boldsymbol{R}_l}_{\boldsymbol{\mu}_{nuc}(\boldsymbol{R})} \tag{3.55}$$

In the case of a two-level atom we studied before with only one electron considered, we had simply $\boldsymbol{\mu} = -e\boldsymbol{r}$. Using the fact that the electronic wavefunctions ψ_a vary slowly

with $\boldsymbol{R}$ (they are considered constant and thus go out of the integral on $\boldsymbol{R}$) and their orthonormality, the matrix elements can be rewritten as

$$\begin{aligned}
M_{fi} &= M_{a'n;am} \\
&= \langle \psi_{a'}(\boldsymbol{r},\boldsymbol{R})\chi_{a',n}(\boldsymbol{R})|\boldsymbol{\mu}_{el}(\boldsymbol{r}) + \boldsymbol{\mu}_{nuc}(\boldsymbol{R})|\psi_a(\boldsymbol{r},\boldsymbol{R})\chi_{a,m}(\boldsymbol{R})\rangle \\
&= \langle \chi_{a',n}(\boldsymbol{R})|\underbrace{\langle \psi_{a'}(\boldsymbol{r},\boldsymbol{R})|\boldsymbol{\mu}_{el}(\boldsymbol{r})|\psi_a(\boldsymbol{r},\boldsymbol{R})\rangle}_{\boldsymbol{\mu}_{a'a}(\boldsymbol{R})}|\chi_{a,m}(\boldsymbol{R})\rangle \\
&+ \langle \chi_{a'n}(\boldsymbol{R})|\boldsymbol{\mu}_{nuc}(\boldsymbol{R})|\chi_{am}(\boldsymbol{R})\rangle \underbrace{\langle \psi_{a'}(\boldsymbol{r},\boldsymbol{R})|\psi_a(\boldsymbol{r},\boldsymbol{R})\rangle}_{\delta_{a'a}} \\
&= \langle \chi_{a',n}(\boldsymbol{R})|\boldsymbol{\mu}_{a'a}(\boldsymbol{R})|\chi_{a,m}(\boldsymbol{R})\rangle + \langle \chi_{a'n}(\boldsymbol{R})|\boldsymbol{\mu}_{nuc}(\boldsymbol{R})|\chi_{am}(\boldsymbol{R})\rangle\, \delta_{a'a}
\end{aligned}$$

Some observations can be made at this point : M_{fi} is made of two terms. The second term contributes only when $a' = a$ (i.e. when electronic state does not change in the transition). It gives rise in this case to infrared absorption by the vibrations. The first term contains the dipole moment of the electrons and correspond to transition between different electronic states. If $a' = a$, the first term becomes $\langle \chi_{a,n}|\boldsymbol{\mu}_{aa}(\boldsymbol{R})|\chi_{a,m}\rangle$ with $\boldsymbol{\mu}_{aa}(\boldsymbol{R})$ defined as :

$$\boldsymbol{\mu}_{aa}(\boldsymbol{R}) = \int_V d\boldsymbol{r}|\psi_a(\boldsymbol{r},\boldsymbol{R})|^2\boldsymbol{\mu}_{el}(\boldsymbol{r}) \tag{3.56}$$

Since $\boldsymbol{\mu}_e$ is a odd operator, $\boldsymbol{\mu}_{aa}(\boldsymbol{R})$ is different from 0 only if the system lacks inversion symmetry. If this is the case, the first term also contributes to infrared transition.
For transitions between different electronic states that give rise to radiative processes, the relevant matrix elements are $M_{fi} = \langle \chi_{a',n}|\boldsymbol{\mu}_{a'a}(\boldsymbol{R})|\chi_{a,m}\rangle$. Then if we suppose that $\boldsymbol{\mu}_{a'a}(\boldsymbol{R})$ depends weakly on $\boldsymbol{R}$, we can replace it by $\boldsymbol{\mu}_{a'a}(\boldsymbol{R}_0)$ with $\boldsymbol{R}_0$ the set of nuclear coordinates when the system is at equilibrium. In this approximation, $\boldsymbol{\mu}_{a'a}(\boldsymbol{R}_0)$ can be taken out of the integral :

$$M_{fi} = \boldsymbol{\mu}_{a'a}(\boldsymbol{R}_0)\,\langle \chi_{a',n}|\chi_{a,m}\rangle \tag{3.57}$$

$$|M_{fi}|^2 = |\boldsymbol{\mu}_{a'a}(\boldsymbol{R}_0)|^2|\,\langle \chi_{a',n}|\chi_{a,m}\rangle\,|^2 \tag{3.58}$$

We see that the transition probability is controlled by two factors : $|\boldsymbol{\mu}_{a'a}(\boldsymbol{R}_0)|^2$ (the electronic dipole element) that accounts for the electronic state change. And $|\,\langle \chi_{a',n}|\chi_{a,m}\rangle\,|^2$ which is the square of the overlap integral between vibrational wavefunctions of the initial state and final state. For a given electronic transition (for instance from $5d$ level to $4f$ level in phosphor), this overlap (known as the Franck-Condon overlap) is the key element that controls the strength of a given transition between two vibrational states. It is important to note that $\chi_{a',n}$ and $\chi_{a,m}$ are solutions of different Schrödinger equations (one harmonic oscillator problem and one "displaced" harmonic oscillator problem). Hence, they belong to different sets of orthonormal eigenfunctions and their overlap integral is in principle non-zero even if $m \neq n$. Remember also that $\chi_{a',n}$ and $\chi_{a,m}$ are a product of 3N independent one-dimensional harmonic oscillator (see equation 3.48) :

$$|\,\langle \chi_{a',n}|\chi_{a,m}\rangle\,|^2 = \prod_{\nu=1}^{3N} |\,\langle \chi_{a',\nu,n_\nu}(Q_\nu)|\chi_{a,\nu,m_\nu}(Q_\nu)\rangle\,|^2 \tag{3.59}$$

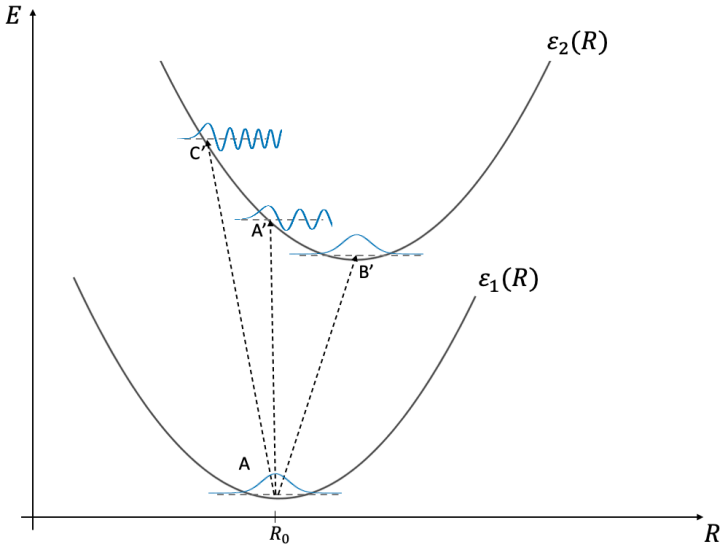

Figure 3.4: Diagram illustrating the quantum formulation of the Franck-Condon principle.

To gain more insight on this quantum formulation, we can come back to our simple diatomic molecule (only one relevant vibration mode) with figure 3.4 where the vibrational wavefunctions of interest are displayed in blue. From this, it is clear that the transition AA' is the one with highest probability (highest overlap). On the other hand, AB' and AC' are very unlikely. In the case of AB' transition, it is clear that there is practically no overlap between vibrational wavefunction of initial state and vibrational wavefunction of final state. In the case of AC' transition, It is the oscillating nature of the wavefunction in final state that leads to a very low overlap.
It is interesting to compare the quantum formulation of FC principle with the classical and semi-classical one. We see that the requirements $R =$ constant and momenta $=$ constant are replaced in the quantum approach by the notion that transitions for which those conditions are not fulfilled are more unlikely that transitions for which it is the case. Notice that the quantum Franck-Condon principle is not a selection rule! Notice also that if the initial and final harmonic oscillators are not displaced with respect to each other but only shifted in energy (i.e. if $\varepsilon_a(\boldsymbol{R}) = \varepsilon_{a'}(\boldsymbol{R}) + C$), then $\chi_{a',n}$ and $\chi_{a,m}$ belong to the same set and thus $\langle \chi_{a',n} | \chi_{a,m} \rangle = \delta_{nm}$.

3.5 One-dimensional configuration coordinate model

The following is a summary of the method employed by Jia et al. in their first-principle study of luminescent properties of numerous phosphors compounds [38], [39]. This method will also be used in the study of luminescent properties of SALON:Eu^{2+}.
Figure 3.5 presents a typical diagram based on the one-dimensional configuration coordinate model (1D CCM). We start by making the assumption that Born-Oppenheimer approximation is valid (electronic variables are decoupled from atomic variables). Then, it is considered that all the complexity of the nuclei displacements can be reduced to one

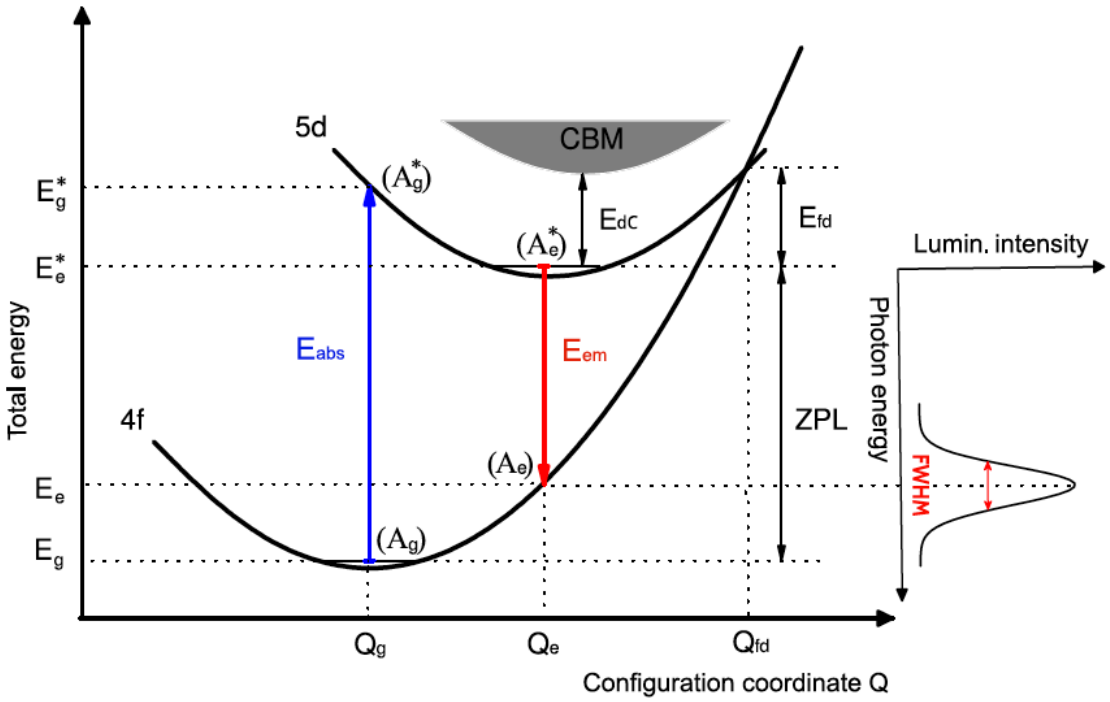

Figure 3.5: Diagram of the one-dimensional configuration coordinate 1D-CCM), image from [38].

effective vibrational mode characterized by a generalised configuration coordinate Q that makes the link between ionic coordinates of the electronic ground state system and those of the excited state system. The potential energy of the system containing a Eu^{2+} ion in the ground state (4f) and in the excited state (5d) are displayed as a function of Q (they are the Born-Oppenheimer potentials ε_a of previous section that will be denoted $V_g(Q)$ for the ground state potential and $V_e(Q)$ for the excited state potential). We can write (by setting minimum of ground state energy curve at the origin and assuming harmonicity) :

$$V_g(Q) = \frac{1}{2}M\Omega_g^2 R^2 = \frac{1}{2}\Omega_g^2 Q^2 \tag{3.60}$$

for the ground state energy curve and

$$V_e(Q) = \frac{1}{2}M\Omega_e^2(R-\Delta R)^2 + E_{ZPL} = \frac{1}{2}\Omega_e^2(Q-\Delta Q)^2 + E_{ZPL} \tag{3.61}$$

for the excited state energy curve. E_{ZPL} stands for the energy difference between excited state curve minima and ground state curve minima. The parameters of the 1D model (effective displacement of the normal coordinate ΔQ, effective displacement of the nuclei ΔR, effective modal mass M and effective vibrational frequencies in the ground/excited state $\Omega_{g,e}$) writes :

$$(\Delta Q)^2 = \sum_{\alpha,i} m_\alpha (R_{\alpha i,e} - R_{\alpha i,g})^2 \tag{3.62}$$

$$(\Delta R)^2 = \sum_{\alpha,i} (R_{\alpha i,e} - R_{\alpha i,g})^2 \tag{3.63}$$

$$M = \frac{(\Delta Q)^2}{(\Delta R)^2} \tag{3.64}$$

where i stands for cartesian directions x,y,z, α labels the atoms, m_α is the atom's mass and $R_{\alpha i,e-g}$ is the atomic i-th coordinate of atom α in the excited-ground state. The modal mass M can be understood as an average of the masses of the atoms involved in the displacement weighted by the square of the nuclei displacements.
The absorption-emission process can be understood thanks to the diagram of figure 3.5, here are the different steps. The starting point is the system in its relaxed 4f ground state (A_g) with energy E_g and coordinate Q_g. When a photon is absorbed by a Eu_{4f} electron, Eu^{2+} ion will be excited to the excited state (A_g^*). System is now out of equilibrium, the coordinate did not change yet but the energy is now E_g^*. Relaxation then takes place due to this new excited state electronic configuration, phonons are emitted during the process. The system reaches a metastable state (A_e^*) with energy E_e^* and coordinate Q_e. Finally photon emission process occurs through 5d-4f deexcitation (A_e: energy E_e, coordinate Q_e). Cycle is completed by a last lattice relaxation with phonon emission until state A_g is reached. From this, we can define classical luminescent properties of the material :
The absorption energy :

$$E_{abs} = E_g^* - E_g \tag{3.65}$$

The Franck-Condon shift in the excited state accompanied by phonon emission :

$$E_{FC,e} = E_g^* - E_e^* \tag{3.66}$$

The emission energy :

$$E_{em} = E_e^* - E_e \tag{3.67}$$

The Franck-Condon shift in the ground state accompanied by phonon emission :

$$E_{FC,g} = E_e - E_g \tag{3.68}$$

The Stokes shift is given by the sum of the two Frank-Condon shifts :

$$\Delta S = (E_g^* - E_g) - (E_e^* - E_e) \tag{3.69}$$

The zero phonon line energy :

$$E_{ZPL} = E_e^* - E_g \tag{3.70}$$

Actually, **the previous equations (from 3.65 to 3.70) are also valid when all the vibrational modes are considered (detailed after) or if the potentials are not harmonics**. It has to be noted that ABINIT is able to provide all the informations that we need (energies E_g, E_g^*, E_e^*, E_e and the atomic positions $R_{\alpha,i}$ in ground and excited state). We can then now use equations 3.60 and 3.61 on these informations to gain insights on other relevant luminescence parameters. For instance, it is possible to calculate the effective vibrational frequencies as

$$\Omega_g^2 = \frac{2E_{FC,g}}{\Delta Q^2} \tag{3.71}$$

$$\Omega_e^2 = \frac{2E_{FC,e}}{\Delta Q^2} \tag{3.72}$$

or the important Huang Rhys factors that indicate the average numbers of phonons emitted during the relaxation process in the ground and excited state:

$$S_{em} = \frac{E_{FC,g}}{\hbar\Omega_g} = \frac{\Omega_g \Delta Q^2}{2\hbar} \tag{3.73}$$

$$S_{abs} = \frac{E_{FC,e}}{\hbar\Omega_e} = \frac{\Omega_e \Delta Q^2}{2\hbar} \tag{3.74}$$

It is also possible to define the difference in curvature between the excited and ground state as :

$$\Delta C = E_{FC,e} - E_{FC,g} \tag{3.75}$$

Finally, let us add a few words on how we can understand thermal quenching with the help of the diagram 3.5. Two mechanisms are often invoked to explain it : the auto-ionization and the $4f$-$5d$ crossover. Auto-ionization refers to the promotion of the $5d$ electron to the conduction band by thermal excitation, the energy barrier of this mechanism is denoted E_{dC} and is equal to the difference between the lowest conduction band energy and the 5d electron energy. The $4f$-$5d$ crossover refers to the jump from $5d$ state to $4f$ state at the crossover between the $4f$ and $5d$ potential energy curve. An electron undergoing this mechanism will thus deexcitate in the $4f$ state only through non-radiative processes. The energy barrier of this mechanism is denoted E_{fd} and is equal to the difference between the cross-over energy and the $5d$ electron energy. Comparing those two energy barriers could indeed allow to determine which mechanism is supposed to be predominant.

3.6 Luminescence intensity formula

3.6.1 1D model at finite temperature

We have shown that the transition probability from an initial electronic state (i) in its vibrational state (m) to a final electronic state (f) in its vibrational state (n) is proportional to

$$W_{i,m-f,n} \propto |\langle \psi_f \chi_{f,n} | \boldsymbol{\mu} | \psi_i \chi_{i,m} \rangle|^2 \tag{3.76}$$

Where $\boldsymbol{\mu}$ is the dipole operator. If we make the Franck-Condon approximation, we have shown that we obtain :

$$W_{i,m-f,n} \propto |\langle \psi_f | \boldsymbol{\mu} | \psi_i \rangle|^2 |\langle \chi_{f,n} | \chi_{i,m} \rangle|^2 = |\boldsymbol{\mu}_{if}|^2 |\langle \chi_{f,n} | \chi_{i,m} \rangle|^2 \tag{3.77}$$

Actually, the transition probability is the same than in the static case but weighted by a factor $|\langle \chi_{f,n} | \chi_{i,m} \rangle|^2$ that takes into account the overlap between vibrational eigenfunctions (the so-called the Franck Condon (FC) factor).
Within the 1D-CCM, the lattice eigenstate is reduced to only one harmonic oscillator function as we only use one effective mode (see figure 3.6). The quantum treatment we have shown in the previous sections leads to the general formulation of emission intensity

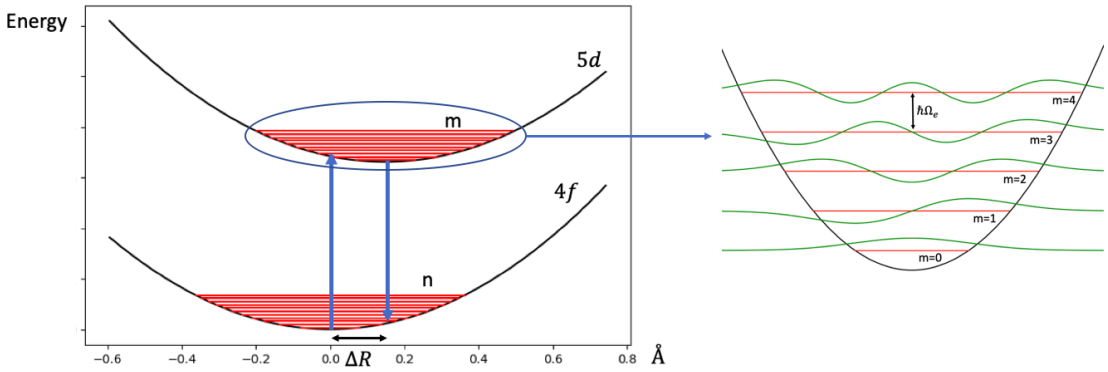

Figure 3.6: Left : Born-Oppenheimer potential energy in ground and excited state as a function of the effective distance from equilibrium. Right : zoom on the excited state potential, vibrational energy levels (in red and separated by $\hbar\Omega_e$) and their corresponding eigenfunctions $\chi_{5d,m}$ (in green) in the harmonic approximation are displayed.

(in number of photons per unit time per unit energy) as a function of the photon energy $\hbar\omega$:

$$I(\hbar\omega) = \frac{n_D\omega^3}{3\epsilon_0\pi c^3\hbar}|\boldsymbol{\mu}_{5d-4f}|^2 A(\hbar\omega) \tag{3.78}$$

where n_D is the refractive index of the material, ϵ_0 is the permittivity and c is the speed of light. $\boldsymbol{\mu}_{5d-4f}$ stands for electronic dipole element of the transition defined as $\boldsymbol{\mu}_{5d-4f} = \langle\psi_{4f}|\boldsymbol{\mu}|\psi_{5d}\rangle$. This quantity is assumed to be constant with ionic coordinates. It is more convenient to use the normalized luminescence intensity defined by [40] :

$$L(\hbar\omega) = C\omega^3 A(\hbar\omega) \tag{3.79}$$

where C is a normalization constant $C^{-1} = \int A(\hbar\omega)\omega^3 d(\hbar\omega)$. Notice again the presence of the ω^3 factor. Finally, we now define the emission spectral function $A(\hbar\omega)$ that describes the shape of the spectrum :

$$A(\hbar\omega) = \sum_{n,m} p_m(T)|\langle\chi_{4f,n}|\chi_{5d,m}\rangle|^2\delta(E_{ZPL} + m\hbar\Omega_e - n\hbar\Omega_g - \hbar\omega) \tag{3.80}$$

where $p_m(T)$ is a thermal occupation factor (i.e. the probability of finding the lattice eigenfunction in state m). By considering the partition function of an harmonic oscillator, it is possible to show that [41] :

$$p_m(T) = a^m(1-a) \tag{3.81}$$

where $a = \exp\left\{-\frac{\hbar\Omega_e}{k_BT}\right\}$.
Let us detail what this equation 3.80 tells us : the spectral emission function is given by an infinite sum of transitions between any initial vibrational state m in electronic $5d$ state (with a probability of occupation that follows Bose-Einstein statistics and hence depends

on temperature, see equation 6.2) to any vibrational state n in the $4f$ electronic state. Each transition $(5d, m \rightarrow 4f, n)$ emits a photon of energy $\hbar\omega = E_{ZPL} + m\hbar\Omega_e - n\hbar\Omega_g$ and its intensity is weighted by the corresponding Franck Condon (FC) factor $|\langle\chi_{4f,n}|\chi_{5d,m}\rangle|^2$. Of course, the delta distribution function should be replaced by a finite width function , Gaussian or Lorentzian function for instance, to describe homogeneous or inhomogeneous broadening of each transition (the width of this function being a free parameter of our model). $\chi_{4f,n}$ are the lattice eigenfunctions of the ground 4f electronic state and $\chi_{5d,m}$ are the lattice eigenfunctions of the excited 5d electronic state (displaced of ΔR compared to the $\chi_{4f,n}$). If the harmonic approximation is made (figure 3.6), they take the form [42] :

$$\chi_{4f,n}(x) = \frac{1}{\sqrt{2^n n!}} \left(\frac{M\Omega_g}{\pi\hbar}\right)^{1/4} \exp\left\{-\frac{M\Omega_g x^2}{2\hbar}\right\} H_n\left(\sqrt{\frac{M\Omega_g}{\hbar}}x\right) \tag{3.82}$$

$$\chi_{5d,m}(x) = \frac{1}{\sqrt{2^m m!}} \left(\frac{M\Omega_e}{\pi\hbar}\right)^{1/4} \exp\left\{-\frac{M\Omega_e(x-\Delta R)^2}{2\hbar}\right\} H_m\left(\sqrt{\frac{M\Omega_e}{\hbar}}(x-\Delta R)\right) \tag{3.83}$$

where H_n and H_m are Hermite polynomials. The challenge here is to evaluate the Franck-Condon factor $|\langle\chi_{4f,n}|\chi_{5d,m}\rangle|^2$ that indicates the relative strength of the (m,n) transition in the total line shape through the overlap between $\chi_{4f,n}$ and $\chi_{5d,m}$.

3.6.2 1D model at T=0K

At T=0K, only the first vibrational state m is populated ($p_0 = 1$ and $p_{m\neq 0} = 0$) and we have thus only to consider the transition from m=0 to any n. The emission spectral function becomes simply :

$$A_{em}(\hbar\omega) = \sum_n |\langle\chi_{4f,n}|\chi_{5d,0}\rangle|^2 \delta(E_{ZPL} - n\hbar\Omega_g - \hbar\omega) \tag{3.84}$$

By applying the same reasoning but by inverting initial and final state , we write for the absorption process (transitions from n=0 to any m):

$$A_{abs}(\hbar\omega) = \sum_m |\langle\chi_{5d,m}|\chi_{4f,0}\rangle|^2 \delta(E_{ZPL} + m\hbar\Omega_g - \hbar\omega) \tag{3.85}$$

Notice however that this is an idealized formula for the absorption spectrum since a better description would require to include also absorption processes from ground state to a continuum of energies in the conduction bands. Integration over the continuum of energies of the conduction bands would thus be necessary but this adds way more difficulties to the problem and this is not addressed in this work.
We can further simplify these expressions if we assume that the two B-O potentials have the same curvature (or equivalently the same effective frequency Ω_{4f}=Ω_{5d}=Ω). In this case, the Huang Rhys factor are the same $S_{em} = S_{abs} = S$ and the F-C factors of emission and absorption can be written in a simple analytical form [43]:

$$|\langle\chi_{4f,n}|\chi_{5d,0}\rangle|^2 = \exp\{-S\}\frac{S^n}{n!} \tag{3.86}$$

$$|\langle \chi_{5d,m} | \chi_{4f,0} \rangle|^2 = \exp\{-S\} \frac{S^m}{m!} \tag{3.87}$$

In fact, even at finite temperature, absorption and emission spectrum are completely symmetric with respect to E_{ZPL} as long as $\Omega_{4f} = \Omega_{5d}$.

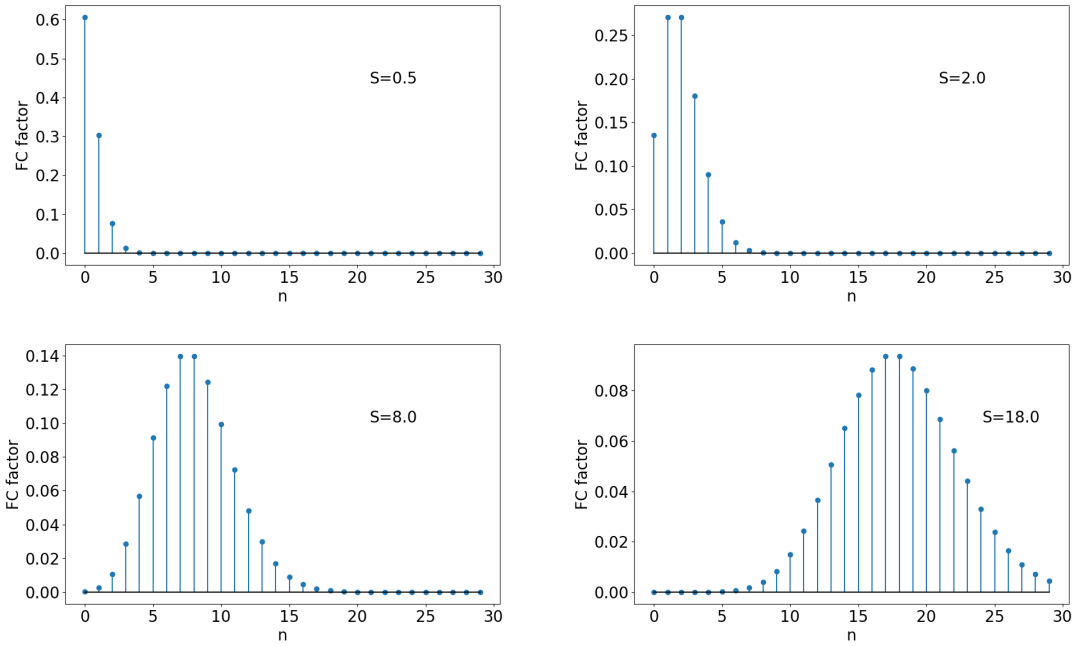

Figure 3.7: FC factors (equation 3.86) in the case of same curvature for different Huang Rhys parameter S

With the help of a Python code, let us observe what the spectral functions look like : Figure 3.7 presents first the F-C factors (equation 3.86) in the case of same B-O curvature for different Huang Rhys parameter S. For a small coupling ($S < 1$), we see that most of emission-absorption process occurs at the zero phonon line (n=0). We see also that the FC factors present an asymmetric shape. As the coupling increases ($S >> 1$), the FC factors becomes progressively gaussian shaped. The maximum is located at the nearest integer to the value $S - 1/2$.
Figure 3.8 presents emission and absorption spectra for different Huang Rhys factors : The first three plots show spectra where the B-O potentials have the same curvature but with a displacement between the two B-O potentials that increases (which induces an increase in S, see equation 3.73). Notice that, as expected, absorption and emission are mirror images around $E_{ZPL} = 2eV$. Also, the zero phonon line fraction in the total spectra (given by e^{-S}) decreases as the coupling increases. Last plot shows the effect of a curvature difference (here $\Omega_g = 1.5 * \Omega_e$). Absorption and emission are no longer symmetric. Notice that in this case, equation 3.86 is not valid!

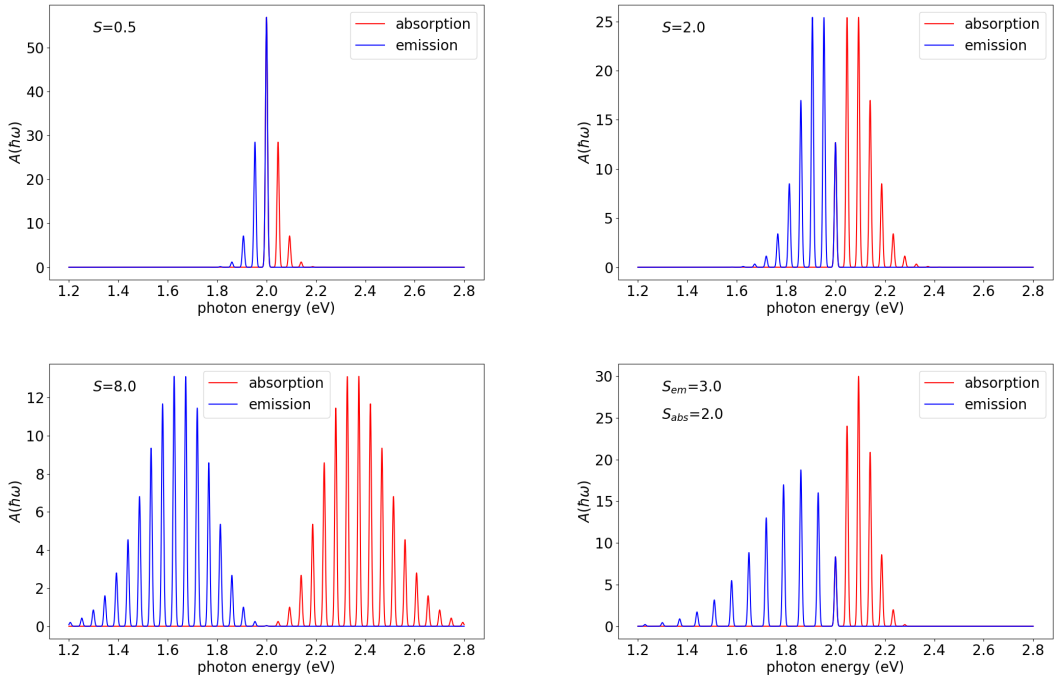

Figure 3.8: Emission and absorption spectra for different Huang Rhys factors with E_{ZPL} fixed to 2 eV. Notice that this zero-phonon line is present both for emission and absorption, the blue and red curves are superimposed at 2 eV.

3.6.3 Full width at half maximum

One important property that we want to compute is the full width at half maximum (FWHM) of the luminescence intensity. An exact way to obtain it is to use the previous equations (equation 3.80 and 3.79) and to compute the FWHM of the envelope of the series of delta peaks that are weighted by their respective FC factors. This cannot be done analytically and requires computer simulation.

It is however possible to derive an analytical expression of the FWHM of the emission spectral function $A(\hbar\omega)$ denoted $W(T)$ as a function of temperature based on a semi-classical formulation of the F-C principle. Let us see how to obtain this formula.

We start by considering the dispersion of the position operator of a quantum harmonic oscillator of mass m and frequency ω in its m'th state: $\sigma^2 = \langle x^2 \rangle - \langle x \rangle^2$. It can be shown ([44]) that $\langle x^2 \rangle = \frac{\hbar}{2m\omega}(2m+1)$. Since the expected value $\langle x \rangle$ is zero for an harmonic oscillator, we are left with a simple expression of the dispersion of the oscillator in its m'th state.

$$\sigma_m = \sqrt{\langle x^2 \rangle} = \sqrt{\frac{\hbar}{2m\omega}(2m+1)} \tag{3.88}$$

FWHM at T=0K We first look at the dispersion at zero temperature (only the state m=0 is occupied). By using the relation $FWHM = 2\sqrt{2\ln 2}\sigma$, it gives for our case :

$$FWHM_{PD}(T=0) = 2\sqrt{\ln 2 \frac{\hbar}{M\Omega_e}} \tag{3.89}$$

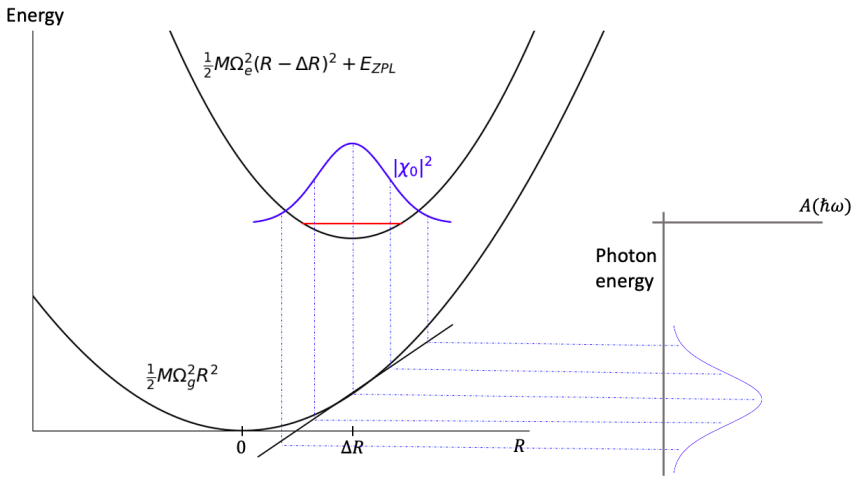

Figure 3.9: Schematic representation of the method to compute the FWHM from following the semi-classical formulation of the Franck-Condon principle.

Actually, this equation is the FWHM of the probability density (PD) associated to the wave function χ_0 (see figure 3.9). The idea is then to assume that the dispersion of the PD can be transformed to a dispersion in emission energy thanks to the classical Franck Condon principle (transitions occur in straight vertical lines from the excited state parabola to the ground state parabola). So we have to do a mapping of the PD in the R coordinates to $A(\hbar\omega)$ that is a function of energy in order to compute the FWHM of the emission spectral function. One simple way to do it is to assume that the curve $V_g = \frac{1}{2}M\Omega_g^2R^2$ is linear around ΔR. As $|\chi_0|^2$ is gaussian shaped, this assumption leads to an emission spectral function $A(\hbar\omega)$ that is also gaussian shaped (see figure 3.9). Thus, It gives for the FWHM of $A(\hbar\omega)$:

$$W(T=0) = 2\sqrt{\ln 2 \frac{\hbar}{M\Omega_e}} \left.\frac{dV_g}{dR}\right|_{\Delta R} = 2\sqrt{\ln 2 \frac{\hbar}{M\Omega_e}} M\Omega_g \Delta R \tag{3.90}$$

One can also re-arrange the terms and use equation 3.74 and 3.73 to obtain $W(0)$ as a function of the Huang Rhys parameters :

$$W(0) = \sqrt{8\ln 2}\frac{S_{em}}{\sqrt{S_{abs}}}\hbar\Omega_g \tag{3.91}$$

FWHM at T≠0K We now have to consider that all initial vibrational states m can be occupied. Using equation 3.88, we first rewrite the dispersion of the harmonic oscillator

being in its state m as $\sigma_m^2 = \sigma_0^2(2m+1)$. We assume then that the final dispersion is given by an average of the σ_m^2 weighted by the corresponding probability of being in state m. We write :

$$Av(\sigma_m^2) = \sum_{m=0}^{\infty} \sigma_0^2(1+2m)p_m(T) = \sigma_0^2 \sum_{m=0}^{\infty}(1+2m)p_m(T) \tag{3.92}$$

The probabilities $p_m(T)$ are the same than in equation 3.80 : $p_m(T) = a^m(1-a)$ with $a = \exp(-\hbar\Omega_e/kT)$. Putting the expression of $p_m(T)$ in equation 3.92, we find :

$$Av(\sigma_m^2) = \sigma_0^2(1-a)\sum_{m=0}^{\infty}(2m+1)a^m \tag{3.93}$$

$$= \sigma_0^2(1-a)\frac{a+1}{(a-1)^2} \tag{3.94}$$

$$= \sigma_0^2\frac{1+a}{1-a} \tag{3.95}$$

Using finally the definition of the hyperbolic cotangent $\coth(x) = \frac{e^{2x}+1}{e^{2x}-1}$ and the new definition effective dispersion $\sqrt{Av(\sigma_m^2)}$, we finally end up with the well established formula ([45], [35]):

$$W(T) = W(0)\sqrt{\coth\left(\frac{\hbar\Omega_e}{2kT}\right)} \tag{3.96}$$

3.6.4 Multi-dimensional configuration coordinate model at T=0K

In the previous sections, we assumed that all the complexity of all the phonons modes could be reduced to one effective phonon mode. We will now look at how we could take into account the effect of all the modes. First, we will simply assume that two modes are involved in the optical transition to get an intuitive understanding of what is happening and we will easily generalize it for the N modes.

Let's imagine a first mode (mode 1 of pulsation ω_1) that presents a small electron-phonon coupling (S_1=0.5) and a second mode (mode 2 of pulsation $\omega_2 > \omega_1$) that has a higher coupling (S_2=4), see figure 3.10. We assume that ω_1 and ω_2 do not change depending on the electronic state so that we have $S_{em,\nu} = S_{abs,\nu} = S_\nu$. Notice that each mode has its own configuration coordinate (Q_1 and Q_2).

Now, in the electronic 4f ground state labelled g (5d excited state will be labelled e), the lattice state is written as a product of harmonic oscillators function χ_{g,ν,n_ν} (lattice wavefunction of the mode number ν in its vibrational state n_ν, in the electronic state g).

$$\chi_{g,(n_1,n_2)} = \chi_{g,1,n_1}\chi_{g,2,n_2} \tag{3.97}$$

At T=0 (all the modes are in their lowest vibrational state in the excited state), the emission spectral function is then written as a double infinite sum (on the all vibrational states n_1 and all vibrational states n_2):

$$A_{em}(\hbar\omega) = \sum_{n_1=0}^{\infty}\sum_{n_2=0}^{\infty} |\left\langle \chi_{g,(n_1,n_2)} \middle| \chi_{e,(0,0)} \right\rangle|^2 \delta(E_{ZPL} - n_1\hbar\omega_1 - n_2\hbar\omega_2 - \hbar\omega) \tag{3.98}$$

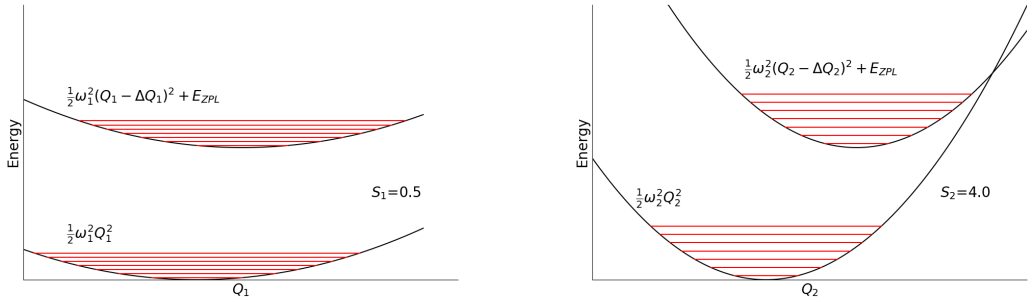

Figure 3.10: 2-dimensional configuration coordinate diagram. Mode 1 (configuration coordinate Q_1, frequency ω_1 and displacement ΔQ_1) is a small-coupling mode while mode 2 (configuration coordinate Q_2, frequency ω_2 and displacement ΔQ_2) is a higher coupling mode.

$\hbar\omega$ stands for photon energy and ω_ν stands for mode ν frequency. As $\chi_{g-e,1,n_1}$ only depends on Q_1 and $\chi_{g-e,2,n_2}$ on Q_2 (as the set of harmonic oscillators are independent), the two dimensional FC overlap integral can be split into a product of two one dimensional FC overlap :

$$\left\langle \chi_{g,(n_1,n_2)} \middle| \chi_{e,(0,0)} \right\rangle = \left\langle \chi_{g,(n_1)} \middle| \chi_{e,(0)} \right\rangle * \left\langle \chi_{g,(n_2)} \middle| \chi_{e,(0)} \right\rangle \tag{3.99}$$

Those 1D FC overlaps are well known at T=0 and for same B-O curvatures (see equation 3.86). This gives :

$$|\left\langle \chi_{g,(n_1,n_2)} \middle| \chi_{e,(0,0)} \right\rangle|^2 = e^{-S_1}\frac{S_1^{n_1}}{n_1!}e^{-S_2}\frac{S_2^{n_2}}{n_2!} \tag{3.100}$$

The emission spectral function of in this 2-dimensional model is thus finally given by :

$$A_{em}(\hbar\omega) = e^{-(S_1+S_2)}\sum_{n_1,n_2}\frac{S_1^{n_1}S_2^{n_2}}{n_1!n_2!}\delta(E_{ZPL}-n_1\hbar\omega_1-n_2\hbar\omega_2-\hbar\omega) \tag{3.101}$$

Let us generalize for the case at 3N dimensions. The letter ν will denote the mode number and run from 1 to 3N where N is the number of atoms in the unit cell. Each mode ν can be in any of its vibrational state n_ν. We write the set of vibrational states in the electronic ground state as $\boldsymbol{n} = (n_1, n_2, ...n_{3N})$ and the set of vibrational states in the electronic excited state as $\boldsymbol{m} = (m_1, m_2, ...m_{3N})$. It gives :

$$A_{em}(\hbar\omega) = e^{-\sum S_\nu}\sum_{\boldsymbol{n}}\left\{\prod_\nu \frac{S_\nu^{n_\nu}}{n_\nu!}\delta\left(E_{ZPL}-(\sum_\nu n_\nu\hbar\omega_\nu)-\hbar\omega\right)\right\} \tag{3.102}$$

The important quantities that enters equation 3.102 are the phonon frequencies ω_ν and what is called the partial Huang Rhys factors S_ν. Let us see how we can obtain these and other important quantities. The approach developed here is mainly based on what was done by Alkauskas et al. in [46] and [2]. We define first the weight by which each mode

ν contributes to the atomic position changes when an optical transition (5d-4f) occurs : $p_\nu = (\Delta Q_\nu / \Delta Q)^2$ where

$$\Delta Q_\nu = \sum_{\alpha,i} m_\alpha^{1/2} (R_{e;\alpha i} - R_{g;\alpha i}) \Delta r_{\nu;\alpha i} \tag{3.103}$$

$$(\Delta Q)^2 = \sum_\nu (\Delta Q_\nu)^2 \tag{3.104}$$

Where $i = (x, y, z)$, α labels the atoms, $R_{e;\alpha i}$ and $R_{g;\alpha i}$ are respectively atomic positions in excited and ground state and $\Delta r_{\nu;\alpha i}$ is the vector that represents the displacement of atom α in phonon mode ν. This vector is normalized such that $\sum_{\alpha,i} \Delta r_{\nu;\alpha i} \Delta r_{l;\alpha i} = \delta_{\nu,l}$. Those equations tell us that the contribution of a mode in the optical transition is given by the dot product between the atomic distortion induced by this optical transition and the phonon eigenvector associated to this mode, weighted by the atom's mass. From this, it is possible to define an effective frequency as :

$$\Omega^2 = \sum_\nu p_\nu \omega_\nu^2 \tag{3.105}$$

where ω_ν is the frequency of the mode ν. Notice that with this definition of the ΔQ_ν, the total ΔQ of equation 3.104 is exactly the same than the one calculated in the 1D model (equation 3.62). This is the same for the effective frequency Ω of equation 3.105 that is equivalent to the effective frequency of the 1D model. We define then the partial Huang Rhys factor associated to mode ν that indicates the number of phonons of mode ν created during the 4f-5d transition.

$$S_\nu = \frac{\omega_\nu \Delta Q_\nu^2}{2\hbar} \tag{3.106}$$

It is then possible to use these S_ν to construct a spectral function of electron-phonon coupling $S(\hbar\omega)$:

$$S(\hbar\omega) = \sum_\nu S_\nu \delta(\hbar\omega - \hbar\omega_\nu) \tag{3.107}$$

3.6.5 Generating function approach

Once $S(\hbar\omega)$ is known, one can use a mathematical tool called the generating function approach to evaluate $A(\hbar\omega)$ as defined in equation 3.102. It can be done by computing the Fourier transform of the generating function $G(t)$: For simplicity, we set $\hbar = 1$ here.

$$A(E_{ZPL} - \omega) = \frac{1}{2\pi} \int_{-\infty}^{+\infty} G(t) e^{i\omega t} dt \tag{3.108}$$

with the generating function $G(t)$ defined as :

$$G(t) = e^{S(t) - S(0)} \tag{3.109}$$

where

$$S(t) = \int_0^{+\infty} S(\omega) e^{-i\omega t} d\omega \tag{3.110}$$

Let us see why this works with our 2D example : We first use the property $\int f(x)\delta(x - x_0)dx = f(x_0)$ to write :

$$S(t) = \int_0^\infty \Big(S_1\delta(\omega - \omega_1) + S_2\delta(\omega - \omega_2)\Big)e^{-i\omega t}d\omega = S_1e^{-i\omega_1 t} + S_2e^{-i\omega_2 t} \tag{3.111}$$

Indeed, this can be generalized as $S(t) = \sum_\nu S_\nu e^{-i\omega_\nu t}$ which is a sum of pulsating wave of amplitude S_ν and pulsation ω_ν. We find also $S(0) = \sum_\nu S_\nu$. We then use the definition of the exponential function : $e^x = \sum_n x^n/n!$ to write :

$$e^{S(t)} = \sum_{n=0}^{\infty} \frac{(S_1e^{-i\omega_1 t} + S_2e^{-i\omega_2 t})^n}{n!} \tag{3.112}$$

$$= 1 + S_1e^{-i\omega_1 t} + S_2e^{-i\omega_2 t} + \frac{1}{2}(S_1^2e^{-i2\omega_1 t} + S_2^2e^{-i2\omega_2 t} + 2S_1S_2e^{-i(\omega_1+\omega_2)t}) + ... \tag{3.113}$$

and

$$e^{-S(0)} = \frac{1}{e^{S(0)}} = \frac{1}{1 + (S_1 + S_2) + \frac{1}{2}(S_1^2 + S_2^2 + 2S_1S_2) + ...} \tag{3.114}$$

which is exactly the zero-phonon line fraction intensity.
The emission spectral function is defined trough the fourier transform of the generating function $G(t)$:

$$A(E_{ZPL} - \omega) = \frac{1}{2\pi}\int_{-\infty}^{\infty} G(t)e^{i\omega t}dt = \frac{e^{-S(0)}}{2\pi}\int_{-\infty}^{+\infty} e^{S(t)}e^{i\omega t}dt \tag{3.115}$$

$$= e^{-(S_1+S_2)}\Big\{\Big(\delta(\omega)\Big) + \Big(S_1\delta(\omega - \omega_1) + S_2\delta(\omega - \omega_2)\Big) \tag{3.116}$$

$$+ \frac{1}{2}\Big(S_1^2\delta(\omega - 2\omega_1) + S_2^2\delta(\omega - 2\omega_2) + 2S_1S_2\delta(\omega - \omega_1 - \omega_2)\Big) + \frac{1}{6}\Big(...\Big) + ...\Big\} \tag{3.117}$$

where we have used the property of the delta function $2\pi\delta(t) = \int_{-\infty}^{+\infty} e^{i\omega t}d\omega$. With this equation, we clearly identify how the spectral function is composed of the zero-phonon process, one-phonon processes, two-phonon processes that mix the modes,... The beauty of this approach is that this formulation is actually exactly equivalent to equation 3.102.

3.6.6 Generalisation at finite temperature

We can further generalize the expression of the emission spectral function at finite T and for different B-O curvatures in the excited or ground state ($\omega_{(e,\nu)} \neq \omega_{(g,\nu)}$).The generalization at finite T can be done by considering that we now have transitions from vibrational states $m_\nu \neq 0$. These transitions are weighted by the usual thermal occupation factors $p_{m_\nu}(T)$ that are different for each mode as the ω_ν are different:

$$p_{m_\nu}(T) = a_\nu^{m_\nu}(1 - a_\nu) \tag{3.118}$$

where $a_\nu = \exp\left\{\frac{\hbar\omega_{(e,\nu)}}{kT}\right\}$. This equation is plotted for different phonon energies on figure 3.11 as a function of temperature. It allows to understand that the way the mode ν contributes to the total spectral function (how important are transitions starting from $m_\nu = 0, m_\nu = 1, m_\nu = 2, ...$) for a given temperature is highly dependent on the frequency of that mode. For instance, at 300K, we see that for mode at 5 meV, the probability for vib. state m=0 for being occupied (0.176) is slightly bigger than the probability for vib. state m=1 for being occupied (0.147) and so on. This contrasts with a mode at 40 meV where the probability for vib. state m=0 for being occupied (0.79) is much bigger than the probability for vib. state m=1 for being occupied (0.17) which indicates that this is much likely to find the mode at 40 meV in its vib. state m=0 which is not true for the mode at 5meV.

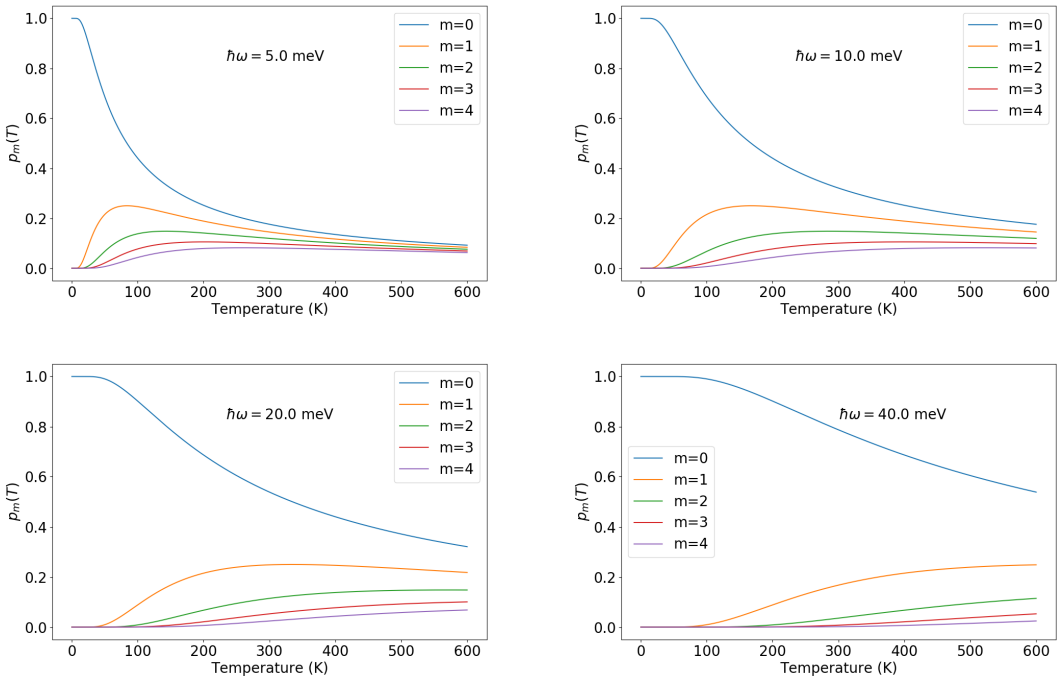

Figure 3.11: $p_{m_\nu}(T) = a_\nu^{m_\nu}(1 - a_\nu)$ for different mode frequency.

The spectral function can be written as :

$$A(\hbar\omega) = \sum_{\boldsymbol{n}}\sum_{\boldsymbol{m}}\prod_{\nu} p_{m_\nu}(T)|\left\langle\chi_{g,\boldsymbol{n}}|\chi_{g,\boldsymbol{m}}\right\rangle|^2\delta(E_{ZPL}+\sum_{\nu} m_\nu\hbar\omega_{e,\nu}-\sum_{\nu} n_\nu\hbar\omega_{g,\nu}-\hbar\omega) \quad (3.119)$$

which is a generalisation of equation 3.80 that considered only one effective mode. Notice that the sum $\sum_{\boldsymbol{n}}$ and $\sum_{\boldsymbol{m}}$ hides 3N infinite sums : $\sum_{\boldsymbol{n}} = \sum_{n_1}\sum_{n_2}...\sum_{n_{3N}}$. As the modes are independent harmonic oscillators, The 3N-dimensional overlap integral can be written as a product of 3N one-dimensional overlap integrals.

$$\left\langle\chi_{g,\boldsymbol{n}}|\chi_{e,\boldsymbol{m}}\right\rangle = \prod_{\nu}\left\langle\chi_{g,n_\nu}|\chi_{e,m_\nu}\right\rangle \quad (3.120)$$

Chapter 4

Preliminary *ab initio* results

Contents

4.1 Bulk SALON

4.1.1 Crystal structure

Experiment Based on single-crystal X-ray diffraction data, Hoerder et al. [1] showed that SALON crystallizes in a tetragonal phase (space group $P4_2/m$) with the unit cell-parameter $a = b$ equals 7.959 Å and c equals 3.184 Å with 2 formula units per cell (figure 4.1). We can mention that the c axis is a binary axis. Combined with inversion, it gives 8 symmetry operations. The structure is a variant of the UCr_4C_4 structure type with strontium on the corresponding uranium site, aluminium and lithium on the corresponding chromium site and nitrogen and oxygen on the corresponding carbide site. Two tetrahedra types form a network hosting the strontium cations in one of the resulting channels (figure 4.2a). The first type (blue tetrahedra T1) is composed of aluminium coordinated with three nitrogen and one oxygen forming a $[AlON_3]^{8-}$ unit. The second type (green tetrahedra T2) is composed of lithium coordinated with one nitrogen and three oxygen forming a $[LiO_3N]^{8-}$ unit. These tetrahedra compose a network of vierer rings (i.e. four polyhedra connected to each other forming a ring) arranged in three types of channels of which two are empty (C1 and C2) and the third hosts strontium cations that are located at a centre of inversion (C3). Strontium atoms are coordinated with four nitrogen (Sr–N distance =

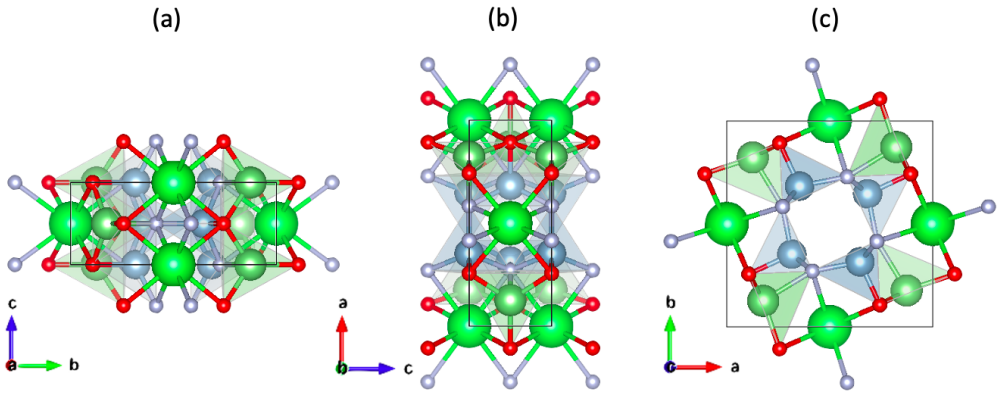

Figure 4.1: Projection of the unit cell of $Sr[Li_2Al_2O_2N_2]$ (a) along a axis, (b) along b axis, (c) along c axis. Flashy green spheres represents strontium atoms, red spheres oxygen atoms, grey spheres nitrogen atoms, green spheres lithium atoms and blue spheres aluminium atoms. Figures were obtained with *VESTA* software.

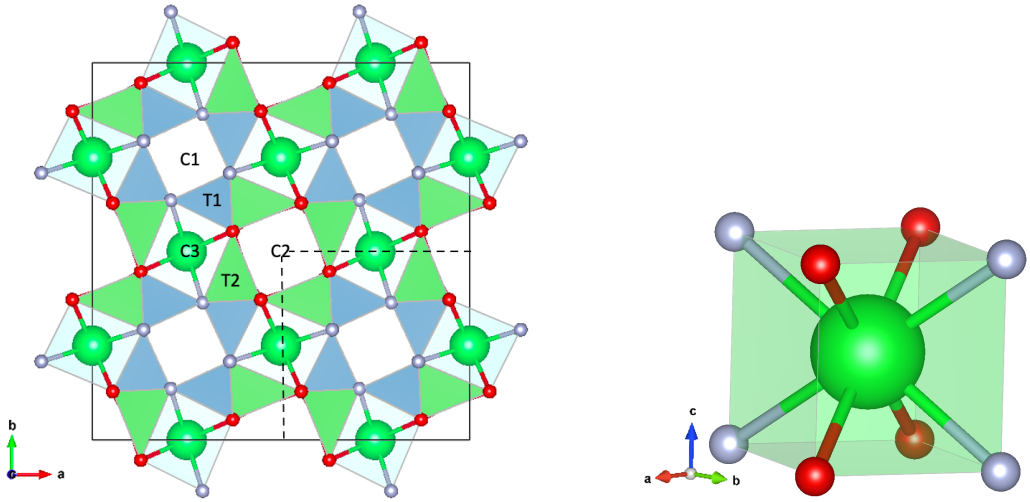

(a) (b)

Figure 4.2: (a) 2x2x2 supercell of bulk SALON. Blue tetrahedra T1 is composed of aluminium coordinated with three nitrogen and one oxygen forming a $[AlON_3]^{8-}$ unit. Green tetrahedra T2 is composed of lithium coordinated with one nitrogen and three oxygen forming a $[LiO_3N]^{8-}$ units. These tetrahedra compose a network of vierer rings arranged in three types of channels of which two are empty (C1 and C2) and the third hosts strontium cations that are located at a centre of inversion (C3). The unit cell is represented with dashed lines. (b) View of the nearly cubic environment of Sr coordinated with four oxygen and four nitrogen.

2.760(5) Å) and four oxygen (Sr–O distance = 2.659(4) Å) which gives a highly symmetrical cube-like coordination (figure 4.2b).

Simulation As for any *ab initio* simulation, convergence studies of the total energy and the unit cell parameters of the material of interest must be realized with respect to some important variables such as the cut-off energy for the plane wave basis (variable *ecut*) or the k-points mesh used to sample the Brilloin zone (variable *ngkpts*). An example of such convergence studies can be found in the appendices. Three cases were studied :

1. Norm conserving pseudopotential (nc), GGA PBE exchange functional.
2. Norm conserving pseudopotential, LDA exchange functional.
3. PAW pseudopotential, GGA PBE exchange functional.

In the case of norm conserving pseudopotential, the choice of $ecut = 40$ Ha and a k-point mesh 2x2x4 leads to a precision of 0.5 mHa per atom compared to the asymptotic value for the total energy and the cell parameters are less than $\approx$ 0,1 % shorter or longer than the asymptotic values.
In the case of PAW pseudopotential, the choice of *ecut*=21 Ha and a 2x2x4 k-points grid leads to the same level of precision.
Table 4.1 shows the comparison between the experimental unit cell parameters and the simulated ones (structural optimization using the Broyden-Fletcher-Goldfarb-Shanno minimization (BFGS)). The algorithm stops when a tolerance force of $5 * 10^{-5}$ Hartree/bohr between atoms is obtained. It can be seen that GGA exchange functional overestimates the lattice parameters of about 0.5-0.7 % in the case (1) and (3) while LDA underestimates the lattice parameters of about 0.9%. We can also mention that, with PAW pseudopotential, the calculated Sr-N and Sr-O bond length are respectively 2.78169Å (+0.78 % compared to experiment) and 2.66670 Å (+0.66 % compared to experiment).

	Exp.	**nc, GGA PBE**	**nc, LDA**	**PAW GGA**
a=b [Å]	7.959	8.005 (+0.58%)	7.886 (-0.92%)	8.014 (+0.69%)
c [Å]	3.184	3.200 (+0.50%)	3.156 (-0.88%)	3.202 (+0.57%)
Vol. [Å^3]	201.692	205.044 (+1.66%)	196.283 (-2.68%)	205.676 (+1.98%)

Table 4.1: Comparison between experimental lattice parameters and simulated ones.

A comparison between the reduced coordinates of the 18 atoms of the unit cell can be found in the appendix A.1.

4.1.2 Electronic structure

Electronic structure was computed with PAW pseudopotential and GGA exchange functional. Brillouin zone path chosen is shown on figure 4.3. Figure 4.4 presents the electronic band structure and the partial density of states obtained with the simulated cell parameters.
According to the these results, bulk SALON has an indirect band gap of 3.44 eV. The experimental band gap determined by Hoerder et al. was 4.4 eV. This underestimation can be explained by the classical "band gap problem" of DFT [48]. The partial density of states provides insightful informations of the nature of the bands. With increasing energy, we can

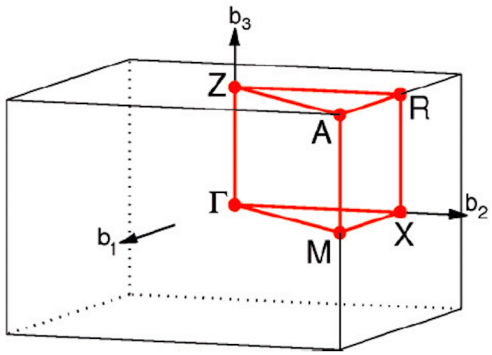

Figure 4.3: Brillouin zone of tetragonal crystal structure. Path chosen for the band structure is $\Gamma - X - M - \Gamma - Z - R - A - Z - X - R - M - A$ as advised in [47].

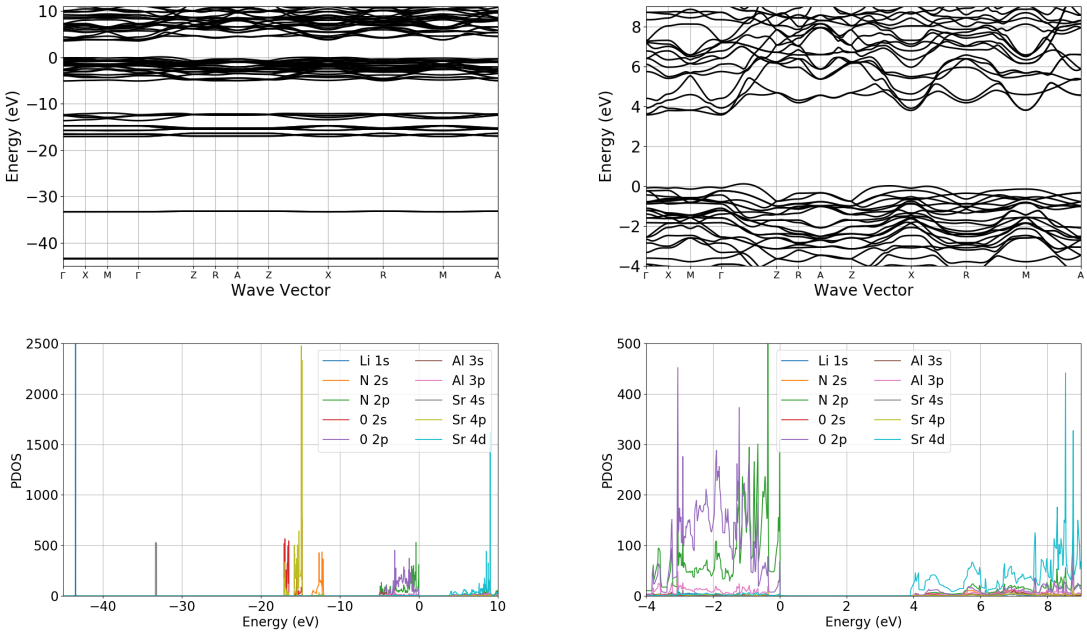

Figure 4.4: Top left : complete electronic band structure of bulk SALON. Top right : zoom near Fermi level (set to 0). An indirect band gap of 3.44 eV is calculated. Bottom left : complete partial density of states decomposed in the different orbitals. Bottom right : zoom near the Fermi level.

observe the following states : deep and localized 1s states of lithium and 4s of strontium. Then three characteristic bands composed of 2s states of oxygen, 4p states of strontium and 2s states of Nitrogen. Near the Fermi level, we have a big stack composed of 2p states of oxygen and nitrogen with 3p states of aluminium. Finally, the bottom of the conduction bands is mainly composed of 4d states of strontium. It was also verified that using the experimental cell parameters does not change noticeably the electronic properties.

4.1.3 DFPT calculations

Calculations based on density functional perturbation theory [49] were performed in order to obtain the phonon frequencies at Γ, the Born effective charge tensors, the electronic dielectric tensor, the complete phonon band structure and the thermal expansion coefficient.

Phonon band structure

First, convergence studies with respect to the plane wave cut-off *ecut* and the *k*-point grid were done on the phonon energies at Γ point. It was obtained that a cut off energy *ecut* = 30 Ha and a k-point mesh 2x2x4 leads to a precision of 10^{-3} meV compared to the converged value. Then, the entire phonon band structure was calculated. The result is presented on figure 4.5. A partial density of state analysis is also presented where we observe clearly the different particular localized modes present in the phonon band structure. The phonon frequencies at Γ point and a detailed analysis of their irreducible representation are provided in appendix B.

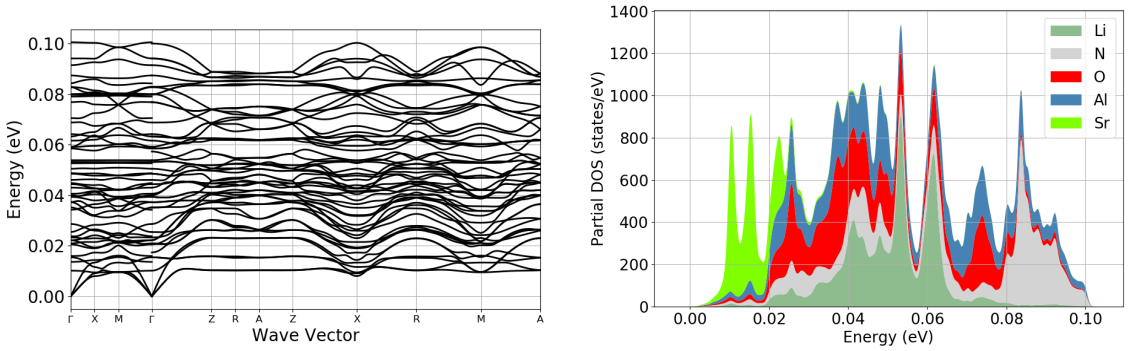

Figure 4.5: Left : Phonon band structure of bulk SALON. Right: Phonon partial density of states of bulk SALON.

Born effective charge

For each atom of the unit cell, the Born effective charge defined as $Z^*_{ij} = \frac{\Omega}{e}\frac{\delta P_i}{\delta d_j}$ (Ω the unit cell volume, e the electron charge, P_i the polarization along axis i and d_j the displacement along axis j) was computed with a 4x4x8 k-point grid and *ecut*=40 Ha. The born effective charge tensors are presented on table 4.2. We can see some slight anisotropy in the X-Y plane. Notice also that, due to symmetry, x component is inverted with y component between atoms 1-2 and atoms 3-4. Compared to their respective ions (Li^+, N^{3-}, O^{2-}, Al^{3+}, Sr^{2+}), we can note that globally, nitrogen atoms are less negatively charged, oxygen is more negatively charged along x (or y) direction, aluminium atoms are strongly less positively charged and strontium atoms are less charged along x (or y) direction and z direction.

Li1 and Li2	**Li3 and Li4**	**N1 and N2**
$\begin{pmatrix} 1.20 & 0.02 & 0 \\ 0.04 & 0.99 & 0 \\ 0 & 0 & 0.89 \end{pmatrix}$	$\begin{pmatrix} 0.99 & -0.04 & 0 \\ -0.02 & 1.20 & 0 \\ 0 & 0 & 0.89 \end{pmatrix}$	$\begin{pmatrix} -2.35 & 0.11 & 0 \\ 0.16 & -2.27 & 0 \\ 0 & 0 & -2.88 \end{pmatrix}$
N3 and N4	**O1 and O2**	**O3 and O4**
$\begin{pmatrix} -2.27 & -0.16 & 0 \\ -0.11 & -2.35 & 0 \\ 0 & 0 & -2.88 \end{pmatrix}$	$\begin{pmatrix} -1.89 & 0.06 & 0 \\ 0.04 & -2.57 & 0 \\ 0 & 0 & -1.88 \end{pmatrix}$	$\begin{pmatrix} -2.57 & -0.04 & 0 \\ -0.06 & -1.89 & 0 \\ 0 & 0 & -1.88 \end{pmatrix}$
Al1 and Al2	**Al3 and Al4**	**Sr1**
$\begin{pmatrix} 1.99 & 0.11 & 0 \\ 0.04 & 2.33 & 0 \\ 0 & 0 & 2.58 \end{pmatrix}$	$\begin{pmatrix} 2.33 & -0.04 & 0 \\ -0.11 & 1.99 & 0 \\ 0 & 0 & 2.58 \end{pmatrix}$	$\begin{pmatrix} 2.04 & 0.11 & 0 \\ 0.16 & 3.11 & 0 \\ 0 & 0 & 2.58 \end{pmatrix}$
Sr2		
$\begin{pmatrix} 3.11 & -0.16 & 0 \\ -0.11 & 2.04 & 0 \\ 0 & 0 & 2.58 \end{pmatrix}$		

Table 4.2: Born effective charge tensor of each atom

Dielectric tensor

Convergence studies on the dielectric tensor showed that, as for the Born effective charges, a high resolution of the k-point grid was necessary to obtain converged values. This can be explained by the fact that DFPT performs the gradient of the wave-function in the reciprocal k-space. A good approximation of this gradient requires a high "resolution" of the k-points grid and therefore a large number of k-points. For $ecut = 40$ Ha and a 4x4x8 k-point grid, we obtain the following converged electronic dielectric tensor : $\begin{pmatrix} 3.954 & 0 & 0 \\ 0 & 3.954 & 0 \\ 0 & 0 & 4.0229 \end{pmatrix}$

Thermal expansion coefficient

When we will examine the effect of temperature on the luminescent properties of SALON:Eu, one of the effect to consider is the thermal expansion of the lattice. To do that, it is indeed first necessary to compute the expansion coefficient of bulk SALON.

Method Our first hypothesis is that we consider SALON as isotropic, meaning that α is reduced to a scalar volumetric coefficient. We write :

$$\alpha_V = \frac{1}{V}\left(\frac{\partial V}{\partial T}\right) \tag{4.1}$$

The second hypothesis is that the quasiharmonic approximation (QHA) can be used where we assume that each phonon acts as an independent harmonic oscillator (phonon-phonon coupling is ignored). The only contribution to the thermal expansion of the crystal is due

to the coupling between the phonons and the change in the unit cell volume [50]. The approach is based on the minimization of the Helmholtz free energy [51], [52]:

$$F(V,T) = E(V) + F_{vib}(V,T) \tag{4.2}$$

with

$$F_{vib}(V,T) = \sum_{\boldsymbol{q}\nu} \left(\frac{\hbar\omega_{\boldsymbol{q}\nu}(V)}{2} + kT \ln\left(1 - e^{-\frac{\hbar\omega_{\boldsymbol{q}\nu}(V)}{kT}}\right)\right) \tag{4.3}$$

where $E(V)$ is the the static energy versus volume curve obtained after a full relaxation (at zero temperature) and $F_{vib}(V,T)$ is the vibration energy. The first term is the zero-point motion energy and the second term is the thermal excitation energy. $\hbar\omega_{\boldsymbol{q}\nu}(V)$ refers to the phonon energy at wave vector $\boldsymbol{q}$ and phonon band index ν. If $F(V,T)$ is known, the idea is then to pick a temperature T_i and to minimize $F(V,T_i)$ with respect to V, it gives a point (V_i,T_i). By repeating the operation for different temperatures, we obtain a temperature-volume curve that minimize $F(V,T)$. Finally, the thermal expansion coefficient is obtained with equation 4.1.

Result After a full relaxation of bulk SALON that gave a relaxed volume V_0, 9 fixed volumes were chosen (from $0.98V_0$ to $1.02V_0$ by step of $0.005V_0$) to perform relaxation for each volume. From that, we obtain the static volume-energy curve shown on figure 4.6a (The units chosen are the same than the ones found in [51], mol-c is the abbreviation of a mole-cell, that is, the number of Avogadro times the atoms in a unit cell). Then, phonon dispersion curves were calculated for each volume. For each volume, F_{vib} was computed in ANADDB for 30 temperatures (from 30K to 900K by step of 30K, see figure 4.6b). The total $F(V,T)$ is shown on figure 4.6c at only 7 temperatures for clarity. We see that as temperature increases, the volume that corresponds to the minimum free energy increases. The temperature-volume curve is computed and shown on figure 4.6d. Finally, $\alpha_V(T)$ is shown on figure 4.6e.
We observe that within the range of operating LED temperature (300K-500K), α_V of SALON varies from $3\cdot10^{-6}(\frac{1}{K})$ to $3.5\cdot10^{-6}(\frac{1}{K})$. There is no experimental value of thermal expansion coefficient of SALON to compare with our first-principle calculation. It is however possible to compare it with similar ceramic compounds : Aluminium nitride (AlN), Sialon ($Si_3N_4Al_2O_3$), Silicon nitride (Si_3N_4) have respectively thermal expansion coefficients of $5.3\cdot10^{-6}(\frac{1}{K})$, $3.3\cdot10^{-6}(\frac{1}{K})$ and $3.0\cdot10^{-6}(\frac{1}{K})$ at ambient temperature ([53]).
It is also possible to analyse the effect of zero-point motion : For a unit-cell composed of 54 atoms, it is found that the unit-cell volume calculated in classical DFT is 4163.3636 bohr^3 while the one calculated with the contribution of zero point energy is 4169.4230 bohr^3 (increase of 0.145%).

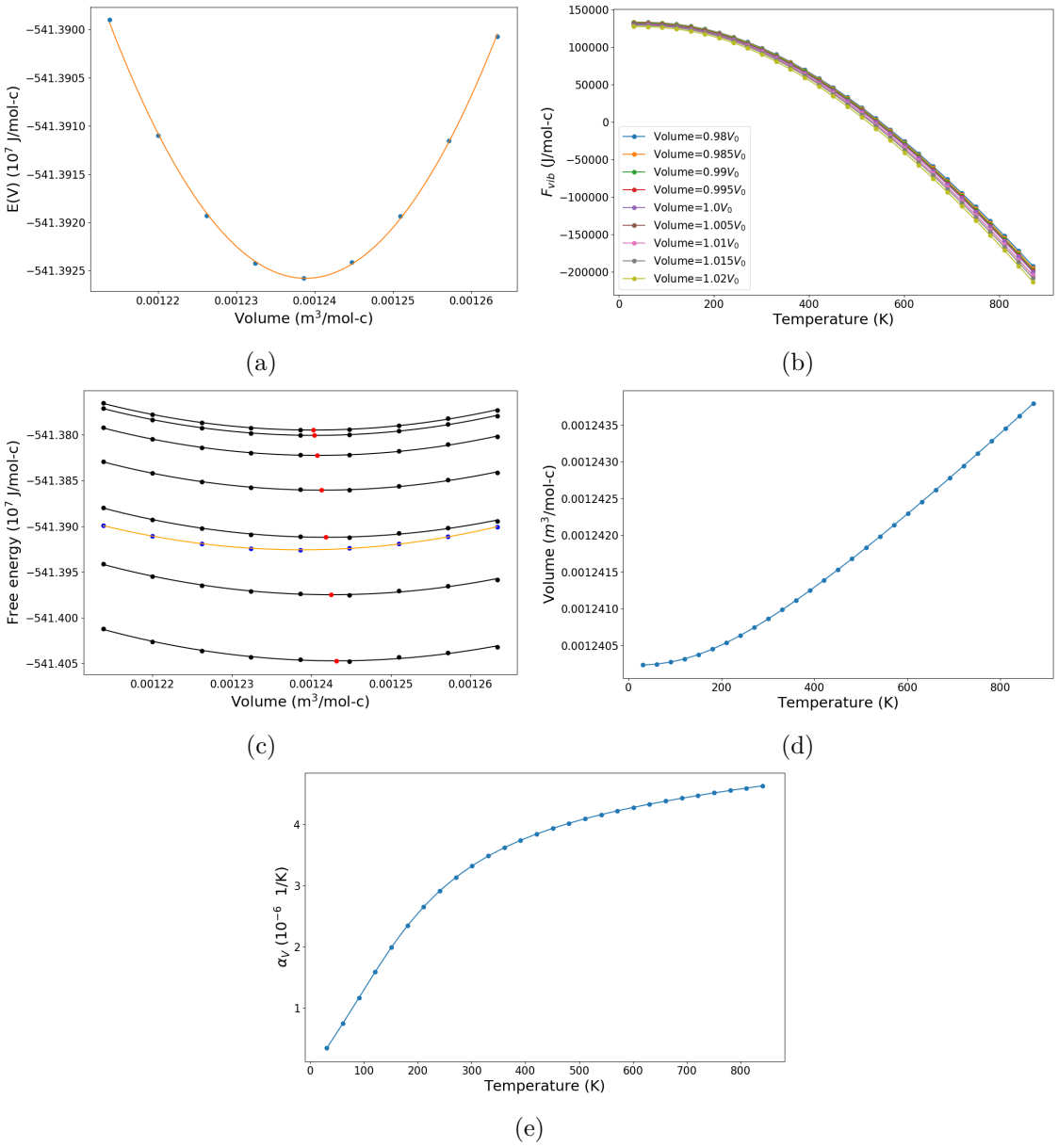

Figure 4.6: Free energy approach to calculate the thermal expansion coefficient : (a) Static internal energy $E(V)$ calculated for 9 volumes (blue dots) interpolated with a second-order polynomial fit (orange). (b) Vibrational free energy $F_{vib}(T)$ for the 9 volumes (c) Total free energy $F(V,T) = E(V) + F_{vib}(V,T)$ at 7 temperatures from 30K (upper black curve) to 870K (lower black curve) by step of 120K. The calculated black points are interpolated by a second-order polynomial fit (black curves). Red dots show the minimum of each curve. Contribution of $E(V)$ is added on the plot (same color than figure (a)). (d) Temperature-Volume (based on the red points of figure (c)) points linearly interpolated. (e) Expansion coefficient based on equation 4.1.

4.2 Europium doped SALON

In this section, we aim principally to present the method used to deal with the europium doping and especially with the Eu_{5d} excited state. Only the results of the structural relaxation in the ground state are shown in this section as the electronic properties and the crystal structure modification due to 4f-5d transition are directly linked to the luminescent properties treated in depth in the next section.
To mimic the effect of europium doping, one of the strontium atom must be replaced manually by europium atom. Indeed, the unit-cell used should be enlarged so that the interaction between europium atoms becomes negligible. However, increasing the supercell size is computationally demanding. There is a compromise here on the supercell size choice that was finally fixed to a 1x1x3 supercell (the motivations of this choice are addressed in subsection 4.2.3).

4.2.1 Eu_{4f} ground state calculations

PAW pseudopotential and GGA PBE exchange functional were used to conduct structural relaxation on a 1x1x3 supercell (54 atoms) where one of the six equivalent strontium atom is replaced by one europium atom (doping rate of 16.67 %). Following the methodology of Jia et al in [38], a Hubbard term U ([54], [55]) was added on the $4f$ states of europium ions so that those levels are present in the band gap (U=7 eV and J=0.7 eV). $Eu^{2+} = [Xe]4f^7$ has a spectroscopic term $^8S_{7/2}$(L=0, S=7/2). From an atomistic point of view, no spin-orbit coupling is thus expected in the ground state (L.S=0). In the solid, we can thus expect a small multiplet splitting compared to the excited case ($[Xe]4f^6 5d^1$). The plane wave cut off was set to 35 Ha and a 2x2x2 k-point grid was used. Table 4.3 summarizes the results of the structural relaxation and compares the undoped case with the doped case : we see first that doping induces small distortions in the lattice (the structure is no longer tetragonal but slightly monoclinic). We also observe that doping induces a increase in the volume of the unit cell. Finally, the Eu-N (2.78335 Å) and Eu-O (2.67863 Å) bond length are very close to the Sr-N (2.78169 Å) and Sr-O (2.66670Å) bond length which is reasonable since the experimental atomic radii of Eu and Sr in their VIII coordination state are very close (1.39 and 1.40 Å respectively [56].).

	Cell 54 atoms undoped	**Cell 54 atoms doped**	**Difference**
a [Å]	8.012646	8.01382	0.001174
b [Å]	8.012646	8.01487	0.002224
c [Å]	9.609391	9.6116	0.002209
α [°]	90	90	0
β [°]	90	90	0
γ [°]	90	90.0418	0.0418
Vol. [Å^3]	616.946796	617.350703	0.403907

Table 4.3: Results of the ground-state relaxation of the a supercell composed of 54 atoms (1x1x3 supercell) for the bulk undoped SALON and for the europium doped case (one Strontium atom is replaced).

4.2.2 Eu_{5d} excited state calculations

To mimic the 4f-5d transition, Δ SCF method is used : promotion of highest Eu_{4f} electron to the lowest Eu_{5d} level is accomplished by changing manually the occupation number of Eu_{4f} and Eu_{5d} bands. To be explicit, if the occupation numbers in the ground state are (...1 1 1 1 0 0 0 0...), the occupation numbers in the excited state are set to (...1 1 1 0 1 0 0 0 ...). In this method, the Eu_{4f} hole is treated explicitly in the valence manifold through forced occupation numbers. This approach has been successfully applied to study the luminescence in Ce-doped ([57],[58]), and Eu-doped inorganic scintillators ([59]). It was shown that the Coulomb interaction is correctly included between the Eu core and the explicitly treated Eu_{5d} electron [60].
By doing that, the Eu_{4f} bands split into one unoccupied band that stays in the gap, and six occupied bands that are shifted downward. Moreover, the Eu_{5d} state is shifted downward in the band gap. This can be explained by considering the hole left by the 4f-5d transition that creates an attractive coulomb potential for the Eu_{5d} electron. The Eu_{5d} electron and the Eu_{4f} hole are thus bound to each other (exciton).
Schematic electron occupancies for the ground state excited state of typical Eu^{2+} are presented on figure 4.7. We note that excited europium ion $(Eu^{2+})^* = [Xe]4f^6 5d^1$ has now a spectroscopic term (for $4f^6$ term) ^7F_J with J=0-6. Splitting is thus expected in the spectrum. However, only the lowest energy excited state is studied in this work. Spin-orbit coupling was not included in the simulations. After the absorption, the environment will be impacted by the excited electron. If we suppose that the electron is re-emitted quickly after the absorption, it will only affect the local geometry of the crystal and not the macroscopic state of the crystal, meaning that the lattice parameters of the crystal will not change a lot ([60]). Thus, relaxation in the excited state is done at fixed lattice parameters of the ground state.

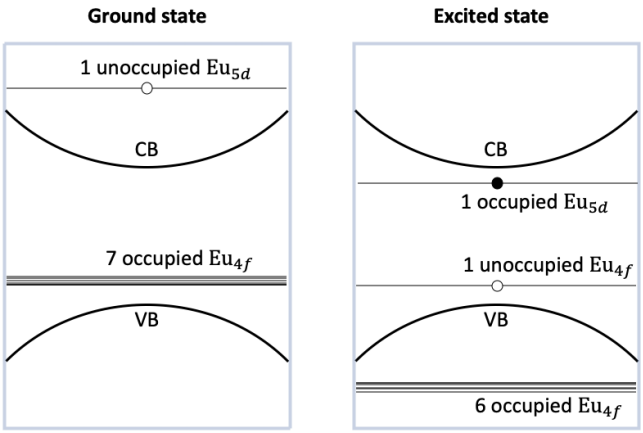

Figure 4.7: Schematic electron occupancies for the ground and excited state calculations of Eu^{2+}doped phosphors. CB and VB stand respectively for conduction band and valence band.

4.2.3 Choice of the supercell size

Numerous simulations were first conducted on a 1x1x2 supercell size of 36 atoms. It was observed that while the ground state did not cause any problem, the Eu_{5d} state was more problematic : the 5d energy was not stable at all and was jumping between numerous values. The explanation (detailed hereafter) came from a careful analysis of the Eu_{5d} electronic structure.

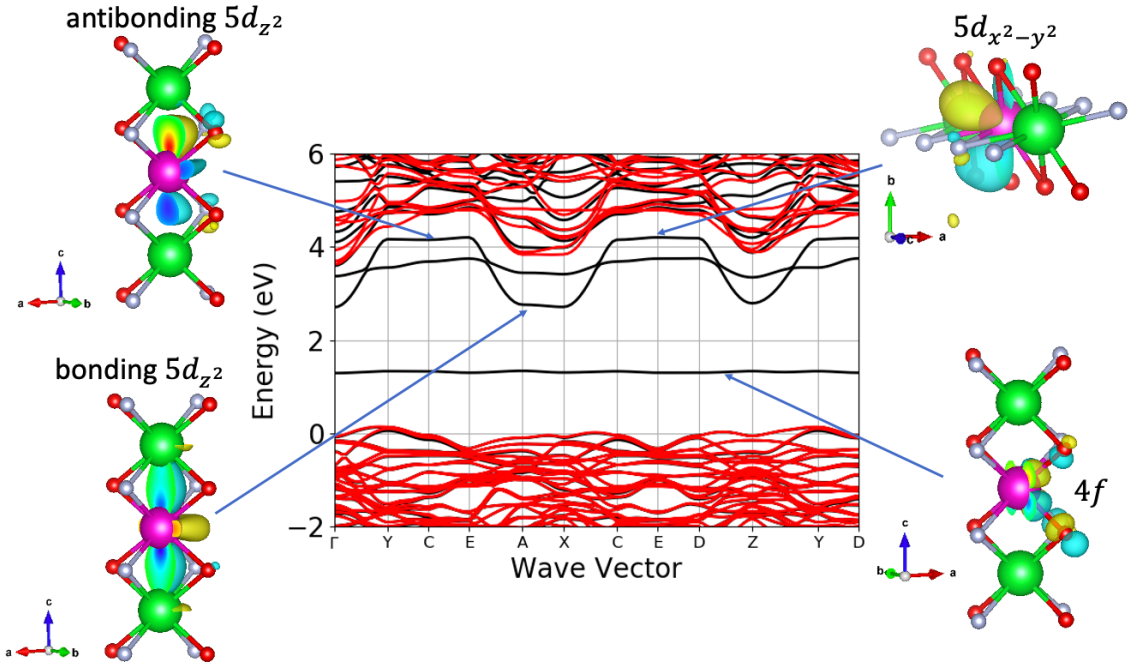

Figure 4.8: 1x1x2 supercell : band structure in the excited state (with a brillouin zone path of monoclinic structure) and the orbitals of interest (real part of the wave function). The crossing between 5d states is the source of instabilities in the SALON:Eu excited state. Increasing the supercell size (and thus reducing the unphysical interaction between europium atoms) solved the problem.

Figure 4.8 shows the band structure of a 1x1x2 supercell with europium atom in its Eu_{5d} excited state. The orbitals of interest are shown to allow a better understanding of the behaviour of this band structure. First, the only 4f unoccupied state staying in the band gap is correctly localized. Then we can look at the occupied 5d orbitals. A nearly localized $5d_{x^2-y^2}$ state is observed, it is interesting to note how the lobes are placed between oxygen and nitrogen atoms. Concerning the $5d_{z^2}$ state that presents huge dispersion, we can observe first a bonding character when the z component of the wave vector is 0. Of course, those bonds come from the fact that europium atoms are too closed (one above the upper strontium and one below the lower strontium). On the contrary, for a z component of the wave vector different of 0, we observe the associated anti-bonding character. This huge dispersion implies the observed crossing between the 5d levels, which explains the instability. It was thus expected that this undesired and unphysical dispersion of the $5d_{z^2}$ state would decrease as the distance between europium along c-axis is increased.

This hypothesis was confirmed by increasing the supercell size and thus reducing the interaction between europium atoms. Three other supercell sizes were tested (1x1x3 with 54 atoms, 1x1x4 with 72 atoms and $\sqrt{2}$x$\sqrt{2}$x3 with 108 atoms) and their respective electronic structures were analysed. For each case, the dispersion of $5d_{z^2}$ state was sufficiently lowered so that no crossing appeared and the lowest excited state was the $5d_{z^2}$ (see electronic structures of section 5.1.1). Moreover, no noticeable change in the electronic structure was observed between the three cases, except a slightly smaller dispersion of $5d_{z^2}$ state with 1x1x4 supercell compared to the two other cases. Therefore, to save computational time, the use of a 1x1x3 supercell of 54 atoms was chosen to study the luminescent properties.

Chapter 5

Luminescent properties results at T=0K

Contents

5.1 4f-5d transition

5.1.1 Electronic structure

Figure 5.1 shows the band structures of the four characteristic states of the one dimensional coordinate model as described in section 3.5. As expected, increasing the supercell size leads to cleaner band structures. We see that the dispersion of the $5d_{z^2}$ band is reduced. Indeed, as the distance between europium along the c-axis is increased, the bonding/anti-bonding character is reduced. Moreover, we dot not observe anymore a crossing between $5d_{z^2}$ and $5d_{x^2-y^2}$ bands. Figure 5.2 shows the orbitals associated to the three bands lying in the band gap of A_e^* state (relaxed structure in excited state): Occupied $5d_{z^2}$ that presents still a small bonding character along c-axis (which gives this dispersion from Γ to Z point in the band structure), unoccupied $5d_{x^2-y^2}$ band and unoccupied $4f$ band.
One interesting quantity to extract from these band structures is the energy difference E_{dC} between $5d_{z^2}$ and conduction band minimum located at Γ. As the $5d_{z^2}$ energy varies with the wave-vector because of an unphysical europium-europium interaction, the $5d_{z^2}$ energy was estimated to be at the middle of the $5d_{z^2}$ maximum and minimum. For A_g^* state,

$E_{dC} = 0.52eV$ and for A_e^* state, $E_{dC} = 0.445eV$. This last value is supposed to be the energy barrier for auto-ionization process that aims to explain thermal quenching. This value of E_{dC} should then be compared with the energy barrier for $4f$-$5d$ crossover.

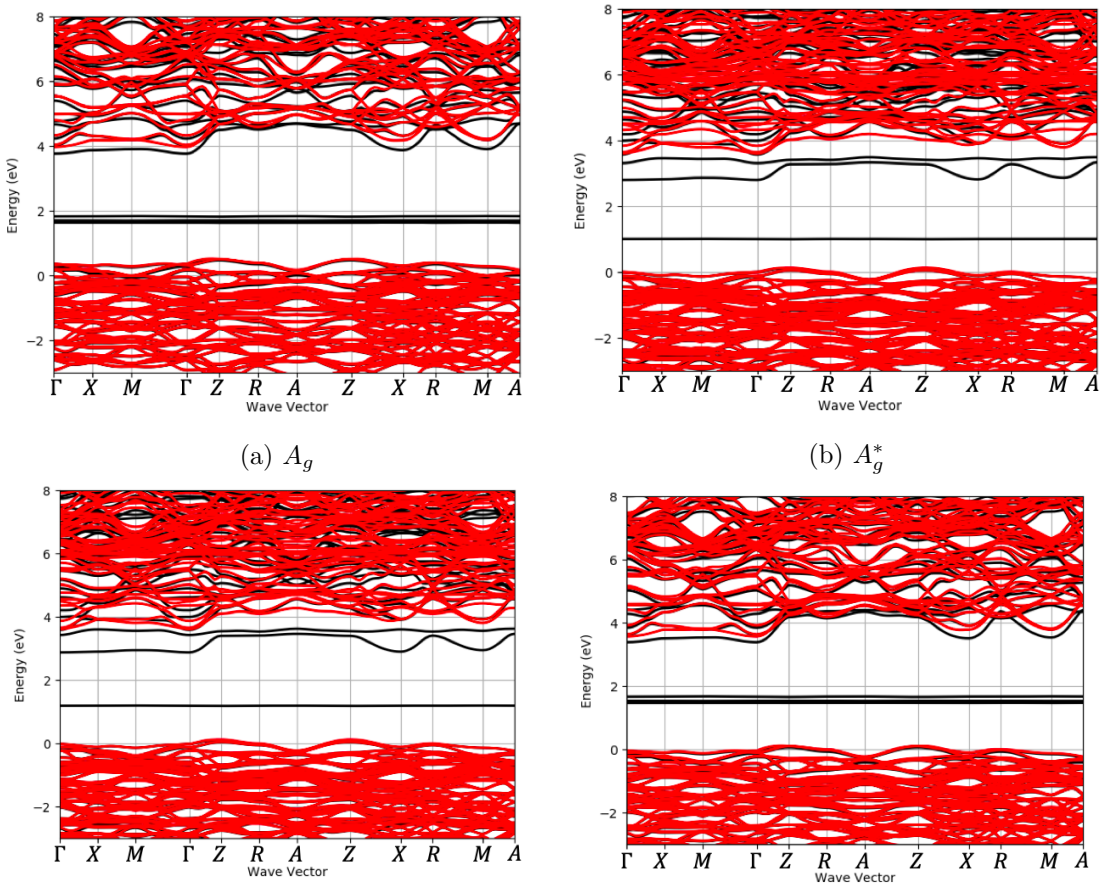

(a) A_g (b) A_g^*

(c) A_e^* (d) A_e

Figure 5.1: Electronic band structure of SALON:Eu. A_g, A_g^*, A_e^*, A_e refers to the notation used in figure 3.5. Black and red curves distinguishes spin up from spin down electrons, respectively.

5.1.2 Excited state relaxation

The goal of this section is to understand what is happening during the relaxation process of the system just after the 4f-5d transition (figure 5.3). To do that, the local environment of europium is analysed with the ground state positions of atoms (A_g and A_g^* states) and is compared with the excited state positions of atoms (A_e^* and A_e states). This local environment is formed by 4 nitrogen and 4 oxygen atoms that form a nearly cubic shape. The effect on more distant atoms has not be considered in this work.
Figure 5.4 allows to visualise the displacement of atoms in the environment of europium during the relaxation in the excited state. A more quantitative comparison between ground

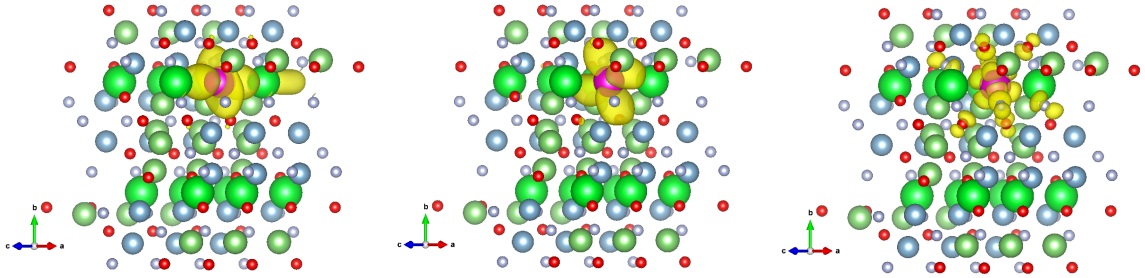

Figure 5.2: Wave function norm of europium at Γ in A_e^* state of left : $5d_{z^2}$ orbital, middle : $5d_{xy}$, right : $4f$. Supercell shown here is composed of 108 atoms.

and excited state environment is provided in table 5.1. From this, several observations can be made on the structural changes when passing from ground 4f to excited 5d state :

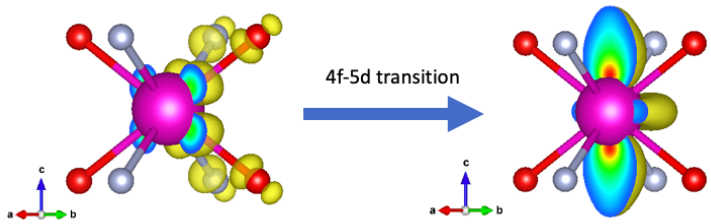

Figure 5.3: Left : local environment of ground state europium and its highest occupied orbital 4f. Right : local environment of excited state europium and its highest occupied orbital 5d, 4f orbital is now unoccupied.

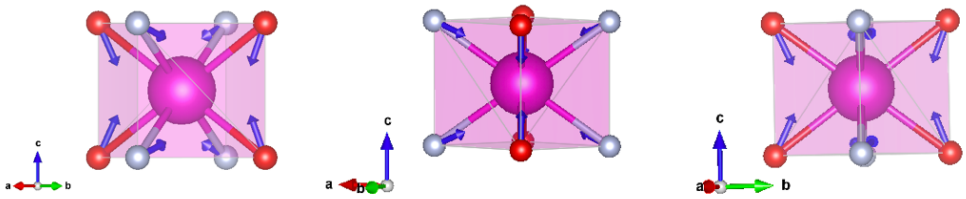

Figure 5.4: Local environment of ground state europium from different views. The vectors show the displacement of the surrounding atoms during relaxation in the excited state. To help visualisation, the vector's magnitude was multiplied by a factor 30.

- The most notable effect is the decrease of the Eu-N and Eu-O bond lengths. In [61], the following explanation is given to explain this effect : the bond length between an f-element ion in a $4f^N$ configuration and ligands is realized by the interaction between the $5p^6$ shell and the ligand's valence electrons. When the ion is in a $4f^{N-1}5d$ configuration, additional covalent interactions appear (mostly electron transfer from the ligand to the inner $4f$ hole) that shorten the bond length. We could also argue

	Ground state	Excited state	Difference
Eu-N length [Å]	2.78335	2.74802	-0.03533
Eu-O length [Å]	2.67863	2.63891	-0.03972
Average bond length [Å]	2.7310	2.6935	-0.0375
Polyhedral volume [Å^3]	31.1143	29.9506	-1.1637
Angle (N-Eu-N) [°]	70.3571	70.6347	0.2776
Angle (O-Eu-O) [°]	73.6716	72.7341	-0.9375

Table 5.1: Comparison between the nearly cubic environment of europium atom in ground state with excited state.

that excited Eu^{2+} in $4f^6 5d$ configuration gets closer to Eu^{3+} configuration, leading to stronger Eu-O and Eu-N bonds.

- Consequence of the bond lengths decrease, the volume of the local environment decreases as well (about 3.7% decrease).
- The acute angle formed by nitrogens and europium atoms (see figure 5.4 middle) increases of 0.2776 °.
- On the contrary, the acute angle formed by oxygen and europium atoms (see figure 5.4 right) decreases of 0.9375 °. Those angle effects are not simple to interpret. An idea could be that this angle variation comes from the change in electron density around europium induced by $4f$-$5d$ transition (for instance the lobes of the 5d occupied orbitals could repel the oxygen ions which would explain the angle increase).

It is also possible to analyse the environment change with a vector decomposition. The idea is to decompose the vector associated to Eu-O/Eu-N bond in excited state into a parallel and perpendicular component of the vector associated to Eu-O/Eu-N bond in ground state (figure 5.5). We write :

$$\boldsymbol{R}_{ex} = \boldsymbol{R}_{ex,\parallel} + \boldsymbol{R}_{ex,\perp} = (1+\alpha)\boldsymbol{R}_{gs} + \beta\boldsymbol{R}_{gs,\perp} \tag{5.1}$$

$\boldsymbol{R}_{gs,\perp}$ is here defined as a vector of same magnitude than $\boldsymbol{R}_{gs}$ and perpendicular to it. The value of α gives an information on the change along the axis formed by the ground state vector. The value of β gives an information on the change perpendicular to the axis formed by the ground state vector, it indicates how $\boldsymbol{R}_{ex}$ has rotated around $\boldsymbol{R}_{gs}$.
For Eu-O bonds, $\alpha = -0.0149$ and $\beta = 0.0080$. For Eu-N bonds, $\alpha = -0.0127$ and $\beta = 0.0052$. From this, it is clear that the dominant effect is the bond length shortening parallel to the initial ground state bond. This shortening is bigger for Eu-O bond. The rotation effect is about two times smaller but is not negligible nonetheless. Also, we observe a bigger β for Eu-O bonds (which confirms the bigger angle change).

5.2 Results of the 1D-CCM

First of all, a convergence study on the energies with respect to the plane wave cut-off *ecut* was performed (see figure 5.6). It can be seen that while the absolute energies are not

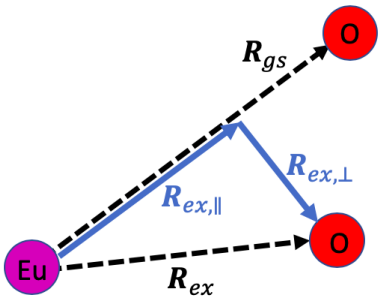

Figure 5.5: Excited state vector decomposition

completely converged (energy change of $\approx 3 \cdot 10^{-3}$ eV/atom between *ecut*=35Ha and *ecut* =45Ha) , their differences are well converged (energy change of $\approx 10^{-6}$ eV/atom between *ecut*=35Ha and *ecut* =45Ha). Since it is only the energy differences that are relevant for this study, *ecut*=35Ha was chosen as it gave reasonable converged results. The same convergence study was performed with respect to the number of k-points : a 2x2x2 k-point mesh was chosen.

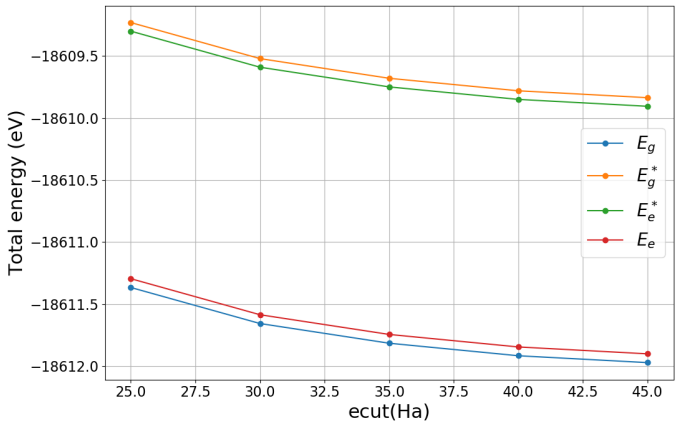

Figure 5.6: Convergence study of the ground/excited state energies in their relaxed/unrelaxed geometries (see figure 3.5 for the legend) as a function of the plane wave cutt-of. While the absolute energies are not completely converged (energy change of $\approx 3 \cdot 10^{-3}$ eV/atom between ecut=35Ha and ecut =45Ha) , their differences are well converged (energy change of $\approx 10^{-6}$ eV/atom between ecut=35Ha and ecut =45Ha).

Table 5.2 presents the relevant energies computed with ABINIT, the parameters entering the 1D model (calculated with equations of section 3.5) are also shown. Based on these computations, SALON:Eu emits photons at around 2 eV which is a first good agreement with the experimental emission peak of 2.019 eV. A comparison with the similar compound [LiAl3N4]:Eu^{2+} or SLA is provided. We observe that their transition energies are quite similar. We can also compare it with the luminescent properties of numerous compounds detailed in [38]. Globally, SALON exhibits a small Stokes shift ΔS, a very small modal mass M, small displacement ΔR and consequently a small ΔQ (the smallest of the compounds

	E_{ZPL} (eV)	E_{abs} (eV)	E_{em} (eV)	$E_{FC,g}$ (eV)	$E_{FC,e}$ (eV)	ΔS (eV)	ΔC (eV)
SALON:Eu	2.0668	2.1357	1.9958	0.07104	0.06883	0.13987	-0.0022
SLA:Eu 1	2.038	2.095	1.962	0.076	0.057	0.133	0.019
SLA:Eu 2	2.049	2.16	1.989	0.06	0.111	0.171	0.052
	ΔQ ($\sqrt{amu}$Å)	ΔR (Å)	M (amu)	$\hbar\Omega_g$ (meV)	$\hbar\Omega_e$ (meV)	S_{em} /	S_{abs} /
SALON:Eu	0.5992	0.14714	16.5869	40.668	40.032	1.7468	1.7195
SLA:Eu 1	0.756	0.172	19.28	33.4	29.0	2.63	1.71
SLA:Eu 2	1.222	0.143	73.01	18.3	25.0	3.27	4.46

Table 5.2: Luminescent parameters deduced from 1D-CCM and ABINIT results. Comparison is provided with $[LiAl_3N_4]$:Eu^{2+} (SLA).

studied in [38]). This means that the geometry of the system do not change that much when the system is excited. We observe also that the effective vibrational energies in the ground and excited state are close to each other, meaning that the curvature of the Born-Oppenheimer potential in the ground and excited state are quite similar (which is not true for SLA). Moreover, these effective vibrational frequencies are the highest of the compounds. Finally, the combination of a small ground state Condon shift ($E_{FC,g}$) with a high ground state effective vibrational frequency $\hbar\Omega_g$ gives a very small emission Huang Rhys parameter S_{em} (smallest of the compound list [38])! The consequence of all of these interesting parameters with extreme values on the emission spectrum will be studied in the next sections. It can also be seen that Huang-Rhys factor (S_{em}) and phonon frequency ($\hbar\Omega_g$) are consistent with the Stokes shift ΔS : as explained in [62], $\Delta S = 0.13987$ eV should lie in between $(2S_{em} - 1)\hbar\Omega_g = 0.1014$ eV and $2S_{em}\hbar\Omega_g = 0.1420$ eV.
The harmonicity of the potentials was checked by computing the energies for several geometries positions (black dots on figure 5.7). A second-order polynomial fit of these energies is displayed in red. The arrows indicate the position of the ground state and excited state minimum. Absorption and emission energies are also displayed. It is possible to extend those fitted parabolas until they cross. The cross-over point is calculated to be at $\Delta Q = 6.376$ (or $\Delta R = 1.567$Å) with an energy barrier $E_{fd} = 5.169$ eV. Actually, for such high values of effective displacement ΔR, harmonic approximation is certainly not valid. Thus this very high value of E_{fd} does not have particular significance. Still, the energy barrier for cross-over mechanism is way bigger than the energy barrier for auto-ionization (0.445 eV). One can conclude that this latter mechanism is the dominant one in thermal quenching process.

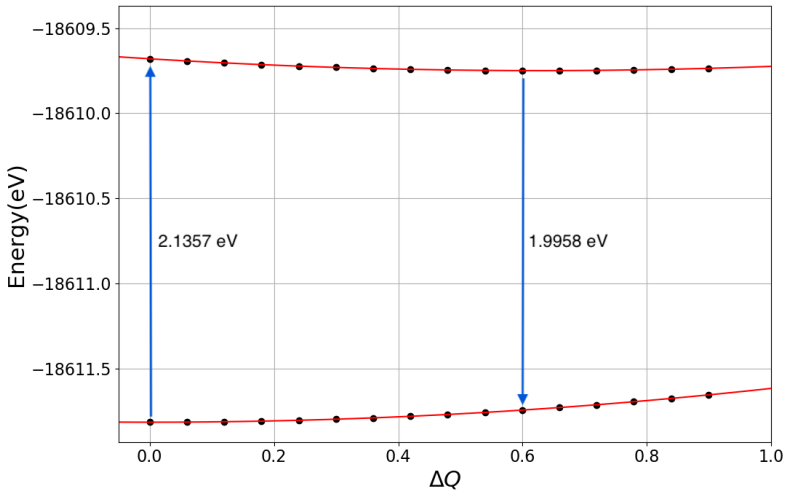

Figure 5.7: 4f (down) an 5d (up) energy curves as a function of the change in normal coordinate ΔQ. Black dots are energies computed in ABINIT for several geometries position and red curve is a second-order polynomial fitting.

5.3 Emission spectrum with the 1D-CCM

In this section, we will use what we have seen in theory section 3.6 on how we could estimate luminescence intensity spectrum based on a quantum formulation of the Franck-Condon principle principle applied to a one-dimensional configuration coordinate model (1D-CCM)

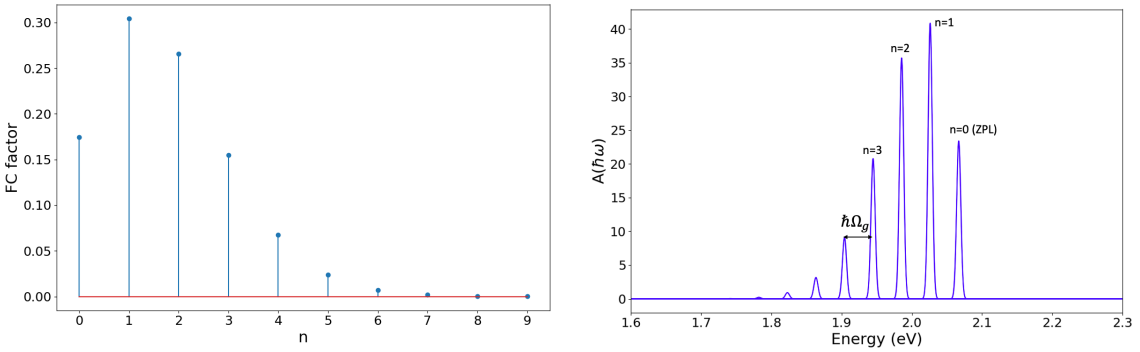

Figure 5.8: Left : Franck Condon factor $|\langle\chi_{g,n}|\chi_{e,0}\rangle|^2 = \exp\{-S\}\frac{S^n}{n!}$ for S=1.7468. Right : Emission spectral function $A(\hbar\omega)$ with a small gaussian broadening. Each transition is spaced by $\hbar\Omega_g$ and the intensity of each transition is given by the corresponding F-C factor.

A Python code was used to estimate the luminescence intensity spectrum at zero temperature based on the different parameters of the 1D-CCM provided by ABINIT. First, we observe (figure 5.8) that, due to a small Huang Rhys factor $S_{em} = 1.7468$, the F-C factors become quickly negligible as n (the vibrational state of electronic ground state) grows. This small S_{em} leads also to an asymmetric F-C factor curve with an important part of the intensity that comes from the zero phonon line (ZPL) and with a peak for n=1. This

contrasts with phosphors with high S_{em} where the F-C factor curve looks like a symmetric Gaussian curve. This results in a small number of transitions that participates to the line shape, hence giving a small bandwidth.
Figure 5.9 (a-b-c-d) shows the spectral emission function $A(\hbar\omega)$ for different inhomogeneous gaussian broadening w (the full width at half maximum of each small gaussian associated to each transition). For 50 and 70 meV, $A(\hbar\omega)$ is compared to the luminescent intensity spectrum $L(\hbar\omega) = C\omega^3 A(\hbar\omega)$. Figure 5.9 (e) shows the variation of the total FWHM as a function of the gaussian width w. From this analysis, it can be seen that setting $w = 63meV$ allows to match the experimental total FWHM (41 nm with emission maximum at 614nm, which gives a FWHM in energy of 0.135 eV). This experimental value can also be compared with the theoretical one derived within the semi-classical approximation (equation 3.91). An underestimation of 8.43 meV (-6.24%) is observed. It is also observed that due to the factor ω^3, the location of the peak of $L(\hbar\omega)$ (2.017 eV) is slightly shifted (+5 meV) toward higher energies compared to the location of the peak of $A(\hbar\omega)$ (2.012 eV). Notice finally that the emission peak is not exactly the same than E_{em} (1.9958 eV).

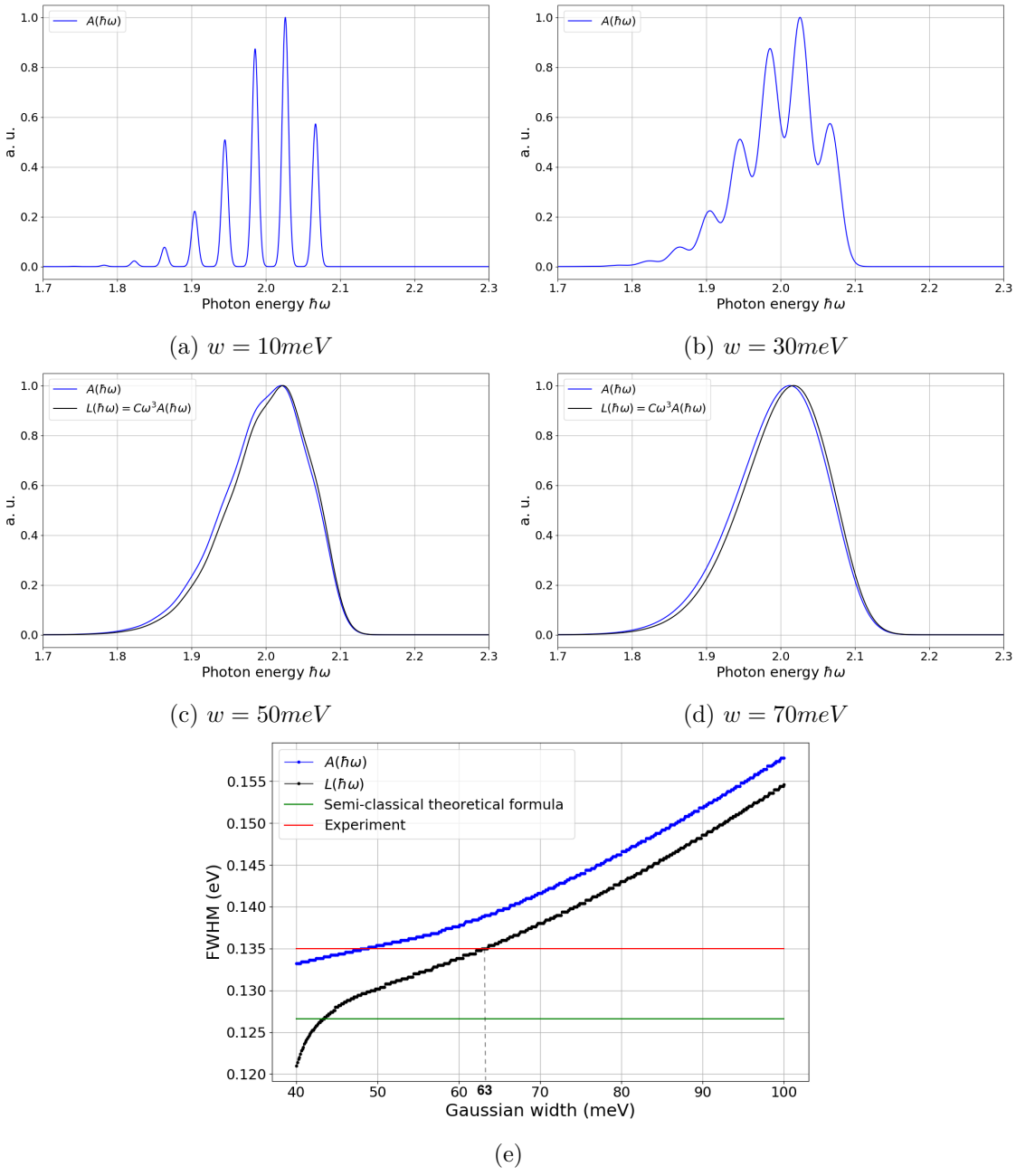

(a) $w = 10meV$ (b) $w = 30meV$

(c) $w = 50meV$ (d) $w = 70meV$

(e)

Figure 5.9: (a) to (d) : Spectral emission function $A(\hbar\omega)$ for different inhomogeneous gaussian broadening w (the full width at half maximum of each small gaussian). For 50 and 70 meV, $A(\hbar\omega)$ is compared to the luminescent intensity spectrum $L(\hbar\omega) = C\omega^3 A(\hbar\omega)$. All curves were normalized to one for an easier comparison. (e) Variation of the total FWHM as a function of the gaussian width w. Setting $w = 63meV$ allows to match the experimental total FWHM of 0.135 eV. Green line shows the theoretical FWHM based on semi-classical formula 3.91.

5.4 Phonon decomposition

The calculation of the emission spectrum shape in the previous section was based on a one dimensional configuration coordinate model where it is assumed that the complexity of all the solid vibration modes can be reduced to one effective vibration mode (here $\hbar\Omega_g = 40.668$ meV). The goal of this section is to present what is obtained when all the phonon modes are taken into account. In this regard, we will use the theoretical background presented in 3.6.4 and 3.6.5.

5.4.1 Phonon DOS

The phonon modes were calculated at Γ in DFPT for a 1x1x3 supercell (54 atoms) for both the bulk SALON and europium doped SALON (where one of the six Sr atom is replaced by Eu atom, 16.67 % doping rate) in its 4f ground state. GGA-PBE functionnal and PAW pseudopotentials were used. *Ecut* was set to 30 Ha and a 2x2x2 k-point mesh was used. The resulting phonon DOS are presented on figure 5.10. Some observations can be made :

- For frequencies bigger than 0.03 eV, no noticeable change is observed between bulk and doped case.
- For frequencies lower than 0.03 eV, differences are observed : the addition of an europium atom induces a change in the shape of strontium peaks. Also, a new peak at 0.008 eV involving mostly europium appears.

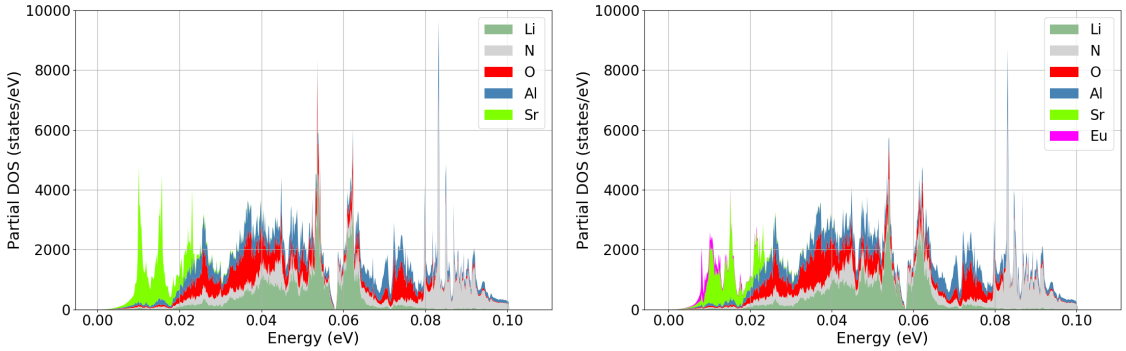

(a) Phonon DOS of undoped SALON (b) Phonon DOS of europium doped SALON

Figure 5.10: Comparison between the phonon DOS of bulk SALON and SALON:Eu.

5.4.2 Spectral function $S(\hbar\omega)$

A python code was used to compute all the relevant quantities described in the theoretical background section 3.6.4. Table 5.3 presents a numerical comparison between parameters deduced from the phonon decomposition approach (with bulk SALON phonon modes and doped SALON phonon modes) and from the 1D model approach. It is important to note that the way to obtain Ω_{eff} and S_{em} are different from one method to the other.

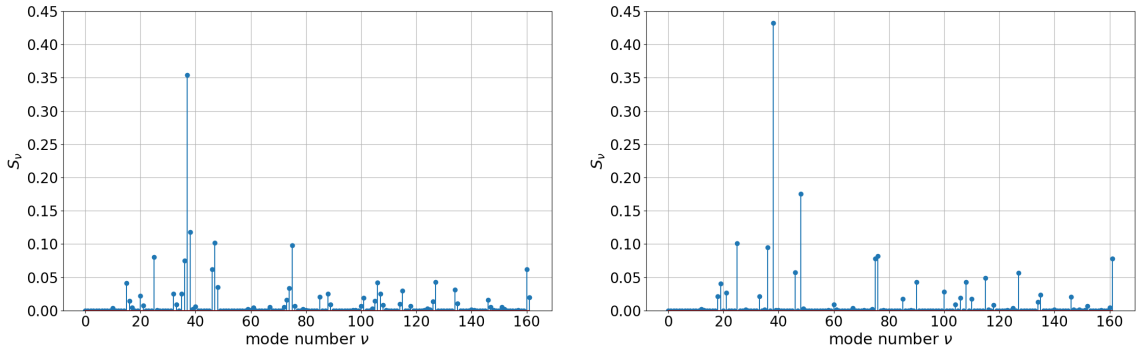

(a) Undoped SALON (b) Europium doped SALON

Figure 5.11: Partial Huang Rhys factors S_ν (calculated with equation 3.106) for undoped and doped SALON.

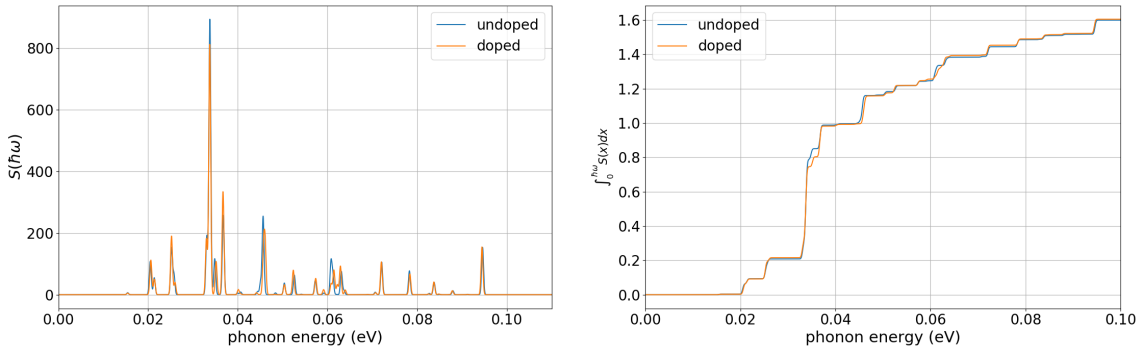

Figure 5.12: Left : Spectral function of electron-phonon coupling $S(\hbar\omega)$ (equation 3.107) in the undoped and doped case. Right : Integral of $S(\hbar\omega)$

The phonon decomposition approach requires the computation of all the phonon modes to which are associated relative weights that depends on the coupling between the mode and the geometry change due to 4f-5d optical transition. No energy difference is needed in this approach. On the contrary, the 1D-CCM approach requires only differences in energy between unrelaxed and relaxed state. In both approach, the geometry change ΔQ is needed.
The discrete partial Huang Rhys factors S_ν are shown for the undoped and doped case on figure 5.11. We can also look at the spectral functions of electron-phonon coupling $S(\hbar\omega)$ presented on figure 5.12 with a small smearing. The integral of those spectral functions are also displayed. Some observations can be made :

- Only few differences are observed between the bulk case and the doped case. This means that the phonon modes that contributes to the optical transitions are already present in the bulk material without the addition of Europium doping agent. For numerical calculation, this means that in first approximation, the bulk modes of SALON are sufficient to predict its luminescent properties.

	ΔQ $(amu^{1/2}\text{Å})$	$\Omega_{eff}(meV)$	S_{em}
phonon mode decomposition : bulk SALON	0.5992	40.519	1.5986
phonon mode decomposition : doped SALON	0.5992	40.664	1.6038
1D-CCM	0.5992	40.668	1.7468

Table 5.3: Comparison of ΔQ, Ω_{eff} and Huang Rhys parameter S_{em} with three methods : phonon mode decomposition for bulk and doped SALON and 1D-CCM based on Δ SCF method (as described in previous section). For the phonon decomposition, ΔQ, Ω_{eff} and S_{em} are calculated using equation 3.104, 3.105 and 3.106, respectively.

- The spectral function $S(\hbar\omega)$ is dominated by one peak at around 33.7 meV (mode number ν=39 for doped phonon modes and ν=38 for undoped phonon modes) which is thus the mode that couples the most with the optical transition. Its partial Huang Rhys factor S_ν is 0.354 (22.16 % of the total Huang Rhys factor) for bulk SALON and 0.433 (26.97 % of the total Huang Rhys factor) for the doped SALON. For a visualization of this mode, the website `"https://henriquemiranda.github.io/phononwebsite/index.html"` was used. A short video that shows this mode in the bulk can be accessed with this link : `https://www.youtube.com/watch?v=Df07ih8EUpE`. It is interesting to see with this animation that, for this mode, the local environment of europium is kind of "breathing" around the central atom. This allows to understand why this mode couples strongly with structural relaxation accompanying 4f-5d transition that involve mostly a change in the Eu-O and Eu-N bond length parallel to the initial bond. We can make the link with figure 5.4 that showed the atomic relaxation in the coordination environment of europium atom. On figure 5.13, this atomic relaxation (blue arrows) is compared with the eigenvectors of this mode (green arrows).

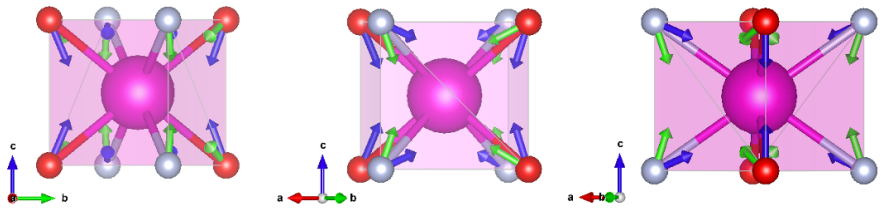

Figure 5.13: Comparison between the atomic relaxation displacement associated to the 4f-5d transition (blue arrows) with the eigenvectors of the mode that couples the most with this relaxation (green arrows).

5.4.3 Emission spectrum based on generating function approach

Following the generating function approach described in subsection 3.6.5, the luminescence intensity $L(\hbar\omega)$ shape was calculated based on the the spectral function $S(\hbar\omega)$ of doped

SALON. As we have seen, $S(t)$ can be written as :

$$S(t) = \sum_{\nu} S_\nu e^{-i\omega_\nu t} \tag{5.2}$$

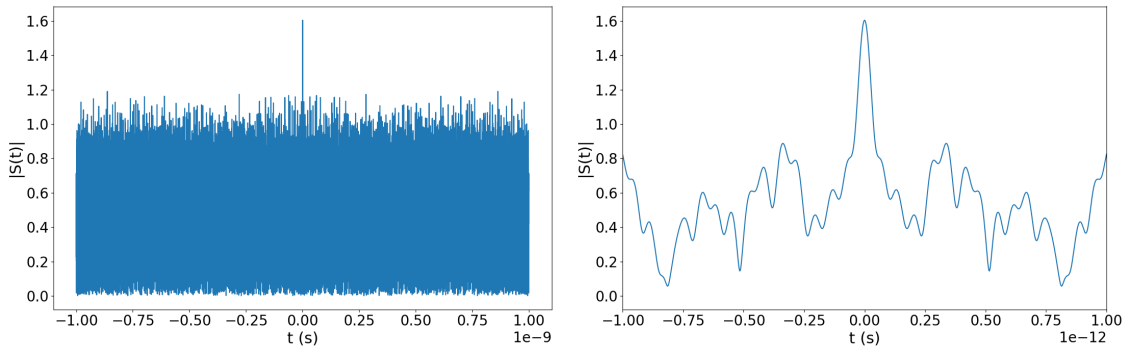

Figure 5.14: Left : module of $S(t)$ as calculated with equation 5.2 on the total time time-window considered. Right : zoom near $t = 0$, notice that $S(0) = \sum_\nu S_\nu$

which is a sum of oscillating waves of pulsation ω_ν and amplitude S_ν The module $S(t)$ is shown on figure 5.14 on the total time-window considered and with a zoom near $t = 0$. Notice that the time window that give converged results should be here at least 0.2 ns (So that all the various mode frequencies are correctly captured). Indeed, the time discretization should be thin enough (the converged result is obtain with 10^6 time steps)

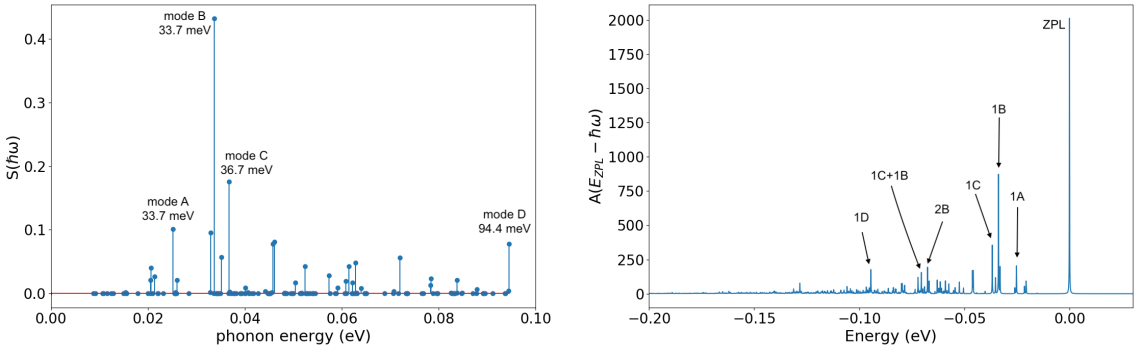

Figure 5.15: Left : Spectral function of electron-phonon coupling $S(\hbar\omega)$ where the four modes that couples the most are identified. Right : Emission spectral function based on the generating function approach (without broadening) that provides a full decomposition of the spectrum into the zero phonon line and the full phonon side-band (with first order, second order,... phonon replicas)

Then, a fast Fourier transform algorithm is used to compute the Fourier transform of the generating function $G(t) = e^{S(t)-S(0)}$ which gives the emission spectral function shown on figure 5.15 (left) where the ZPL is set at 0. This allows to clearly identify the different phonon side bands that participates to the emission spectrum. Four characteristic modes (named A-B-C-D) that couples strongly are explicitly given. First order peaks (emission

of one phonon) are pronounced and some second order peaks (emission of two phonons) can be identified but higher order do not participate a lot to the spectrum. The weight of the ZPL in the spectra can be simply calculated $w_{ZPL} = e^{-S} \approx 0.168$ meaning that about 16.8% of the emitted light comes from the zero phonon line and thus 83.2% comes from the phonon sideband.
Finally, $A(\hbar\omega)$ is convoluted with a gaussian function of fixed fwhm. Figure 5.16 shows the normalized luminescence intensity $L(\hbar\omega)$ for different gaussian fwhm w. A comparison with the 1D model (described in previous section) is provided. We see that at small w, there is a clear difference between the phonon decomposition and the 1D model which is expected since the 1D model is unable to reproduce the full phonon sideband. However, as the broadening w of each phonon line increases, the transition becomes indistinguishable and the 1D model gets closer to the phonon decomposition model. At $w = 63meV$ (the broadening width that allows to match experimental total FWHM in the 1D model), it appears that the 1D model becomes a fairly good approximation of the full multi-dimensional calculation based on phonons.

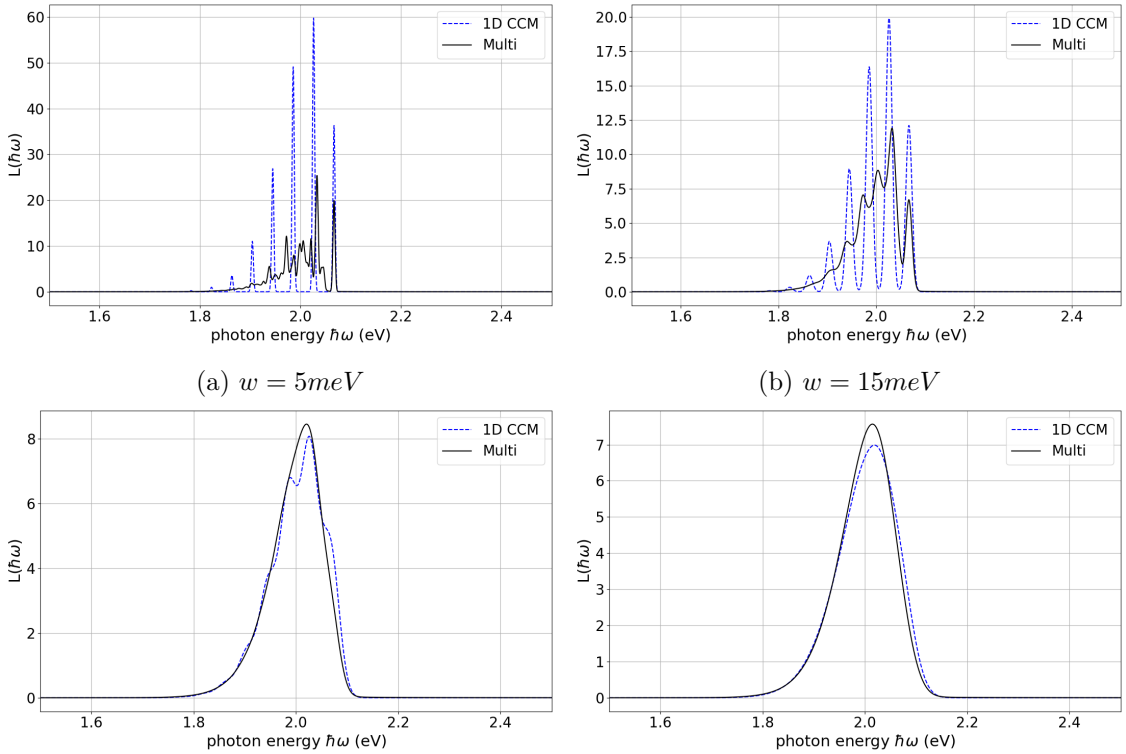

(a) $w = 5meV$ (b) $w = 15meV$

(c) $w = 40meV$ (d) $w = 63meV$

Figure 5.16: Normalized luminescence intensity $L(\hbar\omega)$ (such that the area under the curve is one) based on the multi-dimensional model with a full phonon decomposition compared with the 1D model. Different gaussian width w are compared.

.

Chapter 6

Luminescent properties results at T≠0K

Contents

We have seen that the 1D model is sufficient to fairly reproduce the complete phonon decomposition and to reproduce experimental full width at half maximum at low temperature. We will thus extend the use of the 1D model by analysing the effect of temperature within this approach. We will first see how the spectral function $A(\hbar\omega)$ and the luminescence intensity $L(\hbar\omega) = C\omega^3 A(\hbar\omega)$ are affected by the fact that transitions from higher vibrational levels are now possible. Then we will add the effect of thermal expansion thanks to the thermal expansion coefficient calculated for the bulk SALON. We will then compare the theoretical temperature dependence with the experimental one. It will be shown that this approach is sufficient to explain the temperature dependence of the FWHM while it is not sufficient to explain the experimental shift of the emission peak with temperature. Finally, a new method to predict the luminescence intensity spectrum based on first-principles Born-Oppenheimer molecular dynamic simulation will be presented.

6.1 Transitions from higher vibrational levels with 1D-CCM

6.1.1 Thermal occupation and Franck Condon factors

As temperature is now different of zero, we now have to consider that vibrational states m $\neq 0$ can be populated in the electronic excited 5d state. The emission spectral function must thus take into account transitions from any m (vibrational state number in excited state) to any n (vibrational state number in ground state). We recall the formula of the theoretical section that will be used here :

$$A(\hbar\omega) = \sum_{n,m} p_m(T) |\langle \chi_{g,n} | \chi_{e,m} \rangle|^2 \delta(E_{ZPL} + m\hbar\Omega_e - n\hbar\Omega_g - \hbar\omega) \tag{6.1}$$

where $p_m(T)$ is a thermal occupation factor (i.e. the probability of finding the lattice eigenfunction in state m).

$$p_m(T) = a^m(1-a) \tag{6.2}$$

where $a = \exp\left\{-\frac{\hbar\Omega_e}{k_B T}\right\}$. The temperature dependence of this last equation is displayed on figure 6.1a for $\hbar\Omega_e = 40.032$ meV at different m.

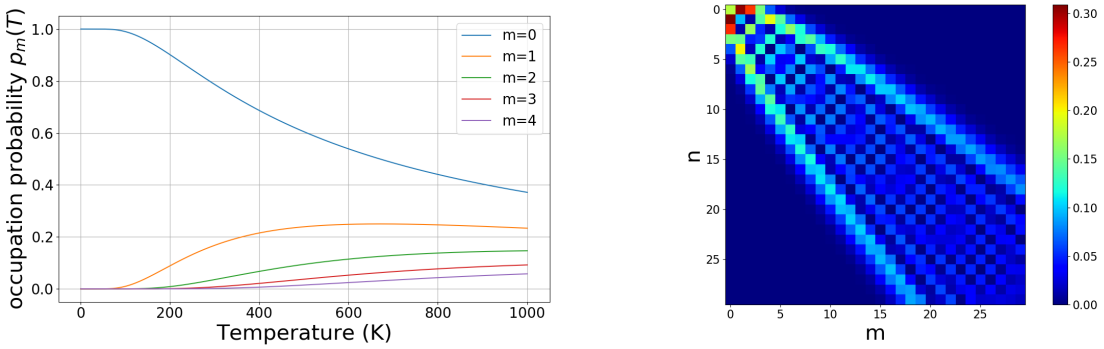

(a) (b)

Figure 6.1: (a) Thermal occupation factor $p_m(T)$ with $\hbar\Omega_e = 40.032$ meV for different m. (b) Color map of the F-C factors $|\langle \chi_{g,n} | \chi_{e,m} \rangle|^2$ where the distance between the two quantum harmonic oscillators and their respective frequency are the ones of table 5.2 ($\Delta R = 0.14717$Å, $\hbar\Omega_g = 40.668$ meV, $\hbar\Omega_e = 40.032$ meV)

The different F-C overlaps were computed by numerical integration. Figure 6.1b shows a 3D chart of the results : each point block (m,n) corresponds to a transition from excited state $\chi_{e,m}$ to ground state $\chi_{g,n}$. The "strength" of this transition is then given by the corresponding F-C factor $|\langle \chi_{g,n} | \chi_{e,m} \rangle|^2$ that is represented by the color. Notice the symmetry of the pattern around the line n=m (this is because we have $\hbar\Omega_e \approx \hbar\Omega_g$) implying a symmetry between emission and absorption spectral function. This symmetry is obviously preserved by changing ΔR and is broken if we set a difference between Ω_e and Ω_g. We can go further and look at what the F-C factors look like when we change some parameters (for instance by varying the distance between the two quantum harmonic oscillators ΔR or if we modify their curvature trough Ω_e and Ω_g). This is shown on figure 6.2. For each case, the Huang Rhys factors are given ($S = \Omega\Delta Q^2/2\hbar$ with $\Delta Q^2 = M\Delta R^2$).

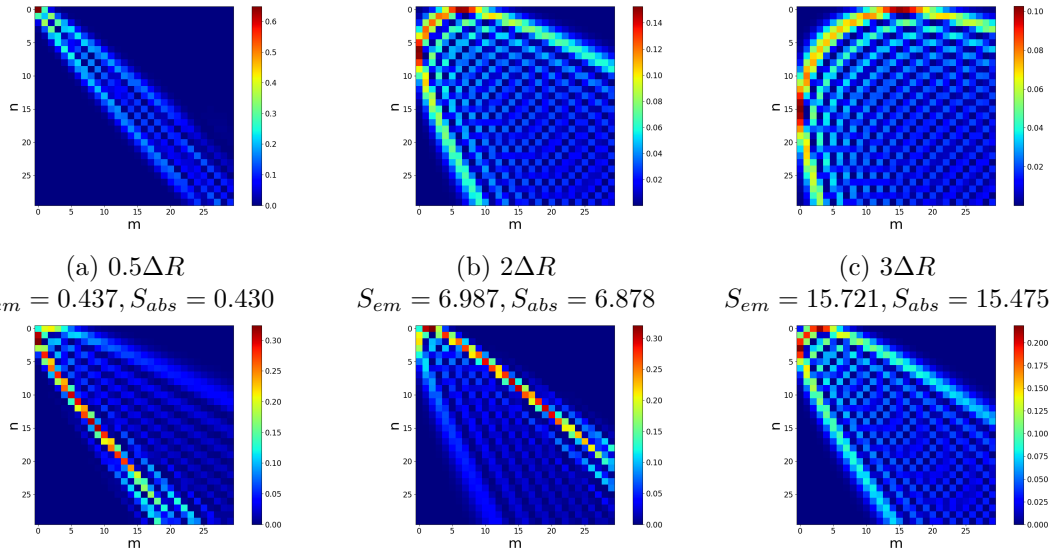

(a) $0.5\Delta R$
$S_{em} = 0.437, S_{abs} = 0.430$

(b) $2\Delta R$
$S_{em} = 6.987, S_{abs} = 6.878$

(c) $3\Delta R$
$S_{em} = 15.721, S_{abs} = 15.475$

(d) $1.5\Omega_g$, $1\Omega_e$
$S_{em} = 2.620, S_{abs} = 1.719$

(e) $1.5\Omega_e$ $1\Omega_g$
$S_{em} = 1.746, S_{abs} = 2.579$

(f) $2\Omega_g, 2\Omega_e$
$S_{em} = 3.494, S_{abs} = 3.439$

Figure 6.2: Up : Effect of ΔR on the F-C factors. $\Omega_{e,g}$ are fixed to their original values and the original ΔR is multiplied by a constant. Bottom : Effect of Ω_e and Ω_g on the F-C factors. ΔR is fixed to its original value and the original $\Omega_{e,g}$ are multiplied by a constant. For each case, the new Huang Rhys factors S_{em} and S_{abs} are given.

Figure 6.3 (left) shows the occupation probabilities p_m for different temperatures. We observe that even at 500K, p_m stays relatively small for high m. This can be explained by the high value of $\hbar\Omega_e$ (see formula 6.2). Figure 6.3 (right) shows the decomposition of the corresponding emission spectral function $A(\hbar\omega)$, red gaussian correspond to transitions from m=0, blue to transitions from m=1, green to transitions from m=2,... The width of each gaussian was fixed to $w = 63$ meV (the value that enable to match experimental FWHM at 0 K.)
Finally, figure 6.4 shows the luminescence intensity $L(\hbar\omega)$ with a normalization to one for each curve to allow a better comparison.

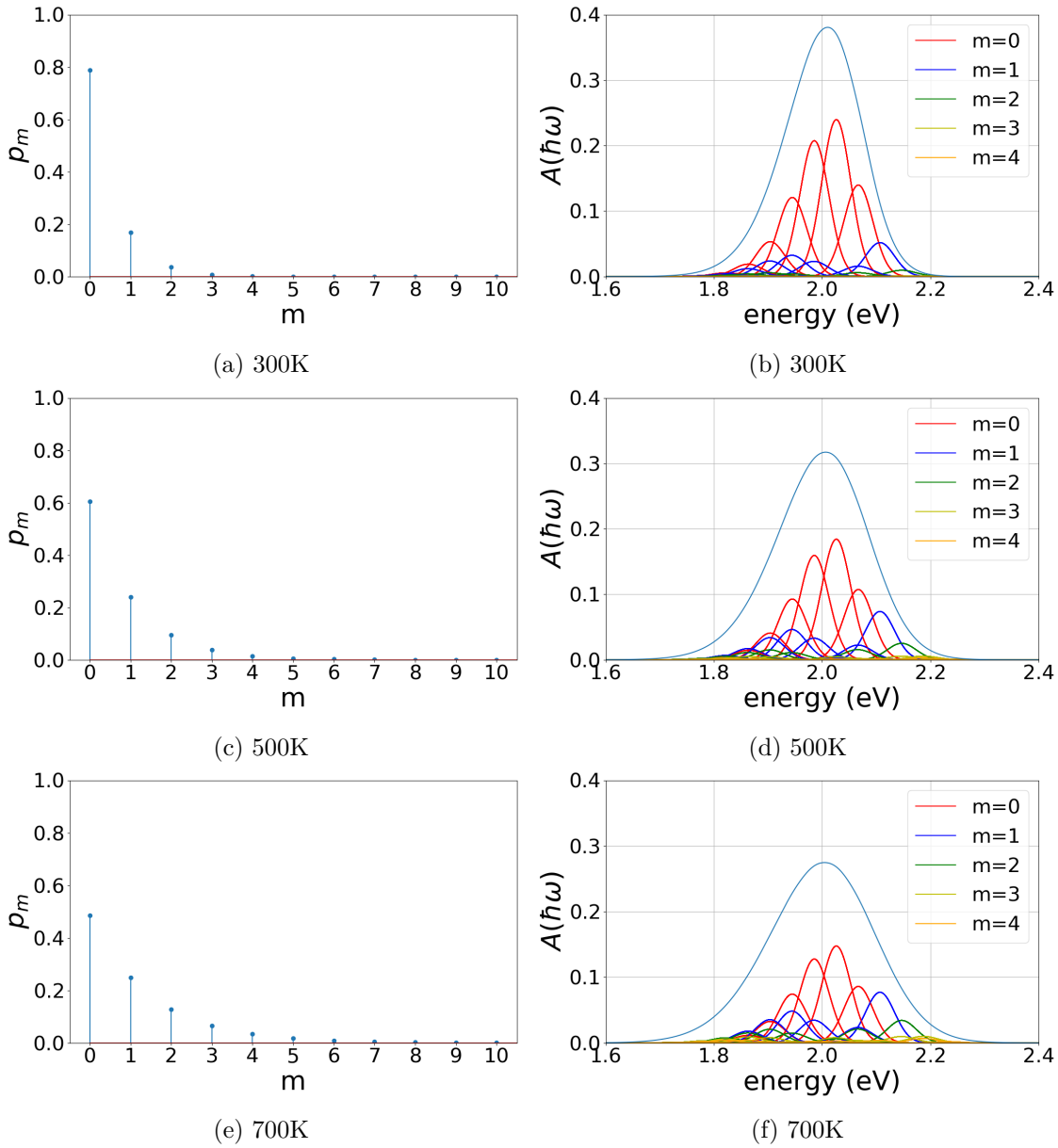

(a) 300K (b) 300K

(c) 500K (d) 500K

(e) 700K (f) 700K

Figure 6.3: Up :occupation probabilities p_m for different temperatures. Bottom: Decomposition of the corresponding spectral function $A(\hbar\omega)$. Each color indicates transitions from one given initial vibrational state m. The upper blue curve is the total (sum of all the small gaussians) emission spectral function $A(\hbar\omega)$. Notice how $A(\hbar\omega)$ is flattened with increasing temperature.

6.1.2 FWHM and emission shift

In order to have a better understanding of the temperature effect on the emission spectral function $A(\hbar\omega)$ and on the luminescence intensity $L(\hbar\omega) = C\omega^3 A(\hbar\omega)$, it is then possible

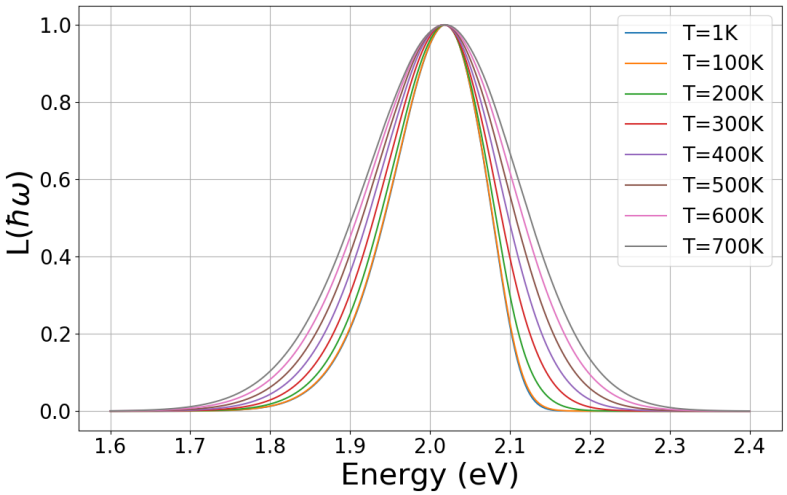

Figure 6.4: Luminescence intensity $L(\hbar\omega)$ normalized to one for different temperatures (in the 1D-CCM, taking only into account the effect of occupation of higher vibrational levels to obtain the temperature dependence).

to compute for any temperature the total FWHM and the location of the maximum E_{max}. Obviously, going to high temperature requires to add in the computation transitions that start at high vibrational level m (for instance at T=1500K, it was observed that considering vibrational levels up to m=15 and n=40 was necessary to obtain converged result which becomes quickly computationally demanding). The FWHM(T) and E_{max}(T) are shown on figure 6.5.

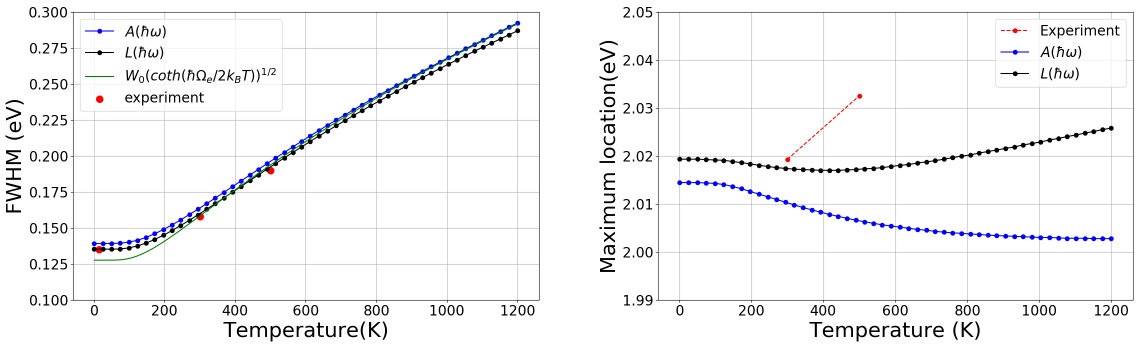

Figure 6.5: Left : FWHM of $A(\hbar\omega)$ and $L(\hbar\omega)$ based on the quantum approach (with Franck-Condon factors), the width of the small gaussian compared with the theoretical formula based on semi-classical approximation (developed in section 3.6.3). Right : Variation of the position maximum of $A(\hbar\omega)$ as a function of temperature.

FWHM Figure 6.5 (left) presents the results of the computation of the FWHM of $A(\hbar\omega)$ and $L(\hbar\omega)$. For this calculation, the width of the gaussian w was fixed to 63 meV. We can first compare the variation of the FWHM of $L(\hbar\omega)$ with temperature with experimental

data (red point). The agreement seems very good. We can also compare the full quantum computation with the theoretical formula of the FWHM based on semi-classical approximation detailed in section 3.6.3 (green curve). Actually, this formula does not assume the ω^3 dependence of the luminescence intensity, so it should be compared with $A(\hbar\omega)$, the spectral emission function. It can be seen that at low temperature, semi-classical formula underestimate slightly the FWHM with respect to the full quantum calculation $A(\hbar\omega)$. As temperature increases, we observe that the semi-classical formula gets very close to the quantum computation. From this analysis, it seems that considering transitions from higher vibrational levels based on the one-dimensional configuration coordinate model is sufficient to reproduce the experimental FWHM temperature dependence.

Emission peak The temperature dependence of the location of the maximum (figure 6.5, right) is more tricky to interpret. Let us first focus on the variation of the maximum location of $A(\hbar\omega)$. A slight shift towards lower energies is observed. The explanation of this red shift is the following : we see that the location of the maximum is nearly constant up to about 100K where it begins to decrease : this threshold of 100K is attributed to the contribution of transitions from vibrational level m=1 (see figure 6.1a where we observe that $p_1(T)$ becomes occupied at $\approx$ 100K). Why do we observe a decrease then? It seems that this comes from the effect of the transition (m=1, n=3) (see figure 6.3) that is located really near to the maximum of the total curve at T=0K **but at lower energy** than this maximum. The transition (m=1,n=2) that is located at higher energy than the maximum (and thus should tends to blue shift the maximum with temperature increase) has a F-C factor that is nearly zero, meaning that the maximum is way more influenced by transition (m=1, n=3) when T increase. So with increasing temperature, the effect of the transition (m=1,n=3) becomes increasingly important and tends to shift the maximum of the curve to slightly lower energies (more than transitions to n≠3 as these are located further from the curve maximum or than transition n=2 that has a very small F-C factor). This effect is a purely quantum effect that originates from the shape of the Franck-Condon factors from vibrational state m=1 that has no classical analogy. Still, this effect is observed with the 1D-CCM framework, it is questionable to say that this has a real physical meaning since we should in principle consider all the phonon modes, leading to way more possible transitions (as it can be observed in the multi-dimensional model at T=0).

Let us look now at the variation of the emission maximum of the luminescence intensity $L(\hbar\omega)$. It appears that while the addition of the ω^3 factor has a negligible effect on the FWHM temperature dependence, this ω^3 factor has a huge impact on the temperature dependence of the emission shift! We observe first a red shift at low-temperature (that comes from the red shift of $A(\hbar\omega)$, then after a minimum at around 400K, the temperature dependence tends to be linear at high temperature with a slope of about 1.6 meV per 100K. This linear temperature dependence is also the result of a formula derived by Shionoya in [63] which is derived within a classical framework based on Maxwell-Boltzmann distribution. This classical framework and therefore the linear temperature dependence is valid as long as $\hbar\Omega >> k_BT$ (if not, Bose-Einstein statistics must be used) which is exactly what is observed in the quantum computation. Here $\hbar\Omega \approx 40meV$ while at the room temperature, $k_BT \approx 25meV$, meaning that due to this very high effective frequency, we are still in the

quantum regime at room temperature and it is therefore questionable to use formulas based on classical approximations.
Finally, when comparing with experimental blue shift, it appears that the model we have used is not able to describe the experimental blue shift that is way bigger than the one computed. Let us see if adding thermal expansion effect is enough to explain experimental data.

6.2 Thermal expansion effect

This section aims to give the results of the analysis of the thermal expansion on the luminescent properties of SALON:Eu^{2+} and especially how the luminescence intensity $L(\hbar\omega)$ is modified when we take into account this effect. To do that, 8 temperatures (from 0 to 700K per step of 100K) were chosen and to each temperature was associated a given relaxed crystal structure geometry with a **fixed volume calculated thanks to the thermal expansion coefficient computed previously**. For each volume, all the parameters entering the 1D model were calculated with ΔSCF method.
The problem becomes complicated since the energy levels of 5d and 4f states and the relaxed atomic geometries depend on volume and subsequently on temperature. All the parameters entering the spectral emission function $A(\hbar\omega)$ of equation 3.84 $(\Delta R, \Omega_{e,g}, E_{ZPL})$ could therefore in principle vary with the change in volume associated to temperature increase. To tackle this problem, the effect of these three parameters were studied separately by allowing one to change and the two others to stay fixed. From this preliminary study, we observed that it was the change in E_{ZPL} that has the greatest influence on the $A(\hbar\omega)$, the two others being negligible.

6.2.1 Change in E_{ZPL}

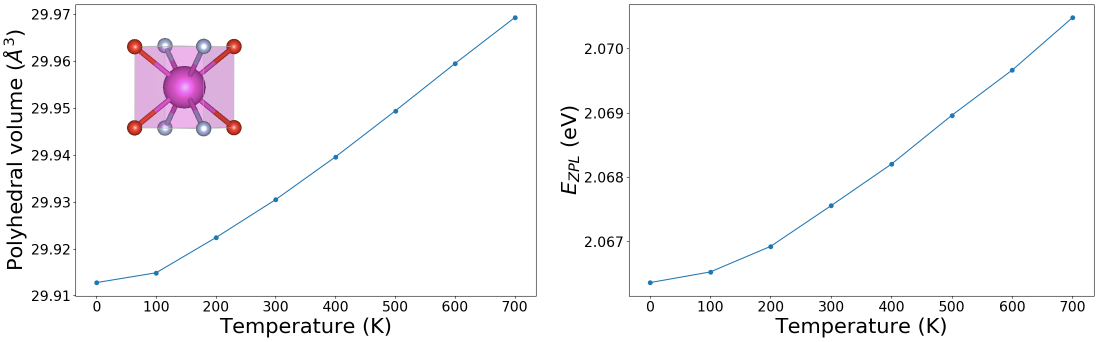

Figure 6.6: Left : change in the polyhedral volume composed of europium (in its excited state) and its local environment with temperature due to thermal expansion. Right : Change in E_{ZPL} with temperature associated to the thermal expansion. It was verified that this blue shift comes mostly from an elevation of of the 5d emitting level (which could be attributed to a decrease of the crystal field splitting with polyhedral volume increase). The slope of the change in E_{ZPL} in the linear regime is $\approx 0.75meV/100K$.

The change in E_{ZPL} with temperature is calculated to be a blue shift of about 0.75 meV / 100K in the linear regime (see figure 6.6 right). This blue shift is attributed to the increase in polyhedral volume (0.01 $Å^3$ per 100 K) of the local environment of europium that leads to an elevation of the 5d level because of the reduced crystal field splitting. Notice also that the polyhedral volume change gives a pseudo thermal expansion coefficient of the polyhedron of $3.33 * 10^6(\frac{1}{K})$ which is very close to the thermal expansion coefficient of the host lattice calculated previously, indicating an homogeneous lattice expansion.

6.2.2 Change in ΔR and in Ω

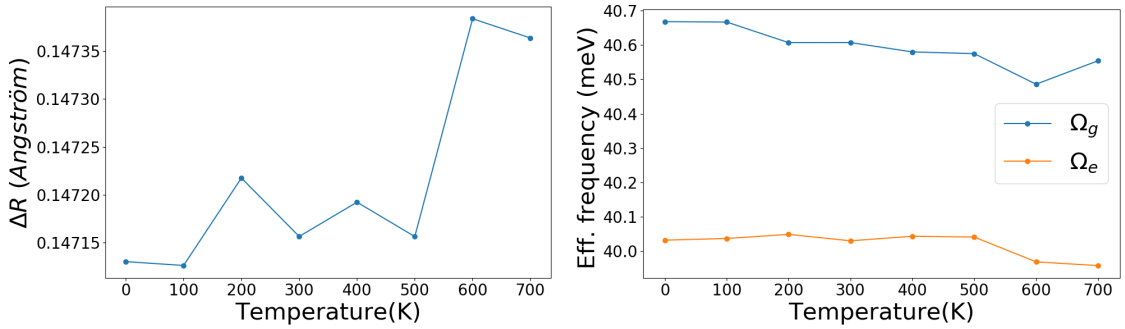

Figure 6.7: Effect of thermal expansion on the effective displacement ΔR and on effective frequencies in ground and excited state

The effect of thermal expansion on the effective displacement ΔR and on effective frequencies in ground and excited state is presented on figure 6.7 (left). As opposed to the change in E_{ZPL}, no obvious trend is observed and the resulting curves are hard to interpret. Still, we will see that these effects are negligible when computing the total luminescence intensity $L(\hbar\omega)$.

6.2.3 Total effect on $L(\hbar\omega)$

The goal was then to observe the total effect of thermal expansion on $L(\hbar\omega)$ by considering the occupation of vibrational levels (as in previous section) **and** by taking into account explicitly the variation of E_{ZPL}, $\Omega_{e,g}$ and ΔR with temperature through thermal expansion. As the changes are difficult to observe directly on the shape of $L(\hbar\omega)$, we provide directly the results by comparing the FWHM and E_{max} of $L(\hbar\omega)$ with and without thermal expansion effect (see figure 6.8). The conclusions arising from this analysis are the following :

- The FWHM temperature dependence seems to be not affected by the thermal expansion effect. This seems reasonable since the FWHM is governed by $\Omega_{e,g}$ and ΔR that do not change considerably with thermal expansion.
- On the contrary, the emission maximum E_{max} is affected by thermal expansion. We can see on figure 6.8 (middle and right) that the difference between the case without

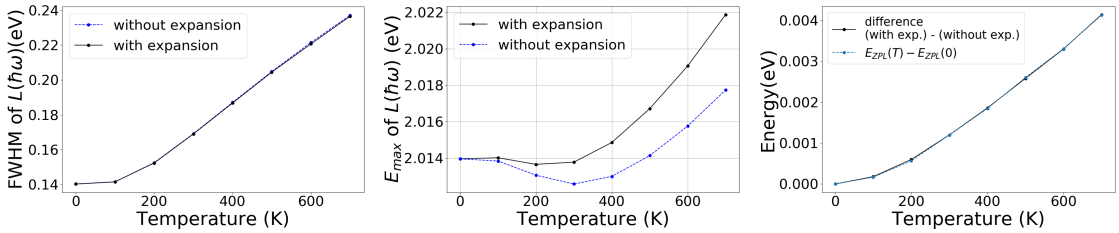

Figure 6.8: Effect of thermal expansion on the FWHM (left) and on the emission maximum E_{max} (middle). Right : Contribution of the thermal expansion in the E_{max} change. It appears that this contribution is principally due to the change in E_{ZPL}

and with thermal expansion is a slope of about 0.72 meV per 100K (in the linear regime) which is roughly equal to the slope found for E_{ZPL}. This confirms that the first order effect comes from the change in E_{ZPL} while the variation of the other parameters with thermal expansion are negligible.

As we have seen, the experimental FWHM is correctly described by the consideration of transitions from higher vibrational states, the thermal expansion being negligible. Considering the thermal expansion for the emission peak shift is however relevant. Still, we observe that this effect is relatively small in SALON:Eu^{2+} because of its high lattice rigidity that leads to a small thermal expansion coefficient. Unfortunately, we are still far from experimental result that shows a slope of 6.7 meV per 100K (emission peak at 614 nm at 300K and 610 nm at 500K). One question arises: is the 1D-CCM really suitable to study the shift of emission maximum?

6.3 Molecular dynamic simulation

At the end of this master thesis, it was also decided to study the temperature dependence of luminescent properties by the means of first-principles Born-Oppenheimer molecular dynamic (MD) simulations on SALON:$^{2+}$. The goal was to focus on the variation of the electronic eigenenergies with temperature that comes from enhanced solid vibrations with temperature increase. To be precise, we can write the temperature dependence of electronic eigenenergies like :

$$\left(\frac{\partial \epsilon_a}{\partial T}\right)_P = \left(\frac{\partial \epsilon_a}{\partial T}\right)_V + \left(\frac{\partial \epsilon_a}{\partial lnV}\right)_T \left(\frac{\partial lnV}{\partial T}\right)_P \tag{6.3}$$

The second term involves the thermal expansion effect ($\left(\frac{\partial lnV}{\partial T}\right) = \alpha_V(T)$) that was calculated in previous section trough the variation of $E_{ZPL}(T) = E_{5d,relaxed}(T) - E_{4f,relaxed}(T)$ with temperature.
The first term of the shift is the contribution of phonon population at constant volume. Actually, this effect has already been estimated in the first section of this chapter when we have considered the quantum formulation of the Franck-Condon principle in the 1D-CCM framework to estimate the luminescence intensity $L(\hbar\omega)$. We have seen however that we were not able to correctly reproduce the experimental emission shift. Here, the goal is to

look at this effect from a classical nucleus dynamics perspective (Newton's law with first-principles forces based on Born-Oppenheimer potential) and thus by considering all the vibration modes in the solid. The idea behind this kind of molecular dynamic simulation is to first pick a temperature from which is deduced the kinetic energy of the ions. Within this kinetic energy constrain, the motion of the ions is governed by the classical equations of motion ($F = ma$). No zero-point motion is thus included here (to do it, one should use Path-Integral molecular dynamic which is way more computationally demanding). At each time-step (and so for each set of ions coordinates), the electronic eigenenergies are calculated by the quantum ΔSCF method.

6.3.1 Method

A first-principles molecular dynamic approach with isokinetic ensemble (variable *ionmov=12* on ABINIT) was performed on doped SALON:Eu^{2+}. To calculate the electronic eigenenergy for a given temperature, the idea is to perform a time-average of eigenenergies from the set of molecular dynamic trajectories $\Delta \boldsymbol{R}(t)$ at temperature T :

$$\epsilon_a(T) = \lim_{\tau \to \infty} \frac{1}{\tau} \int_0^\tau \epsilon_a(\Delta \boldsymbol{R}(t)) dt \tag{6.4}$$

The volume used was the volume of zero temperature (without zero point motion contribution). Four temperatures (300K, 400K, 500K, 600K) were chosen. At each temperature, the molecular dynamic simulation was first conducted in the excited state with one electron manually promoted to 5d level (Δ SCF). 2000 time steps were used with a time step fixed at $2.418884 * 10^{-15}$ seconds which is about 17 times smaller than the smallest period of phonon vibration. For each time step, the local geometry of the 54 atoms and the total energy (from which the kinetic energy of ions was subtracted) were extracted (E_e^* energy in the 1D model picture of figure 3.5). Then, for each of the 2000 local geometry, we calculated the corresponding energy but with the electron in its ground 4f level (E_e energy in the 1D model picture of figure 3.5) for these 4 temperatures. Then, simply by making the difference between the two energies, we have access to the emission energy E_{em} at each time step! Performing the time average of E_{em} for each temperature allow us to have an estimation of the temperature dependence of a "classical" emission spectral function (broadening and shift with temperature). To our knowledge, this is the first time that such method is employed to compute theoretically a luminescence emission spectrum.

6.3.2 Result

We first present what the energies E_e^*, E_e and $E_{em} = E_e^* - E_e$ look like without post processing on the left of figures 6.9, 6.10 and 6.11. It is then possible to plot histograms of these data and to fit gaussians to them, which is shown in the middle figures. From this, we observe two effects : first a broadening of the energies with temperature and secondly a shift of the total energies with temperature. An important point is that the slope of the averaged shift in 5d state (208.10 meV / 100K) is higher than the one of 4f state (206.87 meV / 100K), which induces indeed a blue shift in the emission energy E_{em}! The mean of this blue shift (which is not exactly the difference of the means) is calculated to be 1.13 meV / 100K. This shift should be compared with the shift of the maximum location of

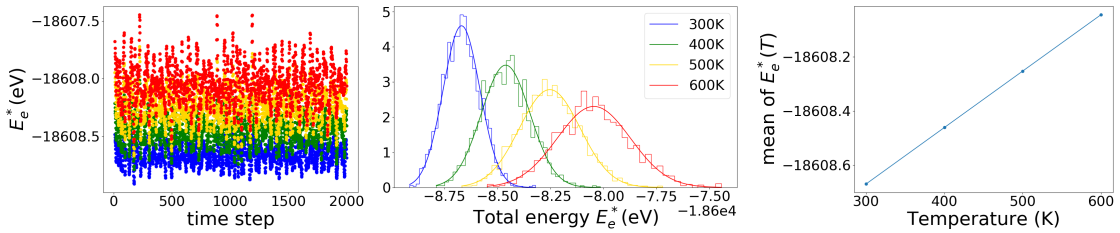

Figure 6.9: Left : Total energy E_e^* computed for 4 temperatures in first-principles molecular dynamic simulation of 2000 time step with europium atom in its 5d excited state. Middle : histogram of those energies at the four selected temperatures of the total energy with a gaussian fitting. Left : mean of E_e^* as a function of temperature, a linear dependence is found with a slope of 0.20810 eV per 100K.

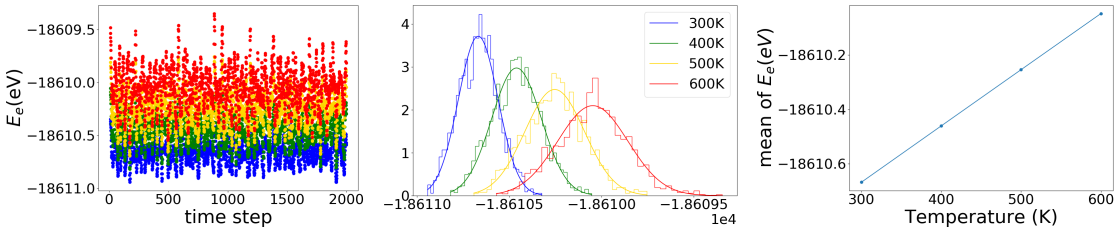

Figure 6.10: Left : Total energy E_e computed for 4 temperatures in first-principles molecular dynamic simulation of 2000 time step with europium atom in its 4f ground state. Middle : histogram of those energies at the four selected temperatures of the total energy with a gaussian fitting. Left : mean of E_e as a function of temperature, a linear dependence is found with a slope of 0.20687 eV per 100K.

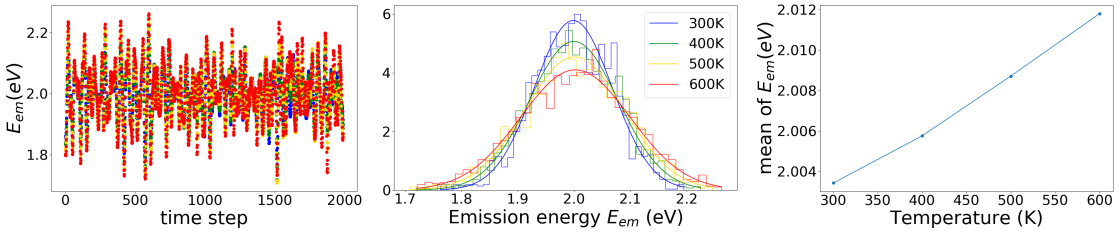

Figure 6.11: Left : Emission energy $E_{em} = E_e^* - E_e$ computed for 4 temperatures in first-principles molecular dynamic simulation of 2000 time step. Middle : histogram of those energies at the four selected temperatures with a gaussian fitting. Left : mean of E_{em} as a function of temperature, a nearly linear dependence is found with an averaged slope of 1.13 meV per 100K between 300 and 500K.

$A(\hbar\omega)$ that we computed in the quantum computation with Franck Condon factors. We observe that here, instead of observing a slight red-shift, a clear nearly linear blue shift is found.

We can go further and assume that the middle plot of figure 6.11 is a classical version of spectral emission function used previously, let us call it $A_{clas}(\hbar\omega)$. Indeed, we can

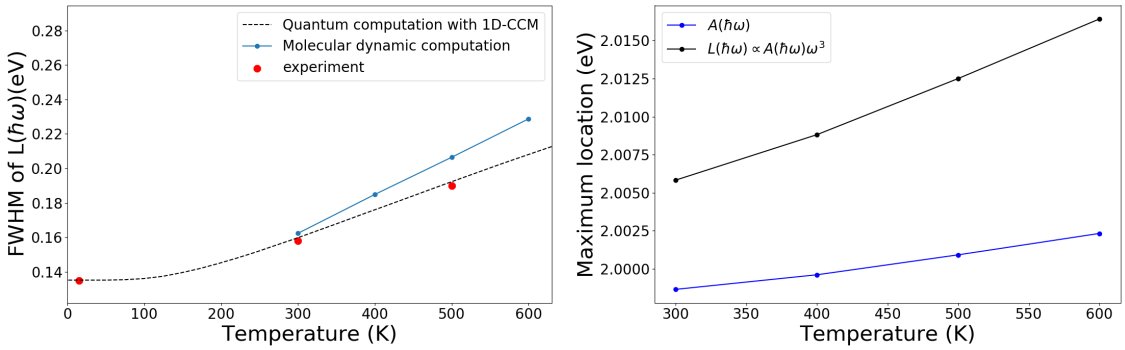

Figure 6.12: Left: Temperature dependence of the FWHM of the luminescence intensity $L(\hbar\omega)$ based on first-principles molecular dynamic simulation. This is compared with the quantum computation of $L(\hbar\omega)$ based on F-C factors and experimental data. Right: Temperature dependence of the position of the maximum of $A(\hbar\omega)$ and $L(\hbar\omega)$.

transform this classical dynamic spectral emission function to a "classical" luminescence intensity by multiplying it by ω^3 : $L_{clas}(\hbar\omega) = C\omega^3 A_{clas}(\hbar\omega)$. This allows us to compare first the FWHM of this classical luminescence intensity (but with all the vibrations modes) with the quantum formulation based on Franck-Condon factors in the 1D-CCM framework (actually, a better comparison would be with a quantum multi-dimensional configuration, which is much more difficult to implement, and has not been done). This is done on figure 6.12 (left). We observe that the MD simulation gives a slightly higher FWHM after 300K. We deduce also that the two curves are crossing just before 300K. Performing the same simulation at smaller temperature could be interesting to confirm this trend and look at the low-temperature dependence in the classical limit. The temperature dependence of the location of the maximum is shown on figure 6.12 (right). We observe that the real shift (the one of the luminescence intensity $L(\hbar\omega)$) is completely different of the shift of $A(\hbar\omega)$! Taking into account this ω^3 factor is crucial to correctly predict the shift! Namely, between 300K and 500K, the shift for $A(\hbar\omega)$ is 2,268 meV while it is 6,676 meV for $L(\hbar\omega)$.
We can also transform our $L_{clas}(\hbar\omega)$ to a luminescence intensity that depends on the light wavelength λ (caution, we are working with distribution, a correct jacobian transformation must be applied as detailed in [64]). The result is shown on figure 6.13. At 300K, the computed FWHM (50.13 nm) is slightly higher than the experimental value (48 nm). The computed emission peak at 300K is at 616,68 nm while the experimental one is 614 nm. Finally, we can also compare the computed shift of this emission peak (616.68 nm at 300K, 613,76 at 500K : shift of around 3 nm in 200K) to which the thermal expansion small blue shift can be added with the experimental one (614 nm at 300K, 610 at 500K : shift of 4 nm in 200K). The agreement is quite good! It is interesting to see that the right order of magnitude of the experimental shift is only obtained when considering all the vibrations mode through a first-principles molecular dynamic simulation. It seems in fact that the 1D-CCM is not suitable to compute such quantity.

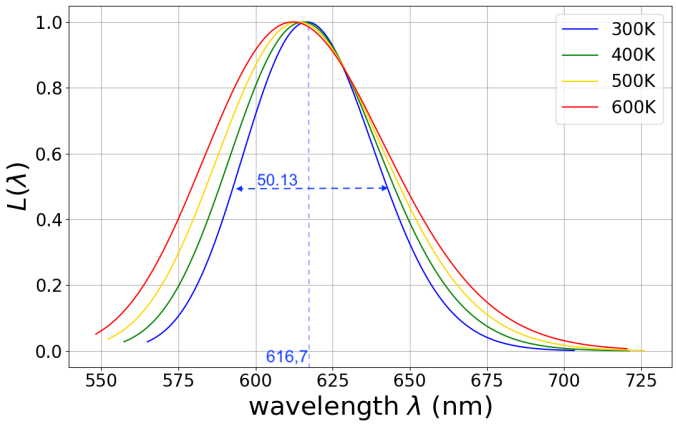

Figure 6.13: Luminescence emission spectrum based on the first-principles molecular dynamic simulation.

6.3.3 Temperature shift : the importance of the ω^3 factor

Let us recap what we have found on the effect of temperature on the FWHM and on the emission peak of $L(\hbar\omega)$ (that are experimentally measured!). When temperature increases, two effects are simultaneously occurring : thermal expansion and phonon population increase (see figure 6.14). In the case of SALON:Eu^{2+} and based on our calculations, thermal expansion has a negligible effect on the FWHM and has a small effect on the emission shift due to an elevation of the 5d emitting level (+1.5 meV between 300K and 500K, about 15-20% of the total shift). Phonon population increase induces first a variation of the 5d and 4f energy levels. The 5d energy grows faster than the 4f energy, leading to an increase of the emission energy with temperature (+2.268 meV). Obviously, this phonon population increase tends also to broaden the emission band. What is not so obvious is that **the broadening of the emission band of $A(\hbar\omega)$ leads to an emission shift of $L(\hbar\omega) = CA(\hbar\omega)\omega^3$, because of this ω^3 factor!**. To be clear, let us take a simple example of a fictitious emission spectral function $A(\hbar\omega)$ that is gaussian shaped and centred at 2 eV with a varying broadening w (blue curve on figure 6.15). With temperature increase, $A(\hbar\omega)$ broadens without changing its peak location. However, if we now consider the luminescence intensity $L(\hbar\omega)$ (black curve), in addition to the direct effect of the broadening of $A(\hbar\omega)$, a clear shift of the emission peak is observed which only originates from the effect of this ω^3 factor.

The conclusions of this study on the origin of the emission peak shift are actually quite different from the conclusions recently proposed by Yan in [65] in his review article on the subject. In his analysis, he argued correctly that the thermal expansion should play a role. We have shown here that this is mainly through the reduction of the crystal field splitting that this effect manifests itself. However, it seems that the effect of the phonon population is missing in his analysis. Based on our results, we have seen that this effect is dominant in the case of SALON:Eu^{2+}. We have also recalled the importance of accounting for the ω^3 when analysing a temperature shift (also something missing in [65]). While interchanging incorrectly $L(\hbar\omega)$ (luminescence intensity measured experimentally) with $A(\hbar\omega)$ (emission

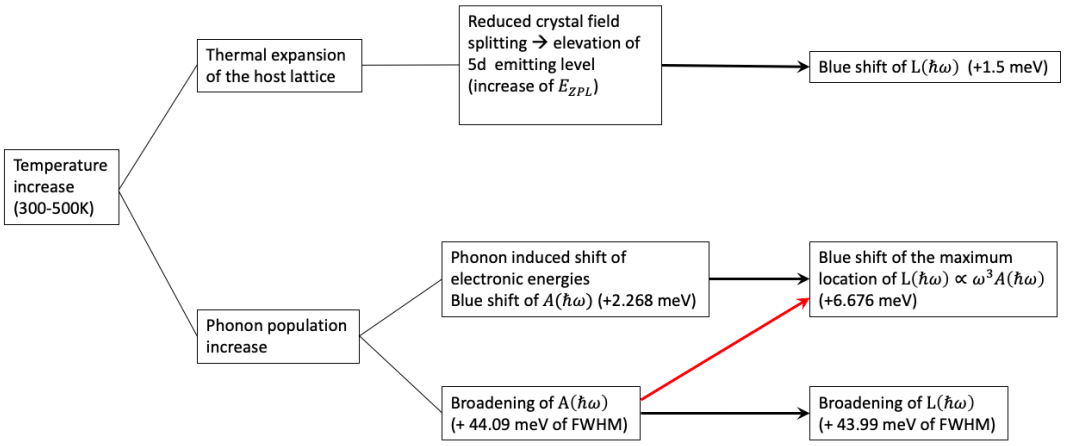

Figure 6.14: Effect of temperature increase on the FWHM and emission peak of the luminescence intensity $L(\hbar\omega)$.

spectral function, not what is measured!) does not have a noticeable impact on the FWHM, this is absolutely not true for the emission peak shift!

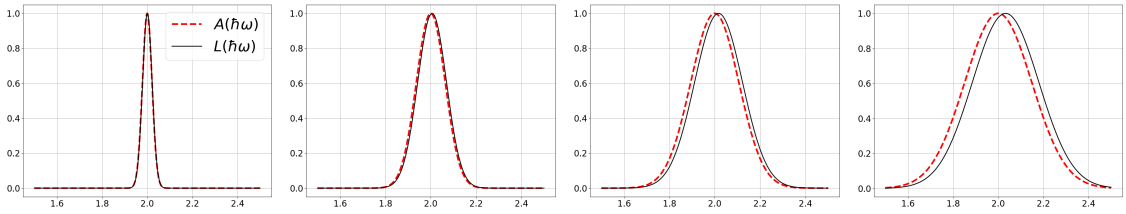

(a) w=0.05 meV (b) w=0.15 meV (c) w=0.25 meV (d) w=0.35 meV

Figure 6.15: Schematic example of the effect of the temperature broadening on the emission peak of $L(\hbar\omega)$.

6.4 Recap and comparison with experiment

Now that we have studied the two temperature effects that are suspected to have an influence on the temperature dependence of the luminescence intensity $L(\hbar\omega)$, let us summarize what we have seen in this chapter : Concerning the FWHM, it appears that considering transitions from higher vibrational levels in the 1D-CCM is sufficient to reproduce correctly experimental data. Moreover, we have seen that thermal expansion has very small influence on the FWHM.
Concerning the emission maximum shift, it appears first that the thermal expansion has a relatively small effect in the total shift (about 15-20%). We have also seen that the 1D-CCM is not suitable to predict correctly the remaining part of the shift. It is only when considering all the vibrations modes (with a molecular dynamic method) that we were able

to reproduce the experimental data. It could be very interesting for further work to see if a quantum model considering all the phonon modes obtains the same result.
Finally,we can use the emission shift computed with molecular dynamic simulation and add it to the emission shift associated to thermal expansion. This total shift can be manually added in the computation of the luminescence intensity spectrum based on the 1D-CCM with F-C factors as done in the first section of this chapter. The result is shown on figure 6.16. The resulting temperature dependence of the luminescence intensity spectrum is compared to the experimental one, the agreement is very good! It is interesting to note the fact that the broadening that only appears on the left side of the spectrum is in fact due to a global shift with temperature of this spectrum. To my knowledge, it is the first time that a first-principles approach succeeds to predict the temperature dependence of the PL spectrum with good agreement with experimental data. And this allows to understand the origin of such temperature dependence, a topics that has been the subject of speculation and confusion for decades.

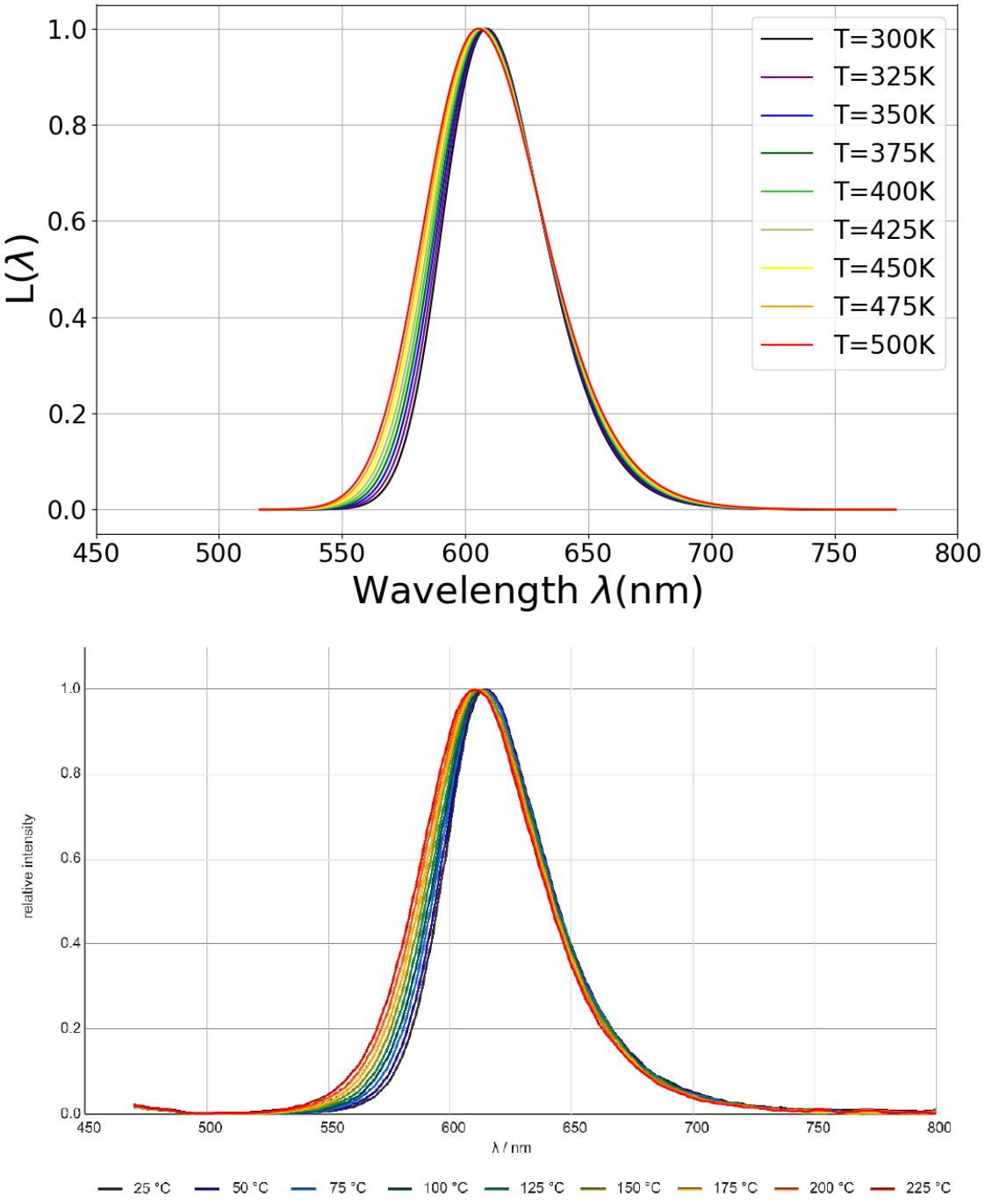

Figure 6.16: Up : simulated luminescence emission spectrum (see text for more details). Down : Experimental luminescence emission spectrum (from [1]).

Conclusion and outlook

It is time to conclude this manuscript that tries to cover the work of one year. A year where I have the feeling to have learned more than during the whole five years of study. Trying to make sens of each equation (that look repelling at first sight I must say), understanding exactly which physical mechanisms are hidden behind those endless formulas, being able to implement those formulas and get predictions that can be compared with real experiments... These are the aspects that made me really enjoy this year.
One year ago, I knew practically nothing about Python. Learning by myself, making a lot of mistakes and being forced to solve each problem ("Where does this obscure error come from ?! ") were very formatting and helped me to develop skills that will be useful for my future life.

The starting point of this master thesis was the recent experimental discovery of a promising narrow emission red phosphor $Sr[Li_2Al_2O_2N_2]:Eu^{2+}$ (SALON:Eu^{2+}) with advantageous luminescent properties (small FWHM and good location of the emission peak). The purpose of this master thesis was to investigate such properties with a combination of *ab initio* calculations performed with ABINIT and an implementation of our knowledge on radiative processes in solids with Python codes.
We began with a first-principles characterization of the bulk properties of SALON : its crystal and electronic structures, phonon modes and its thermal expansion coefficient. Luminescent properties of SALON:Eu^{2+} were then studied with a 1x1x3 supercell of 54 atoms (doping rate of 16.67%). It could be interesting to perform the same analysis with a bigger supercell to check if the residual europium-europium interaction has a noticeable effect on the computed luminescent properties.
Those properties were first analysed at 0K with ΔSCF method. This revealed that SALON:Eu^2 presents a quite high effective frequency $\hbar\Omega_g = 40.67$ meV and a very small effective displacement $\Delta R = 0.147$Å. This leads to a very small Huang Rhys factor $S_{em} = 1.747$, giving an overall narrow FWHM. This very small ΔR can be related to the high rigidity of the lattice hosting europium atom. The stokes shift ΔS is computed to be equal to 0.1399 eV and zero phonon line energy $E_{ZPL} = 2.067$ eV.
The luminescence intensity spectrum was then computed based on a quantum formulation of the Franck-Condon principle. We also performed multi-dimensional analysis based on a full decomposition of the 4f-5d structural relaxation into the phonon modes. It enabled us to identify the phonon mode (at 33.7 meV) that presents a high coupling with optical 4f-5d transition. This phonon decomposition allowed us also to compute the luminescence intensity spectrum with a generating function approach. It appeared that with a sufficient

broadening of each phonon line, the multi-dimensional approach is correctly approximated by the one-dimensional approach.

The temperature dependence of the luminescence properties (shape of the luminescence intensity spectrum, FWHM and emission shift) were then studied. We first showed that considering transitions from vibrational levels $m \neq 0$ within the 1D-CCM was sufficient to reproduce the experimental FWHM. From this analysis, it became clear that the small FWHM increase with temperature comes from the high effective frequency in excited state $\hbar\Omega_e = 40.03$ meV. We noticed also that semi-classical formula gives a correct approximation of the quantum computation. Experimental emission maximum shift with temperature is however not well reproduced with the 1D-CCM. Considering explicitly thermal expansion in the computation showed that the FWHM was practically not influenced by thermal expansion while the emission peak was slightly blue shifted due to a decrease in the crystal field splitting. Finally, only by considering all the solid vibration modes by means of first-principles Born-Oppenheimer molecular dynamic simulation, we found out that we were able to closely reproduce the experimental emission shift. By considering all these effects, we obtained luminescence intensity spectra for any temperature that match correctly the experiment, demonstrating the predictive power of the methodology used in this master thesis.

Let us draw some perspectives for potential future work. This methodology could be used for the theoretical study of other phosphor compounds to further verify its predictive power. It would be for instance very interesting to compare low-temperature spectrum (where phonon side bands are apparent) with theoretical spectrum based on the generating function approach.
From a theoretical perspective, exploring a generalization of the generating function approach for a multi-dimensional model at finite temperature could be also interesting. It would be valuable to compare it with the thermal properties calculated with a one-dimensional model.
It can be also interesting to identify under which conditions the classical and semi-classical formulations of the Franck-Condon principle are a good approximation of the quantum formulation.
On SALON:Eu^{2+}, the theoretical study of thermal quenching behaviour was not addressed (it was only identified that auto-ionization process is supposed to be dominant with respect to 4f-5d cross-over process). This could also be the object of another work.

References

[1] Gregor J Hoerder et al. "Sr $[Li_2Al_2O_2N_2]$:Eu^{2+} —A high performance red phosphor to brighten the future". In: *Nature communications* 10.1 (2019), pp. 1–9.

[2] Audrius Alkauskas et al. "First-principles theory of the luminescence lineshape for the triplet transition in diamond NV centres". In: *New Journal of Physics* 16.7 (2014), p. 073026.

[3] Philippe F Smet, Anthony B Parmentier, and Dirk Poelman. "Selecting conversion phosphors for white light-emitting diodes". In: *Journal of the electrochemical society* 158.6 (2011), R37–R54.

[4] Joachim Schleich, Bradford Mills, and Elisabeth Dütschke. "A brighter future? Quantifying the rebound effect in energy efficient lighting". In: *Energy Policy* 72 (2014), pp. 35–42.

[5] Morgan Pattison et al. *2019 Lighting R&D Opportunities*. Tech. rep. SSLS, Inc., 2020.

[6] Wikipedia contributors. *Light-emitting diode — Wikipedia, The Free Encyclopedia*. [Online; accessed 27-May-2020]. 2020. URL: https://en.wikipedia.org/w/index.php?title=Light-emitting_diode&oldid=956082816.

[7] Yuan-Chih Lin, Maths Karlsson, and Marco Bettinelli. "Inorganic phosphor materials for lighting". In: *Photoluminescent Materials and Electroluminescent Devices*. Springer, 2017, pp. 309–355.

[8] PM Pattison et al. *Solid-state lighting R&D opportunities*. Tech. rep. Technical Report. US Department of Energy, Office of Energy Efficiency, 2018.

[9] Philipp Pust et al. "Narrow-band red-emitting $Sr[LiAl_3N_4]$:Eu^{2+} as a next-generation LED-phosphor material". In: *Nature materials* 13.9 (2014), pp. 891–896.

[10] Ming Zhao et al. "Next-generation narrow-band green-emitting $RbLi(Li_3SiO_4)_2$:Eu^{2+} phosphor for backlight display application". In: *Advanced Materials* 30.38 (2018), p. 1802489.

[11] Claude Cohen-Tannoudji, Bernard Diu, and Franck Laloë. *Mécanique quantique*. Hermann, EDP Sciences, 1998.

[12] Franck Laloë. *Do we really understand quantum mechanics?* Cambridge University Press, 2019.

[13] Christopher A Fuchs and Asher Peres. "Quantum theory needs no 'interpretation'". In: *Physics Today* 53.3 (2000), pp. 70–71.

[14] N David Mermin. "What's wrong with this pillow?" In: *Physics Today* 42 (1989), p. 9.

[15] Carina Faber. "Electronic, excitonic and polaronic properties of organic systems within the many-body GW and Bethe-Salpeter formalisms : towards organic photovoltaics". Theses. Université de Grenoble, Nov. 2014. URL: https://tel.archives-ouvertes.fr/tel-01369304.

[16] X. Gonze. G.-M. Rignanese A. Lherbier. *MAPR 2451 : Atomistic and nanoscopic simulations.* 2019.

[17] Pierre Hohenberg and Walter Kohn. "Inhomogeneous electron gas". In: *Physical review* 136.3B (1964), B864.

[18] Walter Kohn and Lu Jeu Sham. "Self-consistent equations including exchange and correlation effects". In: *Physical review* 140.4A (1965), A1133.

[19] David M Ceperley and Berni J Alder. "Ground state of the electron gas by a stochastic method". In: *Physical review letters* 45.7 (1980), p. 566.

[20] John P Perdew, Kieron Burke, and Matthias Ernzerhof. "Generalized gradient approximation made simple". In: *Physical review letters* 77.18 (1996), p. 3865.

[21] *ABINIT website*. https://www.abinit.org/.

[22] June Gunn Lee. *Computational materials science: an introduction*. CRC press, 2016.

[23] Hendrik J Monkhorst and James D Pack. "Special points for Brillouin-zone integrations". In: *Physical review B* 13.12 (1976), p. 5188.

[24] Wikipedia contributors. *Pseudopotential — Wikipedia, The Free Encyclopedia*. [Online; accessed 23-May-2020]. 2020. URL: https://en.wikipedia.org/w/index.php?title=Pseudopotential&oldid=955834532.

[25] Peter E Blöchl. "Projector augmented-wave method". In: *Physical review B* 50.24 (1994), p. 17953.

[26] Georg Kresse and Daniel Joubert. "From ultrasoft pseudopotentials to the projector augmented-wave method". In: *Physical review b* 59.3 (1999), p. 1758.

[27] Feliciano Giustino. "Electron-phonon interactions from first principles". In: *Reviews of Modern Physics* 89.1 (2017), p. 015003.

[28] Samuel Poncé. "First-principles study of phosphors for white LEDs applications and of the temperature dependence of the electronic structure". PhD thesis. UCL-Université Catholique de Louvain, 2015.

[29] A.A. MARADUDIN and S. H. Vosko. "Symmetry properties of the normal vibrations of a crystal". In: *Reviews of Modern Physics* 40.1 (1968), p. 1.

[30] Christoph Freysoldt et al. "First-principles calculations for point defects in solids". In: *Reviews of modern physics* 86.1 (2014), p. 253.

[31] Xavier Gonze. *MAPR2014, Physics of Functional Materials : Optical properties of materials*. 2018.

[32] Mark Fox. *Quantum optics: an introduction*. Vol. 15. OUP Oxford, 2006.

[33] Shigeo Shionoya, William M Yen, and Hajime Yamamoto. *Phosphor handbook*. CRC press, 2018.

[34] Jose Solé, Luisa Bausa, and Daniel Jaque. *An introduction to the optical spectroscopy of inorganic solids*. John Wiley & Sons, 2005.

[35] Brian Henderson and G Frank Imbusch. *Optical spectroscopy of inorganic solids*. Vol. 44. Oxford University Press, 2006.

[36] Pieter Dorenbos. "A review on how lanthanide impurity levels change with chemistry and structure of inorganic compounds". In: *ECS Journal of Solid State Science and Technology* 2.2 (2013), R3001–R3011.

[37] Baldassare Di Bartolo, Velda Goldberg, and Dennis Pacheco. *Luminescence of inorganic solids*. Springer, 1978.

[38] Yongchao Jia et al. "First-principles study of the luminescence of Eu 2+-doped phosphors". In: *Physical Review B* 96.12 (2017), p. 125132.

[39] Yongchao Jia et al. "Assessment of first-principles and semiempirical methodologies for absorption and emission energies of Ce3+-doped luminescent materials". In: *Advanced Optical Materials* 5.7 (2017), p. 1600997.

[40] Audrius Alkauskas, Matthew D McCluskey, and Chris G Van de Walle. "Tutorial: Defects in semiconductors—Combining experiment and theory". In: *Journal of Applied Physics* 119.18 (2016), p. 181101.

[41] Thomas Greytak. *MIT OpenCourseWare. Lecture Notes : 8.044 Statistical Physics I*. 2013.

[42] Wikipedia contributors. *Quantum harmonic oscillator — Wikipedia, The Free Encyclopedia*. [Online; accessed 6-June-2020]. 2020. URL: https://en.wikipedia.org/w/index.php?title=Quantum_harmonic_oscillator&oldid=947984310.

[43] Charles W Struck and William H Fonger. *Understanding luminescence spectra and efficiency using Wp and related functions*. Vol. 13. Springer Science & Business Media, 2012.

[44] Paola Cappellaro. *MIT OpenCourseWare. Lecture Notes : 22.51 Quantum Theory of Radiation Interactions*. 2012.

[45] Michael A Reshchikov and Hadis Morkoç. "Luminescence properties of defects in GaN". In: *Journal of applied physics* 97.6 (2005), pp. 5–19.

[46] Audrius Alkauskas et al. "First-principles calculations of luminescence spectrum line shapes for defects in semiconductors: the example of GaN and ZnO". In: *Physical review letters* 109.26 (2012), p. 267401.

[47] Wahyu Setyawan and Stefano Curtarolo. "High-throughput electronic band structure calculations: Challenges and tools". In: *Computational materials science* 49.2 (2010), pp. 299–312.

[48] John P Perdew. "Density functional theory and the band gap problem". In: *International Journal of Quantum Chemistry* 28.S19 (1985), pp. 497–523.

[49] Xavier Gonze and Changyol Lee. "Dynamical matrices, Born effective charges, dielectric permittivity tensors, and interatomic force constants from density-functional perturbation theory". In: *Physical Review B* 55.16 (1997), p. 10355.

[50] Ethan T Ritz, Sabrina J Li, and Nicole A Benedek. "Thermal expansion in insulating solids from first principles". In: *Journal of Applied Physics* 126.17 (2019), p. 171102.

[51] G-M Rignanese, J-P Michenaud, and Xavier Gonze. "Ab initio study of the volume dependence of dynamical and thermodynamical properties of silicon". In: *Physical Review B* 53.8 (1996), p. 4488.

[52] Pierre Carrier, Renata Wentzcovitch, and Jun Tsuchiya. "First-principles prediction of crystal structures at high temperatures using the quasiharmonic approximation". In: *Physical Review B* 76.6 (2007), p. 064116.

[53] *Keranova website*. URL: http://www.keranova.se/Engelsk/Exceltabell_E.htm.

[54] VI Anisimov and O Gunnarsson. "Density-functional calculation of effective Coulomb interactions in metals". In: *Physical Review B* 43.10 (1991), p. 7570.

[55] B Amadon, F Jollet, and M Torrent. "γ and β cerium: LDA+ U calculations of ground-state parameters". In: *Physical Review B* 77.15 (2008), p. 155104.

[56] Robert D Shannon. "Revised effective ionic radii and systematic studies of interatomic distances in halides and chalcogenides". In: *Acta crystallographica section A: crystal physics, diffraction, theoretical and general crystallography* 32.5 (1976), pp. 751–767.

[57] A Canning et al. "First-principles study of luminescence in Ce-doped inorganic scintillators". In: *Physical Review B* 83.12 (2011), p. 125115.

[58] A Chaudhry et al. "First-principles studies of Ce-doped $RE_2M_2O_7$ (RE= Y, La; M= Ti, Zr, Hf): A class of nonscintillators". In: *Journal of Applied Physics* 109.8 (2011), p. 083708.

[59] A Canning et al. "First-principles study of luminescence in Ce-doped inorganic scintillators". In: *Physical Review B* 83.12 (2011), p. 125115.

[60] Samuel Poncé et al. "Understanding thermal quenching of photoluminescence in oxynitride phosphors from first principles". In: *The Journal of Physical Chemistry C* 120.7 (2016), pp. 4040–4047.

[61] Jonas J Joos et al. "Insights on the complexity of the excited states of Eu-doped luminescent materials". In: *Inorganic Chemistry Frontiers* (2020).

[62] Mathijs de Jong et al. "Resolving the ambiguity in the relation between Stokes shift and Huang–Rhys parameter". In: *Physical Chemistry Chemical Physics* 17.26 (2015), pp. 16959–16969.

[63] Shigeo Shionoya et al. "Nature of Luminescence Transitions in ZnS Crystals". In: *Journal of the Physical Society of Japan* 19.7 (1964), pp. 1157–1167.

[64] Jonathan Mooney and Patanjali Kambhampati. *Get the basics right: Jacobian conversion of wavelength and energy scales for quantitative analysis of emission spectra*. 2013.

[65] Shirun Yan. “On the origin of temperature dependence of the emission maxima of Eu^{2+} and Ce^{3+}-activated phosphors”. In: *Optical Materials* 79 (2018), pp. 172–185.

Appendices

Appendix A

Structural relaxation results

Atomic positions

	Experimental reduced coordinates			Simulated reduced coordinates		
	x	y	z	x	y	z
Li1	0.13100	0.82100	0.50000	0.12628	0.82291	0.50000
Li2	0.86900	0.17900	0.50000	0.87372	0.17709	0.50000
Li3	0.17900	0.13100	0.00000	0.17709	0.12628	0.00000
Li4	0.82100	0.86900	0.00000	0.82291	0.87372	0.00000
N1	0.58550	0.72990	0.00000	0.58451	0.72903	0.00000
N2	0.41450	0.27010	0.00000	0.41549	0.27097	0.00000
N3	0.27010	0.58550	0.50000	0.27097	0.58451	0.50000
N4	0.72990	0.41450	0.50000	0.72903	0.41549	0.50000
O1	0.25460	0.89305	0.00000	0.25650	0.89285	0.00000
O2	0.74540	0.10650	0.00000	0.74350	0.10715	0.00000
O3	0.10650	0.25460	0.50000	0.10715	0.25650	0.50000
O4	0.89305	0.74540	0.50000	0.89285	0.74350	0.50000
Al1	0.35330	0.68420	0.00000	0.35335	0.68406	0.00000
Al2	0.64670	0.31580	0.00000	0.64665	0.31593	0.00000
Al3	0.31580	0.35330	0.50000	0.31593	0.35335	0.50000
Al4	0.68420	0.64670	0.50000	0.68406	0.64665	0.50000
Sr1	0.50000	0.00000	0.50000	0.50000	0.00000	0.50000
Sr2	0.00000	0.50000	0.00000	0.00000	0.50000	0.00000

Table A.1: Comparison between experimental atomic reduced coordinates and converged simulated ones with PAW pseudopotential and GGA PBE exchange functional. We observe some deviations on the absolute values between experimental and theoretical reduced coordinates : globally the difference does not exceed 0.002 expect for the lithium atoms where the x coordinates of atoms 1 and 2 and y coordinates of atoms 3 and 4 are shifted of 0.0047

Convergence studies

This appendix gives typical convergence studies performed to determine suitable energy cut-off and k-point mesh. Only convergence studies for the bulk SALON study in norm conserving pseudopotential and GGA PBE exchange functional are shown here.

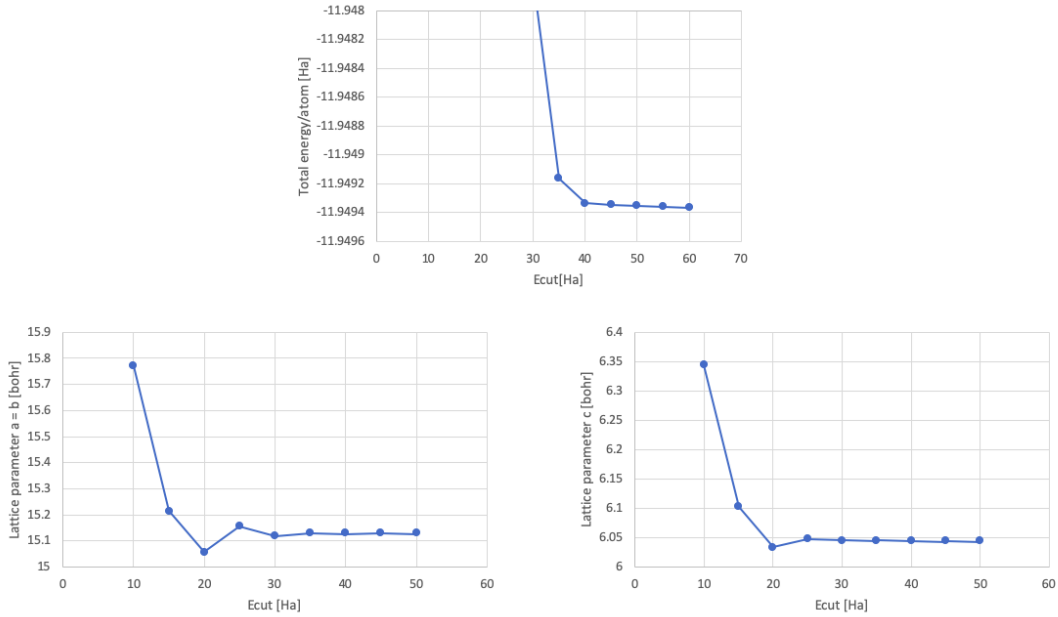

Figure A.1: Convergence study of the total energy and the relaxed lattice parameters as a function of Ecut. The k-point grid was set to 2x2x4.

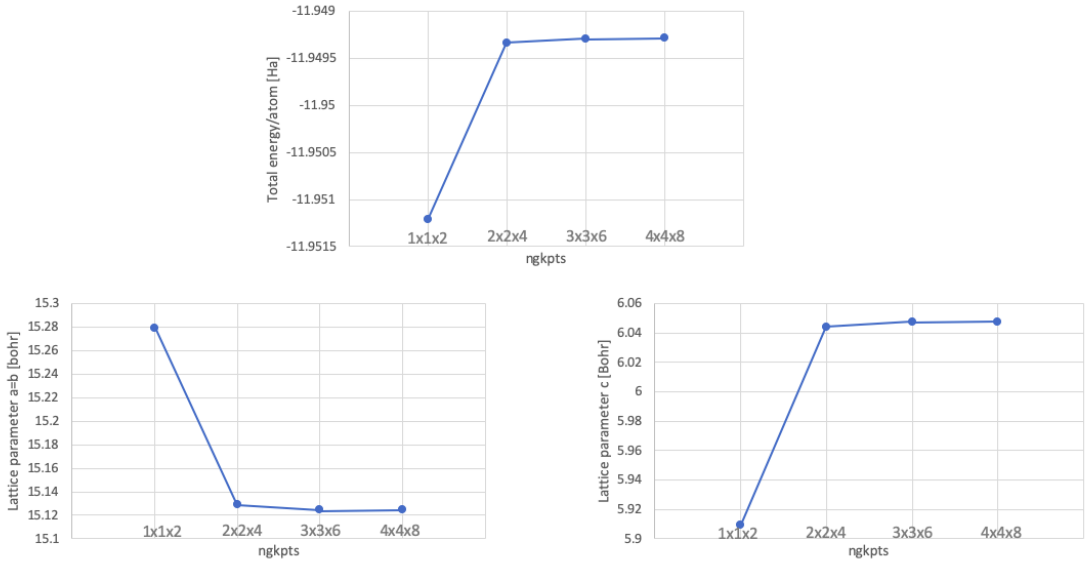

Figure A.2: Convergence study of the total energy and the relaxed lattice parameters as a function of the k-point mesh (variable ngkpts). Ecut was set to 40 Ha.

Appendix B

Phonon frequencies

Table B.1 presents the results of the calculation of the phonon frequencies at Γ point. A k-point grid of 4x4x8 was used and *ecut* was set to 40 Ha. For each mode, the frequency is given in cm^{-1}. To each mode is associated the irreducible representation determined thanks to the characters provided by ANADDB. Letters A and B are for non-degenerate (single) modes where we have only one set of atom vector displacement for a given wavenumber ω. A indicates a symmetry with respect to the principle rotation axis (z here). B indicates an anti-symmetry with respect to the principle rotation axis. Letter E refers to doubly degenerated modes (two sets of atom vector displacements for a given wavenumber ω). The subscripts g and u refer to a mode that is respectively symmetric or anti-symmetric to inversion. Among the 54 modes (18 atoms in 3 dimensions), we observe 8 A_g modes, 5 A_u modes, 8 B_g modes, 5 B_u modes, 4 doubly degenerated E_g modes and 10 doubly degenerated E_u modes.

Phonons frequencies at Γ (cm^{-1}) - Irreducible representation		**Phonons frequencies at Γ (cm^{-1}), direction Γ − X (0 1 0)**		**Phonons frequencies at Γ (cm^{-1}), direction Γ − Z (0 0 1)**	
-0.01 E_u	391.51 E_u	-0.01 E_u	**391.51** E_u	-0.01 E_u	391.51 E_u
-0.01 E_u	391.51 E_u	-0.01 E_u	**393.36** E_u	-0.01 E_u	391.51 E_u
0.00 A_u	407.33 A_g	0.00 A_u	407.33 A_g	0.00 A_u	407.33 A_g
82.00 B_u	424.91 A_u	82.00 B_u	424.91 A_u	82.00 B_u	428.80 E_g
110.02 A_u	428.80 E_g	110.02 A_u	428.80 E_g	124.72 E_u	428.80 E_g
124.72 E_u	428.80 E_g	**124.72** E_u	428.80 E_g	124.72 E_u	434.58 B_u
124.72 E_u	434.58 B_u	**128.74** E_u	434.58 B_u	**140.29** A_u	**462.48** A_u
166.15 B_g	472.14 E_u	166.15 B_g	**472.14** E_u	166.15 B_g	472.14 E_u
169.03 E_u	472.14 E_u	**169.03** E_u	**476.57** E_u	169.03 E_u	472.14 E_u
169.03 E_u	477.39 A_g	179.25 E_g	477.39 A_g	169.03 E_u	477.39 A_g
179.25 E_g	497.27 B_g	179.25 E_g	497.27 B_g	179.25 E_g	497.27 B_g
179.25 E_g	510.37 E_u	188.13 A_g	**510.37** E_u	179.25 E_g	510.37 E_u
188.13 A_g	510.37 E_u	**192.00** E_u	517.97 A_g	188.13 A_g	510.37 E_u
205.37 B_g	517.97 A_g	205.37 B_g	555.00 B_g	205.37 B_g	517.97 A_g
231.08 B_u	555.00 B_g	231.08 B_u	**569.16** E_u	231.08 B_u	555.00 B_g
276.46 A_u	620.09 E_u	276.46 A_u	**620.09** E_u	**283.30** A_u	620.09 E_u
284.19 B_g	620.09 E_u	284.19 B_g	637.97 A_u	284.19 B_g	620.09 E_u
300.53 E_u	637.97 A_u	**300.53** E_u	644.66 E_g	300.53 E_u	644.66 E_g
300.53 E_u	644.66 E_g	**301.06** E_u	644.66 E_g	300.53 E_u	644.66 E_g
317.55 E_g	644.66 E_g	317.55 E_g	645.55 B_u	317.55 E_g	645.55 B_u
317.55 E_g	645.55 B_u	317.55 E_g	667.69 A_g	317.55 E_g	667.69 A_g
323.22 E_u	667.69 A_g	**323.22** E_u	669.15 B_g	323.22 E_u	669.15 B_g
323.22 E_u	669.15 B_g	327.75 A_g	**680.00** E_u	323.22 E_u	705.31 A_g
327.75 A_g	705.31 - A_g	347.13 B_u	705.31 A_g	327.75 A_g	738.11 B_g
347.13 B_u	738.11 B_g	358.13 A_g	738.11 B_g	347.13 B_u	759.55 E_u
358.13 A_g	759.55 E_u	**361.79** E_u	**759.55** E_u	358.13 A_g	759.55 E_u
371.75 B_g	759.55 E_u	371.75 B_g	**811.27** E_u	371.75 B_g	**807.21** A_u

Table B.1: Phonon frequencies at gamma in cm^{-1} and irreducible reprensentation. Second column gives the frequencies at Γ along (0 1 0) direction where we note the splitting of the doubly degenerate E_u modes (in bold). Third column gives the frequencies at Γ along (0 0 1) direction where we note the shifting of A_u modes (in bold).

UNIVERSITÉ CATHOLIQUE DE LOUVAIN
École polytechnique de Louvain
Rue Archimède, 1 bte L6.11.01, 1348 Louvain-la-Neuve, Belgique | **www.uclouvain.be/epl**